Optical Molecular Sensing in Complex Biological Environments

Citation

Nichols, Alexander J. 2015. Optical Molecular Sensing in Complex Biological Environments. Doctoral dissertation, Harvard University, Graduate School of Arts & Sciences.

Optical molecular sensing in complex biological environments

A DISSERTATION PRESENTED
BY
ALEXANDER J. NICHOLS
TO
THE COMMITTEE ON HIGHER DEGREES IN BIOPHYSICS

IN PARTIAL FULFILLMENT OF THE REQUIREMENTS
FOR THE DEGREE OF
DOCTOR OF PHILOSOPHY
IN THE SUBJECT OF
BIOPHYSICS

HARVARD UNIVERSITY
CAMBRIDGE, MASSACHUSETTS
SEPTEMBER 2014

Dissertation advisor: Conor L. Evans Alexander J. Nichols

Optical molecular sensing in complex biological environments

Abstract

Although techniques in molecular imaging have advanced considerably over the past several decades, there remain numerous categories of biological molecular targets that are refractory to straightforward imaging. Among these is molecular oxygen, which is vital to a host of physiological as well as pathological processes, as well as the amorphous pigment pheomelanin, which may play a formerly unappreciated role in melanoma carcinogenesis.

This thesis describes two related bodies of work that advance techniques in oxygen and pheomelanin imaging, respectively. First, inspired by a desire to understand how hypoxia affects cancer chemotherapy on a cellular level, we designed and synthesized a novel oxygen-sensitive, dendritic nanoconstruct that is capable of spontaneously penetrating through hundreds of microns of multiple cellular layers. After demonstrating our nanoconjugate's oxygen sensitivity using time-domain phosphorescence lifetime measurements, we demonstrate that it retains its oxygen sensitivity in a 3D spheroid *in vitro* model of ovarian cancer through the use of a custom-made, near infrared-optimized confocal phosphorescence imaging system. Drawing from this approach, we then describe the fabrication and calibration of a separate oxygen-sensing bandage platform for use in wound-healing applications, and demonstrate its use in *ex vivo* and *in vivo* animal systems.

The second body of work describes the use of non-linear four-wave mixing techniques to facilitate straightforward imaging of the molecular pigment pheomelanin. Recent findings suggest that pheomelanin may play a previously unappreciated role in melanoma carcinogenesis, even in the complete absence of an ultraviolet light insult. However, due to its pale color, pheomelanin is difficult to visualize against a skin background, making its study challenging. After constructing a femtosecond-pulsed coherent anti-Stokes Raman scatter (CARS) microscopy imaging system, we use imaging and spectroscopy to provide proof-of-concept that pheomelanin can be imaged through a combination of CARS microscopy and electronically-enhanced four-wave mixing. We

then use our non-linear imaging system to specifically observe pheomelanin in isolated "redhead" mouse melanocytes, and show through an siRNA gene knock-down strategy that our system can be used to observe changes in pheomelanin signal upon modification of biological pathways known to affect pheomelanin synthesis.

Contents

Author List

The following scientists contributed to **Chapter 2**: Emmanuel Roussakis, Oliver Klein.

The following scientists contributed to **Chapter 3**: Zongxi Li, Emmanuel Roussakis, Pieter G. L. Koolen, Ahmed M. S. Ibrahim, Kuylhee Kim, Lloyd F. Rose, Jesse Wu, Yunjung Baek, Reginald Birngruber, Gabriela Apiou-Sbirlea, Robina Matyal, Thomas Huang, Rodney Chan, Samuel J. Lin.

The following scientists contributed to **Chapter 4**: Sam Osseiran, Joachim "Api" Pruessner, Elisabeth Roider, Vivien Igras.

Listing of figures

This thesis is dedicated to my parents, without whom none of this would be possible,

to my late grandmother Jean, who never missed a beat,

to my late grandmother Adele, who worked tirelessly so my father could have a better life,

and to Whoever upstairs has kept me off the hook for all these years every time I made trouble. Please keep up the good work.

Acknowledgments

As anyone who's ever completed a PhD thesis knows, it is a process that would be impossible to go through alone. I have been fortunate enough to have been surrounded by wonderful people who have guided me through just about every stage of my life and education. There are too many to list, but I will try my best to hit on a few of the "key players" below.

First, my lab mates, past and present: I have learned so much from all of you. Whether it was listening to country music in the chem hood on a Saturday afternoon or pounding away on a grant at 3:00 AM, the time I've spent working with and learning from you has been, without a doubt, the highlight of my graduate education. I might forget how to align a confocal pinhole (maybe), but I won't forget the time we spent together and how each and every one of you was always there for me.

Manolis Rousakis
Yookyung Jung
Zongxi Li
Cindy Hung
Tracy Huang
Joachim Pruessner
Sam Osseiran
Oliver Klein
Jeff Wang
Michael Murphy

In particular, I thank Manolis Rousakis for teaching me everything I know about synthetic chemistry, and for sharing a hood with me for the better part of two years.

Next, I thank the many Professors and investigators who have guided me along my way, whether it was in the context of an advisory committee or a friendly conversation in the hallway:

Gabriela Apiou
Bobby Redmond
Irene Kochevar
Charles Lin
Rox Anderson

Jagesh Shah
Elfar Adalsteinsson
Martha Gray
David Fisher
Sergei Vinogradov

I would like to acknowledge Gabriela Apiou in particular, who has generously and kindly mentored me in the fine art of translational research and whose career advice has been instrumental in my development.

During my recruitment, I once had a conversation with a (famous) chemistry professor, who described the Biophysics program as the "crown jewel" of the Harvard biosciences tracks. In retrospect, he was of course correct, and as everyone in the Biophysics program knows, this is 100% attributable to Michele Jakoulov and Jim Hogle. Simply put, they are phenomenal; they are responsible for making this program the absolute best in the world. Michele's energy and positivity is infectious, and she will do anything and everything for her students. I am grateful to you both.

Of course, I thank my advisor, Conor Evans. When I first met Conor at the end of my first graduate year, he was not yet officially a Professor and had just been granted a modest bench on which to begin his career as an independent researcher. Although my program allowed me to work with just about anyone in Boston and Cambridge, my gut told me that Conor was the guy and the Wellman Center was the place to be. Four years later, I can say that my gut didn't steer me wrong. Not only have I enjoyed the priceless learning experience of Conor's hands-on mentorship in optics and physical chemistry, but I have had the unique joy of watching the lab grow from a two-man think tank to a *bona fide* team of 8+ brilliant scientists with a beautiful new lab space. I am amazed at how much I learned, and I wouldn't trade it for anything. Thanks, Conor.

I gratefully acknowledge the National Science Foundation's Graduate Research Fellowship, the National Defense Science and Engineering Graduate Fellowship, and the Idea^2 Fellowship, all of which made my education a financial reality.

I thank my friends and family: You know who you are, and I won't even try to list you all here. I hope you know how much you all mean to me. No exceptions.

Finally, I thank my parents, Michael and Nancy Nichols. You've shared in my highs, and you've guided me through the rocky narrows of my lows. No words can describe the gratuity, love, and admiration that I feel for you. My successes are as much yours as they are mine, and this thesis is for you.

Several times over the past few years, I have paused for a moment of quiet reflection while walking across campus. In an infinite and constantly expanding universe, across a timeline of humanity that spans more than 50,000 years, I was somehow lucky enough to have been born in civilization's most prosperous era to a comfortable and loving family in the United States of America. We have dentistry, antibiotics, flush toilets, and a panoply of delivery options available via voice-activated smart phone. On top of that, I somehow ended up getting paid to study for a PhD at Harvard University. Considered against the backdrop of civilization's collective history, I feel like I lucked out.

In short, I truly believe that I am blessed to have led such a charmed life full of such caring people. If you are reading this, you're one of them. Thank you.

Believe half of what you see.

-Marvin Gaye

1

Introduction

Over the past several decades, breakthroughs in biomedical imaging technology have created a host of new tools through which to study the most challenging biological problems. Indeed, it is difficult to imagine the practice of modern biology without such techniques as confocal microscopy, first described in 1957, or, more recently, two photon microscopy, which has enabled *in vivo* studies to be conducted in deeper and deeper tissue environments. When combined with the impressive array of fluorescent dyes now available as well as the development of genetically engineered fluorescent proteins such as GFP (for which the Nobel prize in Chemistry was awarded in 2008), these workhorse techniques become powerful and indispensable interrogators of biological form and function.

But what if the structure or process you seek to image doesn't contain a fluorophore, or can't be tagged with one? What if you need to see a small molecule that is refractory to known techniques? Although these scenarios typically call for more complex tactics, all is not lost. So-called "contrast-free" imaging techniques such as coherent Raman vibrational imaging and photoacoustic tomography have made remarkable progress over the past decade and can facilitate imaging based on the target's electronic and vibrational properties, respectively. [1, 2] Similarly, small molecules with no distinctive electronic or vibrational features such as metal ions or gases can often be imaged indirectly though the use of exogenous chemical sensors, although this introduces further complications such as the need for tissue and/or cellular delivery.

This thesis describes distinct but related efforts to advance molecular imaging on two challenging and biomedically relevant targets. The first, which has comprised the majority of my dissertation research effort, describes some of our lab's recent work in the development of novel biocompatible optical oxygen sensors as well as optical sensing platforms for biomedical use. We demonstrate the total synthesis of an oxygen-sensitive, phosphorescent dendritic nanoconjugate as well as the construction of a single-photon counting confocal phosphorescence microscope that can image its near-infrared emission. This conjugate, which we nickname "CAOS" for Click Assembled Oxygen Sensor, is capable of spontaneously penetrating through avascular, multicellular structures as well as 3D *in vitro* cancer models. We go on to discuss potential applications of this work in personalized medicine and cancer therapeutic screenings.

Beyond cancer, the presence of hypoxia in recovering burn sites, surgical grafts, and chronic wounds adversely affects healing and has negative prognostic implications. A technology capable of identifying hypoxia in its early stages could facilitate better short-term and long-term wound care. Leveraging aspects of technology developed through the CAOS project described above, we demonstrate an oxygen-sensitive skin bandage that can be painted on to wound beds and demonstrate its application in *ex vivo* and *in vivo* models of ischemia and burns.

The second effort encompasses the development and early spectroscopic studies of a non-linear optical imaging approach to visualizing the skin pigment pheomelanin, a heterogeneous molecular aggregate responsible for the characteristic reddish/orange color in "redhead" hair. This work, inspired by recent findings in melanoma biology that suggest a new, causative role for pheomelanin in melanoma carcinogenesis, employs a combination of coherent Raman imaging and other non-linear four-wave mixing processes to provide proof-of-concept that pheomelanin can be imaged *in situ* using microscopy techniques and without processing or addition of exogenous contrast agents. It is our hope that these techniques or variants thereof may soon be used to study and better understand melanoma carcinogenesis, both *in vivo* and perhaps even in the clinic.

Although these two bodies of work are focused on the imaging and analysis of different molecular systems, they are unified not only through the chemical/physical approach used throughout their study, but also by the complex biological environments in which their target analytes reside. Oxygen is ubiquitous throughout all respiring cells of the human body, and as such is present in solutions of every conceivable biological pH and protein microenvironment; similarly, pheomelanin is an amorphous aggregate that is believed to be physiological present in cytoplasm, subcellular organelles, and the extracellular space alike. Both oxygen and pheomelanin are refractory to "traditional" imaging techniques, and both are important in a multitude of disease-related processes. Thus, the targets are united through the challenges and rewards of imaging them in their respective complex native biological environments.

Given the different techniques used in each project and the different literature from which our inspirations were drawn, as a courtesy to the reader each body of work will be formally introduced and addressed in a separate chapter or chapter series, and the appropriate literature will be reviewed on a per-chapter basis. Chapters 2 and 3 describe the CAOS and bandage work, respectively, whereas Chapter 4 describes the pheomelanin work.

Finally, while much of this dissertation discusses technical advances intended to facilitate a particular imaging application, the overarching questions driving this work are clinical, and all of our studies are geared towards a particular biomedically relevant end goal. We were inspired not simply to drive new methods of oxygen detection in complex environments, but rather to understand how the absence of hypoxia can lead to therapeutic resistance in cancer patients. Because the appropriate tools did not exist, we decided to build them. Likewise, we seek to image pheomelanin in order to better understand why patients of a particularly skin type (*i.e.*, redheads) are statistically more vulnerable to the devastating but preventable disease of melanoma. Thus, these techniques are meant to be a means to an end rather than as an end in their own right.

It has been my pleasure to conduct this work and it is my sincere hope that you, the reader, enjoy the descriptions and discussions contained in this thesis.

I accept chaos. I'm not sure whether it accepts me.

-Bob Dylan

2

Optical sensing of hypoxia

As the third most abundant element in the known universe and one of the primary constituents of Earth's atmosphere, molecular oxygen is ubiquitous in living systems and essential to the existence of all known higher organisms. Mammals have evolved complex and adaptive circulatory systems that deliver oxygen throughout the body, while simultaneously engaging biological fail-safe mechanisms to prevent its toxic derivatives from escaping and causing cellular damage. Impaired oxygen delivery to tissue regions is etiologically significant in a wide range of pathological conditions ranging from cancer therapeutic resistance to diabetic ulcers.

In spite of its profound biological and clinical importance, few effective tools exist for nondisruptively quantifying oxygen in its physiological milieu. Oxygen's absorption peaks and emission spectrum are poorly specific and difficult to assess in a biological context, and its most abundant isotopic form is not active for magnetic resonance studies. Even the so-called "gold standard" metric of electrochemical, needle-based point measurements suffers from severe drawbacks, including the difficulty of probing large surface areas and the inherently disruptive nature of the instrument and measurement process. Furthermore, large oxygen consumption gradients are believed to exist within even a single organ or glandular structure, making the ability to quantify molecular oxygen at the tissue, cellular, and subcellular level necessary in order to impactfully study this simple molecule's profound profound impact on physiology and disease.

This chapter addresses a new chemical approach to satisfy this unmet need. We demonstrate the total synthesis of phosphorescent oxygen-sensitive molecules that penetrate multicellular structures and describe the construction and application of specialized analytical and imaging systems necessary to use these molecules. In order to contextualize the importance of oxygen measurement in both normal physiology as well as pathological states, we begin with a brief review of physiological oxygen tensions throughout the body and a discussion of oxygen's involvement in disease states such as cancer. Following this, we describe our unique approach to intracellular oxygen reporting and follow with a detailed description of our methods and future applications.

2.1 Overview: Cellular mechanisms of oxygen consumption, utilization, and metabolic regulation

2.1.1 A very brief history

The discovery of oxygen was a landmark in the chemical sciences and represented in its era a departure from prevailing scientific theories. Early understandings of oxygen propagated by the German alchemist J.J. Becher attempted to explain combustion using the "phlogiston" model, which posited that all combustible bodies comprised a flammable element known as phlogiston that was released to the environment upon combustion, leaving behind a dephlogistonated *calx*. This incorrect model was shaken in the late eighteenth century through a series of experiments that demonstrated that in many cases combustible materials can actually gain weight during combustion, thereby calling into question the model's central tenant (*i.e.*, loss of mass vis-a-vis phlogiston). Although numerous scientists could arguably be credited with the discovery of oxygen *per se*, the British clergyman Joseph Preistly was the first to publish his findings, which demonstrated that oxygen liberated through addition of heat to mercuric oxide (HgO) would produce a "physiologic enhancement" both in laboratory mice and in himself. The name "oxygen" stems from work conducted by the French chemist Antoine Lavoisier, whose findings laid the groundwork for our modern understanding of combustion and who named the gaseous element required *oxygène*, based on the Greek word for "sharp." (Lavoisier incorrectly believed oxygen to be an essential component of all acids, which elicit a characteristic sharp and sour taste.) [3, 4]

2.1.2 OXYGEN TRANSPORT AND CONSUMPTION IN TISSUE

Although smaller organisms such as insects can support metabolism on the organismal scale through passive diffusion, higher organisms such as mammals have evolved complex respiratory and circulatory systems to transport oxygen to throughout bodily tissues. On its own, oxygen's solubility in blood is poor (0.03 mL L_{blood}^{-1} $mmHgO_2^{-1}$), thereby making the presence of an oxygen carrier molecule essential to meet the respiratory needs of metabolically active tissues. In humans, this carrier protein is hemoglobin, a remarkable tetrameric heme protein densely packaged in red blood cells that additionally serves crucial roles in carbon dioxide homeostasis and nitric oxide transport. [5] Each hemoglobin molecule can bind four oxygen molecules, thereby increasing the oxygen carrying capacity of blood 65- to 70-fold. [5]

To understand the effects in tissues of reduced or otherwise impaired oxygen delivery, it is first necessary to define basal levels of oxygenation and appreciate the heterogeneity that exists in oxygenation throughout healthy human organs. Under normal atmospheric conditions (*i.e.*, room air), oxygen constitutes roughly 21% of air by volume, corresponding to a partial pressure of 158 mmHg. (Under standard cell culture conditions, this number is often reduced to 150 mmHg due to the addition of 5% CO_2 for pH control.) During inspiration in a healthy individual, the oxygen partial pressure (pO_2) drops to approximately 100-110 mmHg in the alveolus, the functional unit of air exchange within the lung. [6] After diffusing across the lung epithelium, oxygen encounters deoxygenated venous blood and reoxygenates it. In a healthy adult, the pO_2s of arterial and venous blood (approximately 90 mmHg and 40 mmHg, respectively) are generally considered proxies for the pO_2s of blood on either side of the pulmonary vasculature and are thus important and well-known clinical parameters. [6]

Downstream of arterial circulation, there exists substantial variability within the literature on physiological oxygen tensions in solid organs. For example, the brain's dense neuronal parenchyma is extraordinarily metabolically active, such that its oxygen consumption rates are high; oxygen tensions in the frontal white matter typically average 40 mmHg, but results ranging from 33-48 mmHg and beyond have been reported. [7, 8] Likewise, muscle tissues exhibit pO_2s of 25-32 mmHg, depending on depth, muscle type, and muscle location. [7] In contrast, reported pO_2s from livers exhibit a wider range and dependence on physiologic state. Whereas transplant recipients exhibit liver pO_2s of upwards of 60 mmHg 48 hours after transplant, intraoperative pO_2s recorded using a different method showed a median pO_2 of 31 mmHg. [7, 9] Thus, physiological oxygen tensions can be highly heterogeneous and dependent on tissue function.

In considering these data, it is important to note that many were generated using the point-based electrochemical methods, which are inherently limited and of debatable utility in the solid organ environment; the advantages and drawbacks of these systems will be discussed in Section 2.3.1. It is also important to note that these numbers reflect solid tissue pO_2s, as opposed to arterial pO_2s measured in the organ-associated vasculature.

2.2 CELLULAR AND TISSUE RESPONSES TO HYPOXIA

2.2.1 ORGAN-LEVEL EFFECTS OF HYPOXIA

Broadly speaking, hypoxia is biologically defined as a physiological state wherein the equilibrium pO_2 within a tissue or cell is insufficient to meet the oxygen demands of that tissue. In order to appreciate the need for tissue-based oxygen sensors and the sensing range over which they must operate, it is essential to both define hypoxia quantitatively and physiologically, as well as to understand how and when insufficient oxygen can be damaging to tissues. We will therefore proceed by first describing the organ-level effects of hypoxia through two illustrative examples, followed by a brief discussion of hypoxia's effects at the cellular and molecular level.

As described above, oxygen homeostasis in tissues is fundamentally a function of two parameters: oxygen supply and oxygen demand. In the heart, for example, myocardial oxygen demand is determined through a number of factors including heart rate and the contractility or the intensity of each heart beat. [10] On the supply-side, vital physiological properties can be altered to dynamically adjust the blood supply to respiring myocardium, including modulation of vascular resistance and therefore coronary blood flow, modulation of coronoary vascular properties by accumulated metabolites such as adenosine, and the mechanical forces exerted on the coronary arteries through the heart's contraction. [10] When one or more regulatory element in this system becomes compromised (for example, reduced coronary blood flow secondary to atherosclerosis and vessel stenosis), the heart exhibits changes on both the cellular and organ level; cardiac myocytes may switch from aerobic to anaerobic respiration, resulting in an altered paracrine excretion profile as well as altered contractility and impaired ability to meet overall physiological blood delivery needs throughout the body. [10] Although the pO_2 at which this process occurs remains unclear, in part due to the lack of reliable measurement techniques, studies suggest the ischemic threshold may be near 22 mmHg, with myocardial oxygen tensions falling to 6 mmHg or lower during severe hypoxic/ischemic episodes.[11–13]

Another example of oxygen's pathophysiological relevance is hypoxic-ischemic retinal disease. As the tissue responsible for the energy-intensive process of vision transduction, the retina is among the most metabolically active tissues in the body. [14] Retinal ischemia/hypoxia is a sequela of numerous disease states including diabetes, chronic obstructive pulmonary disease, trauma, and obstructive vascular diseases, and is itself among the causative factors of diseases such as glaucoma and macular degeneration. [14]. Beyond inducing retinal ganglion cell death, however, retinal hypoxia can lead to debilitating consequences through a variety of biochemical mechanisms, many of which will be discussed in greater depth below. In the eye, hypoxia leads to downstream synthesis of vascular endothelial growth factor (VEGF), a protein that stimulates new blood vessel growth, which in turn leads to angiogenesis, elevated intraocular pressure, fluid accumulation, and the induction of cytotoxic inflammation. [14] Hypoxia has also been demonstrated to induce increased production of nitric oxide (NO), a gaseous hormone that has been associated with both enhanced vascular permiability and neurotoxicity, as well as increase neuronal excitotoxicity through hypoxia-related accumulation of excitatory neurotransmitters such as glutamine. Various hypoxia-related paths to retinal ganglion cell death are outlined in Figure 2.2.1.[14]

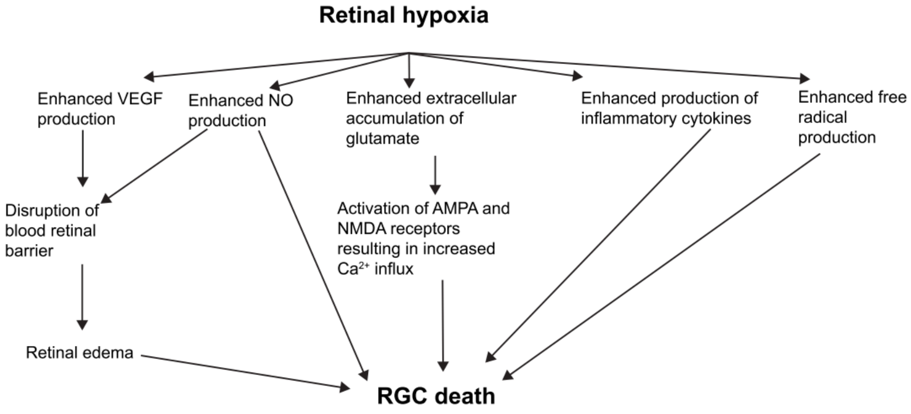

Figure 2.2.1: A depiction of possible factors contributing to Retinal Ganglion Cell (RGC) death in retinal hypoxia-ischemia. Reproduced from [14].

Finally, it is important to note that hypoxia is not always indicative of pathology *per se*, and can be normal in certain tissue types. Bone marrow, for example, has been measured to be physiologically hypoxic, and hypoxia is believed by some to be essential for normal hematopoiesis. [15–17]

2.2.2 CELLULAR AND MOLECULAR EFFECTS OF HYPOXIA

Although hypoxia's effects on the cellular level are myriad and often dependent on the function of the affected cell type, only well-described mechanisms common to multiple cell types will be discussed here. [18, 19] The most studied molecular effectors for hypoxia are the family of transcription factors called hypoxia-inducible factors (HIFs), among which the best characterized is HIF-1. HIF-1 is a heterodimeric protein comprised of a constitutively expressed subunit HIF-1β and an additional oxygen-dependent subunit HIF-1α. Under normal conditions, HIF-1α is rapidly degraded through the ubiquitin-proteasome system. Under hypoxic conditions, however, the rate of HIF-1α degradation is reduced, facilitating its accumulation and increased interaction with HIF-1β and enabling the HIF-1α/β complex to act as a transcription factor.[1] The result is transcriptional

---

[1] This also occurs in the presence of reduced iron concentration.

activation of genes including VEGF, lactate dehydrogenase A (LDH-A), the pyruvate dehydrogenase family enzymes (PDKs) including PDK1, and a host of glycolytic enzymes. [14, 20]

The hypoxia-induced increase in HIF-1 activity is additionally coupled to a metabolic shift from aerobic to anaerobic metabolism that reduces cellular demand for oxygen. While much remains unknown about the manner through which this shift takes place, it is known to occur through a combination of cellular mechanisms including a reduction in mitochondrial oxygen use through reduced uptake of glycolytic intermediates, activation of key metabolism-controlling genes such as PPARα and PDK4, and HIF-1 mediated upregulation of glycolysis-associated genes as described above. [21, 22] In addition to helping to balance oxygen supply with oxygen demand, this metabolic shift is cytoprotective on a number of levels. One result of inadequate cellular oxygenation is the generation of reactive oxygen species (ROS) such as superoxide along the mitochondrial electron transport chain; HIF-1 pathway induction acts in a negative feedback loop to reduce oxidative phosphorylation, resulting in a decreased rate of both ROS creation and mitochondrial damage.[22, 23]

In instances of acute or otherwise unmanageable mismatch between oxygen supply and demand, cellular death can occur through multiple pathways including apoptosis, necrosis, or autophagy. [24–28].

2.2.3 HYPOXIA AND CANCER

In addition to its role in diseases of ischemic etiology, hypoxia is known to occur in tumors and is an important clinical factor in cancer treatment planning and efficacy. Primary solid tumors become hypoxic as they grow beyond the diffusion distance of oxygen from nearby vasculature (up to 200 μm). [29] As described above, the presence of hypoxia contributes to HIF-1 activation and leads to the transcription of genes including VEGF, which in turn stimulates the growth of new blood vessels in the vicinity of the tumor. The resulting tumor-associated neovasculature is morphologically chaotic and leaky and often fails to deliver oxygen uniformly throughout the entirety of the tumor, thereby contributing to the formation of heterogeneous regions of hypoxia. [30–33] Once present, hypoxic conditions exert a plethora of tumor-promoting effects, including suppression of apoptosis, elevated genomic instability secondary to hypoxia-induced ROS generation, enhanced invasiveness, altered lipid metabolism, and selection of somatic mutations favorable to survival in the hypoxic environment.[29, 34]. Clinically, hypoxia contributes to resistance to numerous cancer therapies including the chemotherapeutics etoposide, 5-fluorouracil, paclitaxel, and doxorubicin, as well as to radiation therapy. [20, 29, 35–37] In some cases, the therapeutic resistance can be dramatic; for example, up to 100-fold decreases in paclitaxel cytotoxicity have been reported under hypoxic conditions. [38]

It is important to emphasize that heterogeneities in tumor oxygenation occur on the *microenvironmental* level, and can vary across clusters of cells or even individual cells. To the extent that the presence of hypoxia affects therapeutic response, this highlights the importance of understanding tumor oxygenation on a cell-by-cell level, as even single cells that survive therapy can seed recurrence or therapy-resistant disease. [35, 39–41]

2.3 Chemical approaches to oxygen sensing

2.3.1 Electrochemical methods

For many years the "gold standard" for oxygen sensing has been the so-called Clark electrode. [42] This electrode relies on platinum surface catalysis to perform the following net reaction:

$$\mathrm{o_2} + 4\,\mathrm{e^-} + 2\,\mathrm{H_2O} \longrightarrow 4\,\mathrm{OH^-} \tag{2.1}$$

The electrode itself resides in an aqueous electrolyte solution that is embedded in a fine glass tip; the electrode assembly is then attached to a sensitive ammeter (*e.g.*, a picoammeter) that measures the current generated, which upon proper calibration is proportional to the oxygen at the tip. Although this system has been used to make innumerable measurements in physiological settings, it does suffer from several important drawbacks. First, as an electrode-based system, it is capable of providing only a scalar value proportional to oxygen concentration at a single location; thus ,2D surface measurements as well as measurements of areas smaller than the needle tip (<0.5-1mm) become tedious and problematic. Second, the reaction consumes both oxygen and water, such that the probe actively and constitutively consumes oxygen throughout its operation; this leads to an additional requirement of stirring or agitation to maintain an equilibrium distribution of oxygen at the site of measurement to avoid errors, a challenging task in biological tissue. Third, insertion of a Clark electrode into a sample site is often mechanically and chemically disruptive. Fourth, the probes are temperature and pH sensitive, such that precision measurements require careful calibration across temperature ranges as well as knowledge of the temperature of the analyte solution or tissue. Fifth, Clark electrodes suitable for use in tissue have small tip diameters (often $\leq$1 mm) and are thus fragile and easy to break. Thus, although Clark electrodes find frequent use in a variety of oxygen-sensing contexts (*e.g.*, calibration of other oxygen sensors), they are not ideally suited for biological oxygen measurements on 2D surfaces or complex 3D tissue environments. Readers interested in further discussion of advances in Clark electrodes as well as their pros and cons are referred to a recent, comprehensive review on the subject. [42]

2.3.2 INTRODUCTION TO THE PHOSPHORESCENCE LIFETIME METHOD OF MEASURING OXYGEN TENSION

A powerful alternative methodology for determining oxygen tension in tissue is oxygen-dependent quenching of phosphorescence, also known as "phosphorescence quenching." First proposed by Vanderkooi *et al.* in 1987 as a means of measuring oxygen tension *in vitro*, phosphorescence quenching is an optical technique that exploits the ability of the triplet ground state of molecular oxygen to collisionally interact and exchange energy with the exited state of luminescent molecules, thereby non-radiatively quenching their excited state and shortening the ensemble-averaged excited state lifetime. [43] While this process is possible for excited singlet states (*i.e.*, fluorophores), the microsecond- to millisecond excited state lifetime of triplet emitters (*i.e.*, phosphors) makes them statistically more sensitive to oxygen-mediated quenching than singlet emitters, which have excited state lifetimes on the order of nanoseconds. [44] Additionally, the triplet-triplet interaction that occurs in phosphor-oxygen collisional interaction is more favorable to non-radiative collisional energy transfer than the singlet-triplet interactions that occur between fluorophores and oxygen, as the triplet-triplet interaction is not spin-forbidden.

While a variety of molecules and heavy metal complexes such as iridium and ruthenium complexes are know to phosphoresce, the phosphorescence quenching research community has largely favored the use of porphyrins and porphine analogues due to a number of factors including their stability, their ability to interact with biomolecules such as albumin, their typically red-shifted emission, and the fact that they are ubiquitous in biology.[42, 43, 45, 46] Palladium and platinum-containing porphyrins have been particularly popular, owing in part to the fact that their relatively long lifetimes (40-100 μs and 400-1000 μs for Pt- and Pd-porphyrins, respectively) provide a broad temporal quenching window and therefore a large dynamic range of sensing. In addition, their phosphorescence emissions are bright relative to other porphyrins, and their absorption spectra exhibit large molar extinction coefficients in both the UV and the visible regions (370-450 nm and 500-650 nm, respectively).

THEORY OF OXYGEN-DEPENDENT QUENCHING OF PHOSPHORESCENCE

Consider a phosphorescent molecule PM that emits from an excited triplet state PM^{T}. The two competing pathways through which the excited phosphor decays are phosphorescence (with rate constant k_1) and non-radiative energy transfer to a quenching molecule Q (at rate constant k_2). Thus, the rate of change of PM^{T} is:

$$\frac{\mathrm{d}[\mathrm{PM}^{\mathrm{T}}]}{\mathrm{d}t} = -k_1[\mathrm{PM}^{\mathrm{T}}] - k_2[\mathrm{PM}^{\mathrm{T}}][\mathrm{Q}] \tag{2.2}$$

Separating the variables in Eq. 2.2 and integrating gives:

$$[\mathrm{PM^T}] = [\mathrm{PM_0^T}]e^{-(k_1+k_2[\mathrm{Q}])t} \tag{2.3}$$

Here, $\mathrm{PM_0^T}$ is the concentration of triplet emitters immediately following an excitation pulse.[2] Because the phosphorescence intensity is proportional to the concentration of emitters present, Eq. 2.3 can be re-written as:

$$I = I_0 e^{-\frac{t}{\tau}} \tag{2.4}$$

Eq. 2.4 states that a homogeneous population of excited phosphors in the presence of a quenching agent decays according to a negative exponential function. Thus, substituting in the exponential argument from Eq. 2.3, we arrive at:

$$\frac{1}{\tau} = \frac{1}{\tau_0} + k_2[\mathrm{Q}] \tag{2.5}$$

Where $\frac{1}{\tau_0} = k_1$ is the intrinsic decay of the phosphor in the complete absence of a quencher, and k_2 is a second-order rate constant that describes the frequency of collision between the phosphor and the quencher. This important result is known as the *Stern-Volmer equation*, which describes the inverse lifetime as a function of the molecularly intrinsic quantity τ_0 and the concentration of a quencher Q. [47] Importantly, note that Eq. 2.5 is independent of the concentration of the emitter; practically speaking, this means that this approach can be used to quantify quenchers across arbitrary concentrations of emitters, a useful result in tissues where the concentration of phosphor may vary from point to point.

---

[2] Implicit in this derivation is the assumption that the excitation pulse is treated as a δ function; in the more realistic case that the excitation pulse has a finite width, the decay function will be a convolution of the excitation pulse shape and the decay function. This scenario arises in this work and is discussed in Section 2.5, as well as in Chapter 3. Note that for cases where the excitation pulse is short relative to the decay time (i.e., femtosecond pulses *vs.* microsecond decays), the effects of the convolution are minimal and can be ignored.

For the scenarios discussed herein in which the quenching molecule is dissolved oxygen, it is often more convenient to discuss the quencher in terms of partial pressure (pO_2) rather then molarity. Assuming that Henry's law holds, the oxygen concentration can be re-written as $[O_2] = \alpha pO_2$, where pO_2 is the partial pressure of oxygen and α is oxygen's solubility coefficient in units of M/mmHg. [44]

$$\frac{1}{\tau} = \frac{1}{\tau_0} + \alpha k_2(pO_2) = \frac{1}{\tau_0} + k_q(pO_2) \tag{2.6}$$

Where $k_q = \alpha k_2$ with units of $\text{mmHg}^{-1}\text{s}^{-1}$.[3]

2.3.3 IMAGING METHODOLOGIES AND APPLICATIONS BASED ON PHOSPHORESCENCE LIFETIME

Shortly after its initial description, oxygen quenching of phosphorescence lifetime was adapted as an imaging modality by Rumsey *et al.*, who used it to perform 2D planar imaging of oxygen tension in anoxic and normoxic Sprague-Dawley rat livers. [43, 48] In this early experiment, Rumsey and colleagues used a xenon arc lamp/camera system to provide a brief excitation pulse to an *ex vivo* liver perfused through the portal vein with a Pd-coproporphyrin-containing buffered mixture maintained at 95% O_2/5% CO_2; the liver was then imaged with a camera to acquire the phosphorescence intensity. Upon perfusion with an anoxic buffered mixture, the phosphorescence intensity was observed to increase four-fold, consistent with the decreased rate of oxygen-mediated phosphorescence quenching over the imaging period as predicted by Vanderkooi *et al.* [43, 48]. Notably, this early technique imaged phosphorescence *intensity*, not lifetime, but was still groundbreaking in its ability to non-perturbatively capture course-grain changes in oxygenation across an entire imaging plane as opposed to a single point, as was the previous state-of-the-art. Furthermore, unlike methods relying on Clark electrodes, the resolution for this experiment was limited

---

[3] Nomenclature for the quenching constant k_q can vary throughout the literature; for example, k_q can be used interchangeably with k_2 when partial pressures are not involved. Generally, this does not affect any practical aspect of the Stern-Volmer equation or its application.

by the camera's pixel density and resolution and not the diameter of a Clark electrode tip.

In the decades that followed, this rudimentary approach underwent substantial development and was transformed into a sophisticated and precise technique suitable for a wide variety of oxygen measurement applications. [44] Modern planar phosphorescence imaging methodologies typically involve either a time-domain or Fourier-domain approach in which the phosphorescence lifetime is measured per-pixel across an imaging sample, usually while the imaging target or animal is immersed in or perfused with a phosphorescent mixture. In the former approach, the sample is illuminated by a brief, widefield pulse, as above. However, rather than collect a simple intensity-based image that is time-averaged over the entire millisecond phosphorescence decay period, time-domain phosphorescence lifetime imaging approaches employ fast, time-gated CCD cameras to collect phosphorescence in a limited temporal window during the sample's decay; the lifetime τ is then recovered through curve-fitting (and deconvolution if necessary; see Figure 2.3.1, the footnote in Section 2.3.2, and Chapter 3). For ideal samples that exhibit a single-exponential phosphorescence decay, it is in principle possible to determine the phosphorescence lifetime per-pixel in as few as two excitation pulses (Figure 2.3.1). In many situations, however, multiple pulses and a statistical averaging approach are used to determine the lifetime τ. [42, 44, 49–52]

The Fourier-domain based approach takes advantage of the fact that phosphorescence from a long-lived phosphor (as well as photoluminescence more generally) will appear phase-shifted with respect to a frequency-modulated illumination source due to the delay between excitation and emission. [42, 53, 54] In this approach, pioneered for use in oxygen-sensitive phosphors by Vinogradov *et al.*, a light source modulated at frequency f is delivered to the sample, often by means of an optical fiber. The Stokes- and phase-shifted emission is then waveguided to a fast photodetector such as an avalanche photodiode, where it is digitized for analysis and the phase shift φ is

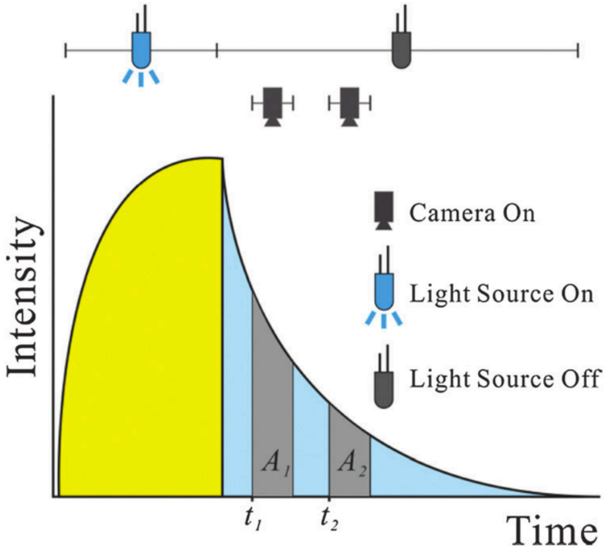

Figure 2.3.1: A typical two-point time-domain lifetime imaging experiment, performed with a time-resolved camera. A_1 and A_2 describe the two signal collection windows, each recorded over a separate flash/imaging cycle. Reproduced from [42].

determined.[4] [42, 53] This is related to the lifetime τ as follows:

$$\tan \varphi = 2\pi f \tau \tag{2.7}$$

Once determined through Eq. 2.7, τ can be related to pO_2 through the Stern-Volmer equation as described in Section 2.3.2. Systems operating on this principle have been successfully commercialized and are sold by Oxygen Enterprises, Inc. [53, 55]

Although the Fourier domain-based method described above enjoys several benefits over its time-domain competitor, it also has its drawbacks. Historically, Fourier-domains systems have been prone to interference by endogenous tissue autoflourescence, although this limitation can be overcome through the use of multi-phase modulation techniques, which allow for separation of signals through determination of the differential φs corresponding to each signal. [42, 56] Fur-

---

[4] For the sake of brevity, only one exemplary detection method is described here; many other phase-sensitive detection techniques exist and could be adapted for this purpose.

thermore, the fiber-based, commercially available system most frequently employed for Fourier-domain oxygen measurements is by nature capable only of point measurements. While phase-sensitive cameras can be used in imaging applications to perform lifetime imaging, such applications are technically complex and infrequently described throughout the literature. [42, 57–59]

The techniques described above or variations thereof have enabled a host of studies involving measurement of intravascular pO_2 in a variety of tissue types including tumor, brain, retina, and heart. [55, 58, 60, 61] It is important to note, however, that with the notable exception of recent two-photon studies based on the chemical development of highly specialized phosphors, most of the studies described herein have utilized 2D planar imaging techniques and/or point measurements of oxygenation and are therefore subject to the inherent limits of such techniques, such as the inability to perform depth-resolved, tomographic measurements.[17, 61, 62] Furthermore, due to the tendency of most phosphorescent oxygen-sensitive probes to remain in the bloodstream and not cross cellular membranes, these studies mostly describe *intravascular* imaging, saying little about oxygen tension in avascular regions or on the cellular level.

2.3.4 MOLECULAR SENSOR DESIGN

As described in the preceding paragraph, most phosphorescence imaging studies in biological systems involve intravenous injection of oxygen-sensitive phosphors to enable oxygen tension measurement within the bloodstream. From a chemical and biophysical perspective, this poses a number of subtle challenges in terms of molecular probe design. First and foremost, blood contains a multitude of large soluble proteins such as albumin; to the extent that porphyrin sensors can interact with different proteins or even different microdomains within a single protein, this leads to an equilibrium scenario wherein at any given time the molecules of the molecular oxygen sensor may be experiencing a number of distinct chemical microenvironments. Because each of these microenvironments may vary in its exposure to dissolved oxygen, this in turn leads to a variation in the quenching constant k_q, and through it the observed phosphorescence lifetime τ (See Eqs. 2.5

and 2.6). [44] Problematically, this can result in a profoundly multi-exponential phosphorescence decay curve that is difficult to interpret. However, these interactions can also be beneficial, in that they can reduce the rate of quenching via k_q, thereby increasing the sensor's dynamic range and usefulness as a biological sensor. [44] Thus, protein interactions provide both pros and cons.

Inspired by both the beneficial aspects of protein interactions as well as a desire to overcome the problems they create, extensive effort has gone into development of synthetic modifications that tune a porphyrin's photophysical, kinetic, and chemical properties. [44] These efforts have largely involved advances in the synthesis of porphyrin dendrimers, structures in which an oxygen-sensitive porphyrin core is surrounded by homogeneous dendritic branches, also known as "dendrons" (Figure 2.3.2). These dendrons, the chemical structure of which can be modified to suit a particular imaging application, serve to solubilize the central porphyrin, alter the kinetics of its interaction with nearby proteins, and increase its dynamic range of oxygen sensitivity through modification of the quenching constant. [44]

An oxygen-sensitive porphyrin dendrimer that is frequently utilized and illustrates many of the above principles is Pd-meso-tetra-(4-carboxyphenyl)tetrabenzoporphyrin, a second-generation glutamate dendrimer also known as "Oxyphor G2" (Figure 2.3.2). [63]. The core of Oxyphor G2 is a meso-substituted, Pd-tetracarboxytetrabenzoporphyrin (PdTCTBP) with desirable absorption and emission properties. When dissolved in water and pumped at its absorption maxima of either 442 or 632 nm, second-generation PdTCTBP dendrimers phosphoresce at 790 nm with $\tau_0 = 267 \pm 5$ μs at 28 °C and pH = 7.4. [63] Without the second generation glutamate residues, however, the same central porphyrin is only sparingly soluble in water, prone to aggregation, and its phosphorescence is rapidly quenched such that the molecule is effectively non-emissive. [64] With the addition of a single glutamate generation (*i.e*, a single glutamate per carboxylic acid residue), the molecule becomes highly soluble as well as emissive, demonstrating a phosphorescence quantum yield of 11.5 % in deoxygenated H_2O as well as a quenching constant of 3054 ± 7 mmHg^{-1}s^{-1}. [64] Upon addition of a second generation of glutamate residues, (*i.e.*, completing the synthesis of Oxyphor G2), the quenching constant drops to 2821 ±5 $\text{mmHg}^{-1}\text{s}^{-1}$ due to the increased barrier layer provided for oxygen diffusion, a still-high number that gives the molecule a low dynamic range that is of questionable utility in biological sensing applications. Upon addition of saturating levels of bovine serum albumin (BSA), however, this number drops dramatically to 182 ±2 $\text{mmHg}^{-1}\text{s}^{-1}$, reflective of the additional shielding from oxygen provided by the protein.[5] [64] While this interaction with albumin does introduce some degree of binding microenvironment heterogeneity and therefore introduce multiexponential components into the phosphorescence decay curve, for the purposes of oxygen measurements there is literature consensus that approaches such as averaging or single-exponential force-fitting (as performed herein in Section 2.4) are appropriate and robust. [44] Notably, as of the authorship of this thesis, Oxyphor G2 is commercially available.

The synthesis of oxygen-sensing porphyrin dendrimers is a fascinating topic with a rich literature; for further review, interested readers are encouraged to consult the excellent book chapter by Vinogradov and Wilson. [44]

2.4 CLICK-ASSEMBLED OXYGEN SENSORS (CAOS) FOR USE IN MULTICELLULAR STRUCTURES

As described above in Section 2.2.3, individual lesions are host to heterogeneous tumor microenvironments that vary in their properties and response to drugs. [33, 40] In many cancers, including ovarian cancer (OvCa), drug resistance has been linked to the presence of hypoxia, which has been shown to reduce therapeutic efficacy through a variety of mechanisms. [33]

Overcoming this hypoxia-induced treatment resistance requires model systems capable of recapitulating the complex tumor environment observed in human disease. *In vitro* tumor models, such

---

[5] As described by Vinogradov *et al.*, dendrimer generations higher than 2 provide diminishing returns and introduce additional synthetic complexity. Second-generation glutamate dendrimers are therefore favored for most applications. [64]

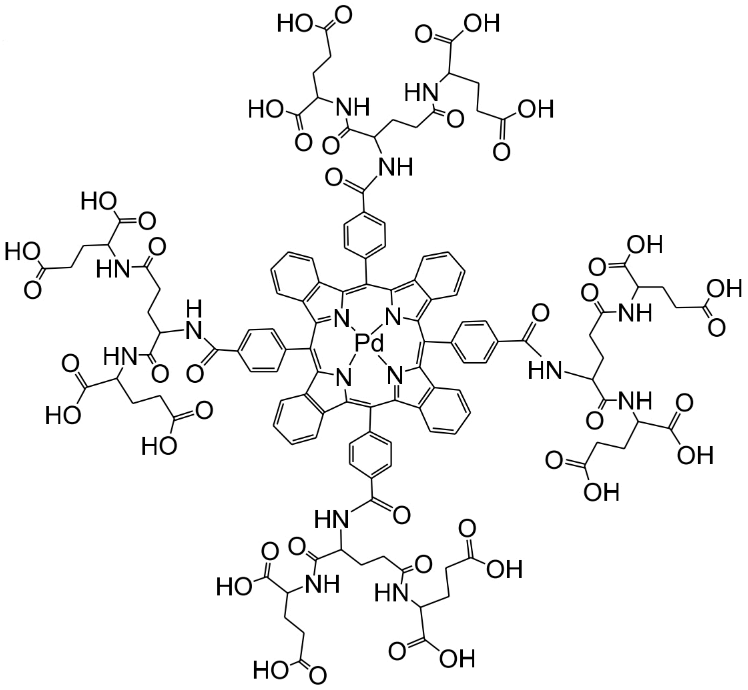

Figure 2.3.2: The chemical structure of Oxyphor G2. [63]

as OvCa 3D spheroid cultures, exhibit many of the features of *in vivo* metastatic lesions, such as the presence of a hypoxic cellular core, while also providing an environment that allows for consistent imaging at the same location before, during, and after therapy. [39, 40, 65] In principle, this approach enables a cell-by-cell correlation between microenvironmental factors such as hypoxia and therapeutic response. The ability to incorporate hypoxia imaging into this platform, however, has been hampered by the absence of cellular-resolution oxygen sensing methods capable of performing depth-resolved imaging studies in *in vitro* model systems. Although phosphorescence lifetime imaging has been used to quantify *in vivo* oxygenation in a variety of tissue types as discussed in Section 2.3.3, non-perturbative measurements of intracellular oxygen tension deep in tissue and methods for delivering oxygen sensors through hundreds of microns of avascular cellular layers to hypoxic tumor regions have not yet been achieved. While multiple groups report the delivery of oxygen sensors across cellular membranes in *in vitro* monolayer culture systems, these approaches collectively suffer from toxicity, poor cellular uptake or the the mandatory use of perturbative delivery techniques, and/or blue shifted emissions that render them unsuitable for use in tissue imaging due to optical scattering. [46, 66–72]

Moreover, the molecular oxygen probe Oxyphor G2 (Figure 2.3.2), while well-characterized and commercially available, is incapable of spontaneously penetrating into cells or multicellular structures (Figure A.1). We conducted experiments demonstrating that conjugates created using high molecular weight polycationic polyethylene imine (MW $\approx$ 25,000), known for its ability to traverse cellular membranes, could not deliver Oxyphor G2 throughout OvCa without significant toxicity. [46, 73, 74] Similarly, surface modification of Oxyphor G2's glutamate dendrimers with cationic ethylenediamine did not result in a construct capable of penetrating cells, and screening of other similar polycationic carrier compounds was additionally unsuccessful.

This section describes the development of oxygen-sensitive, click-assembled oxygen sensing (CAOS) nanoconjugates comprising novel poly(amidoamine)-like dendrons and demonstrates their spheroid-penetrating abilities. [39, 65] Our nanoconjugate's combination of NIR emissivity, lack of toxicity at functional doses, and ability to spontaneously penetrate hundreds of microns into 3D tumor models within hours renders it unique among oxygen sensors, enabling oxygen-sensitive imaging at $>$100 μm depths using NIR-optimized confocal microscopy. Furthermore, the modular synthetic approach described herein enables the synthesis of higher generation dendrons in days, whereas traditional syntheses of dendrimers with similar chemical properties and generation can take weeks, months, or longer and result in very low yields. [75, 76] The CAOS nanoconjugate's ability to spontaneously penetrate multiple cellular layers overcomes a key barrier to the use of *in vitro* tumor models as a hypoxia model system, while also enabling a host of other applications such as oxygen-sensitive imaging in poorly- or non-vascularized tissue regions.

As described in Section 2.3.4, many oxygen sensors are dendrimeric structures, in which an oxygen-sensitive porphyrin core is surrounded by dendritic branches, or dendrons. In protein-free solutions, these dendrons serve to both solubilize the central porphyrin and modulate its dynamic range of oxygen sensitivity. In protein-rich environments such as the bloodstream, non-PEGylated dendrimers have been shown to interact extensively with endogenous proteins; this interaction can decrease the rate of oxygen quenching by an order of magnitude or more. [44] We have observed that fourth generation, dye-tagged poly(amido) amine (G4 PAMAM) "starburst" dendrimers were taken up by monolayer OvCa cultures after 40 minutes (Figure 2.4.1); the same molecule penetrated throughout >250 μm diameter OvCa 3D spheroids after 3.5 hours at low concentrations (500 nM) with no observable toxicity (Figure 2.4.2). PAMAM dendrimers, first synthesized in 1979 by Tomalia *et al.*, are hyperbranched, highly stable, ordered molecules incorporating a large number of tertiary and primary amine groups (pKas of 6.85 and 3.86, respectively); at biological pH, these amine groups retain a positive charge, rendering the overall structure highly polycationic (Figures 2.4.3 and 2.4.4). [76–78] PAMAMs and structural derivatives thereof have been investigated for use in a variety of applications, including transepithelial and oral drug delivery.[77]

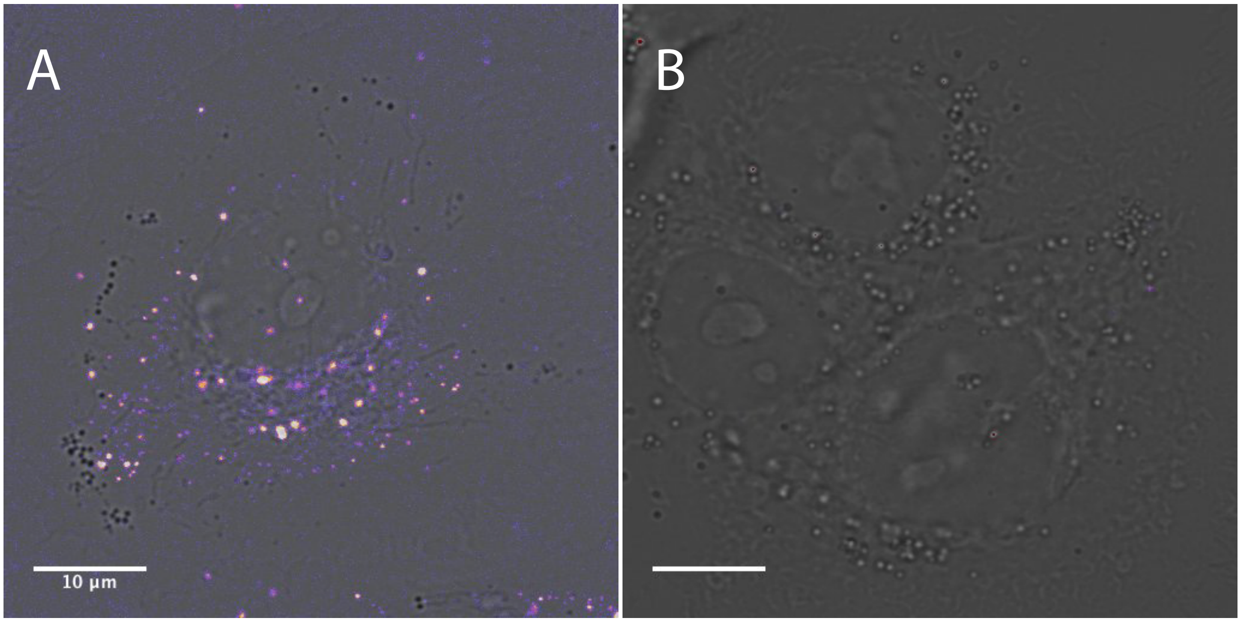

Figure 2.4.1: AlexaFluor 488-PAMAM G4 conjugates readily penetrate monolayer OVCAR5 cells. **A**: OVCAR5 cells treated with 500 nM AlexaFluor 488-PAMAM G4 conjugate for 45 minutes exhibit a punctuate localization pattern consistent with lysosomal uptake. (Purple = AlexaFluor 488-PAMAM G4 conjugate). **B**: Monolayer OVCAR5 cells, no treatment control.

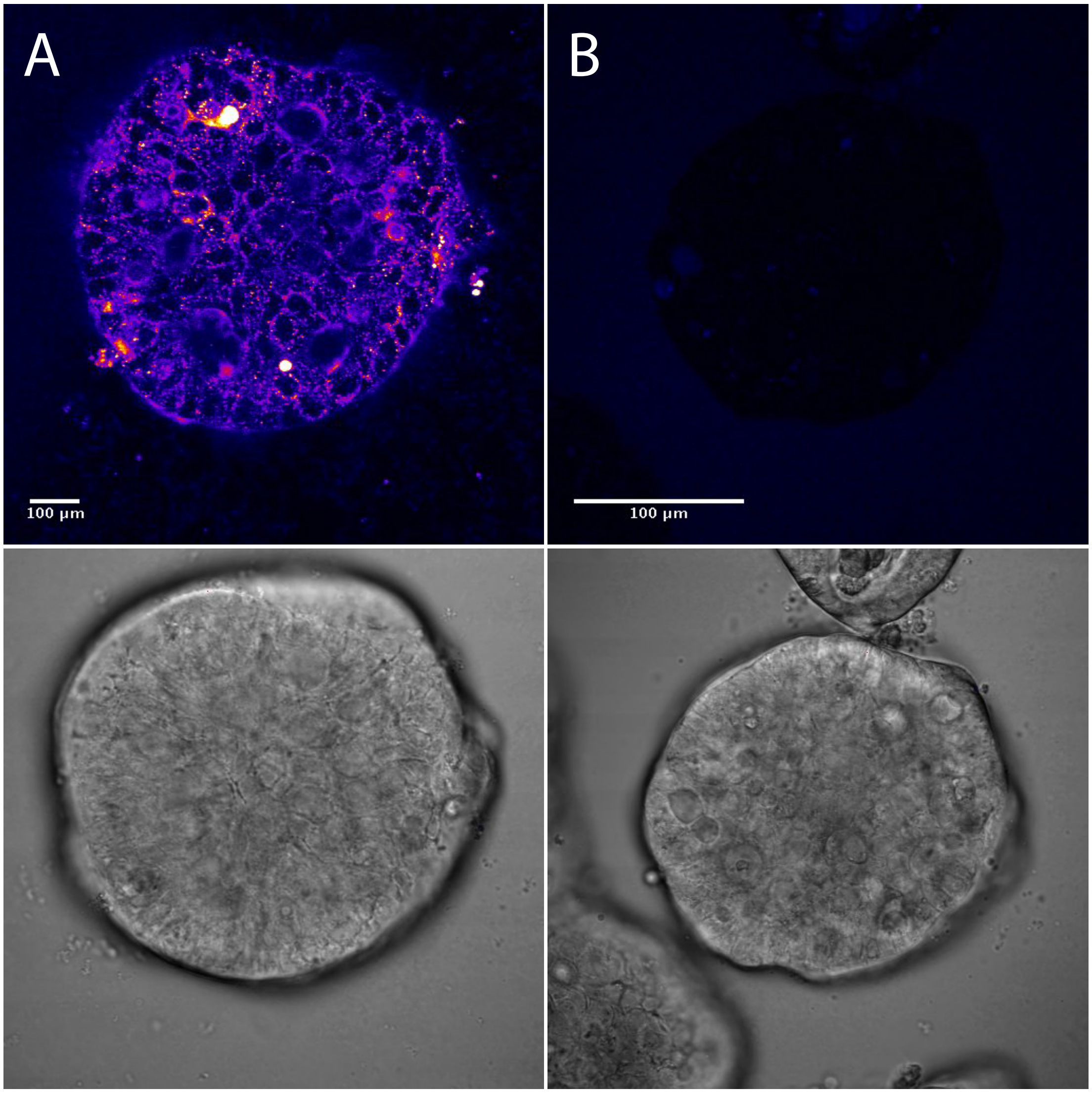

Figure 2.4.2: AlexaFluor 488-PAMAM G4 penetrates large OvCa 3D spheroids, but AlexaFluor 488 carboxylic acid does not. **A**: OvCa 3D spheroids treated with 500 nM AlexaFluor 488-G4 PAMAM conjugate for 3.5 hours. Imaged using multiphoton excitation for enhanced depth penetration. (Purple = AlexaFluor 488-PAMAM G4 conjugate). **B**: AlexaFluor 488 carboxylate does not penetrate OvCa 3D spheroids. Spheroids treated with 500 nM AlexaFluor 488 carboxylate for 3.5 hours.

Much of the interest and excitement regarding PAMAMs stems from their chemical stability, the low polydispersity of synthetic products achieved during their synthesis, and the ease with which PAMAMs and their synthetic intermediates can be isloated.[77, 79] While desirable from a process engineering, manufacturing, and applications perspective, the aforementioned properties were achieved through the development of a synthetic methodology that relies on "gentle" chemical reactions that take place in the absence of a catalyst, additional reagents, or extreme conditions; although this serves to simplify the purification of the final product and synthetic intermediaries thereof, it also makes synthesis of PAMAM dendrimers extremely slow and requires a divergent scheme in which additional structural units, or "generations," are added to a monofunctionalized, bifunctionalized, or multifunctionalized core. [76, 80] Thus, a single reaction in the synthesis of higher generation PAMAM structures can take weeks, months, or even longer. A typical PAMAM synthesis scheme and a schematic illustrating the structure and nomenclature of higher generation dendrimers are shown in Figures 2.4.3 and 2.4.4, respectively. [79]

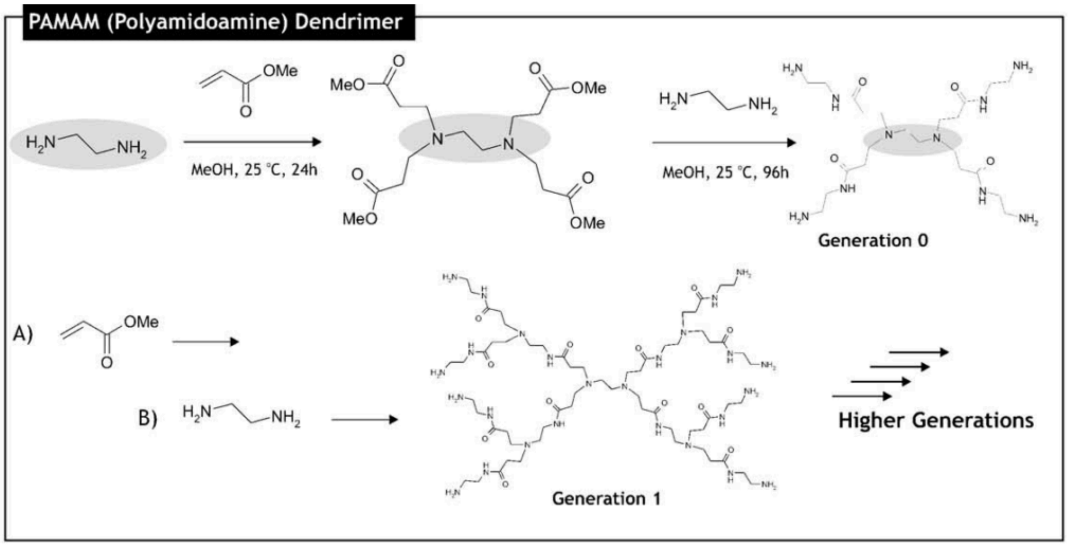

Figure 2.4.3: A representative synthesis of a first-generation (G1) PAMAM. Synthesis of higher generations is required to achieve low toxicity and cellular permeability and can take months or more. Reproduced from [79].

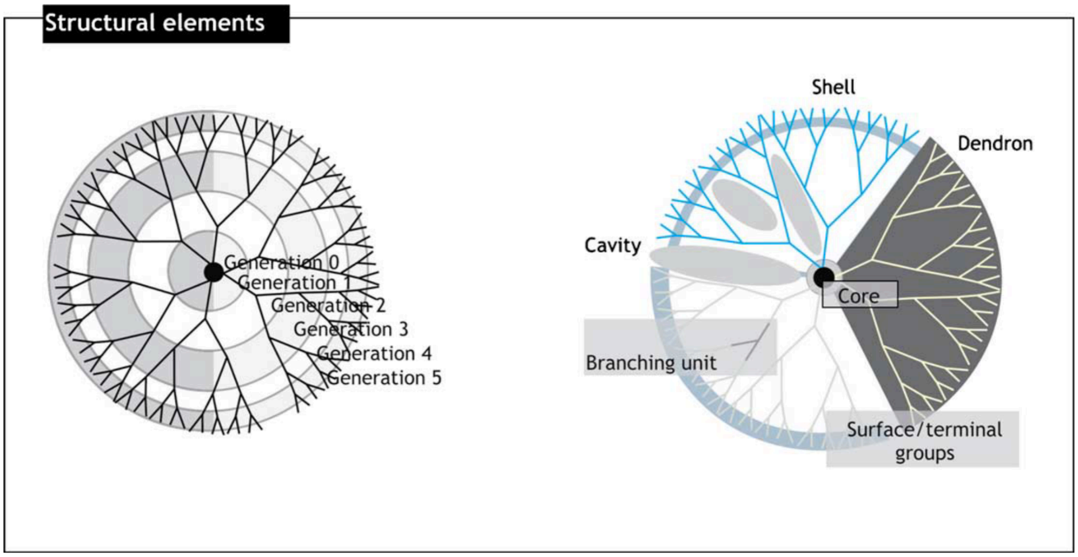

Figure 2.4.4: Illustrative structure and nomenclature of a generalized "starburst" dendrimer. Reproduced from [79].

In addition to being readily endocytosed, PAMAM dendrimers are known to form complexes with proteins such as bovine serum albumin (BSA), analogously to Oxyphor G2. [77, 81] We therefore reasoned that a phosphorescent porphyrin coupled to one or more higher-generation ($\geq$G2) PAMAM dendrons would benefit from the cell- and spheroid-penetrating properties of PAMAM while also interacting with cellular proteins, thereby creating an oxygen sensor with a useful dynamic range for biological experiments. [77, 81] For this work, we selected Pd-tetracarboxytetrabenzoporphyrin (PdTCTBP) as our phosphorescent porphyrin core because its lifetime properties have been characterized in the literature, its synthesis is well-known, and its near-infrared emission (810 nm) lies in the "optical window" ideal for tissue imaging. Additionally, its spectral profile minimizes overlap with known regions of intense autofluorescence, and it can be excited by readily available laser lines (445 nm and 635 nm). [44]

Disappointingly, initial attempts to modify and/or couple commercially available PAMAM dendrons to PdTCTBP resulted in unusably low yields despite the use of a number of synthetic strategies, most likely due to steric hindrance. To create a spheroid-permeable oxygen sensor, we therefore developed a "click"-based strategy to rapidly assemble PAMAM-like subunits and couple them to an oxygen-sensitive porphyrin core. "Click" chemistry, a term popularized by Nobel laureate Barry Sharpless in the early 2000s, describes a synthetic chemical approach that satisfies a number of challenging yet desirable criteria. In one of the earliest papers using the term, Sharpless and colleagues describe click chemistry as follows:

> Following nature's lead, we endeavor to generate substances by joining small units together with heteroatom links (C-X-C). The goal is to develop an expanding set of powerful, selective, and modular "blocks" that work reliably in both small- and large-scale applications. We have termed the foundation of this approach "click chemistry," and have defined a set of stringent criteria that a process must meet to be useful in this context. The reaction must be *modular*, *wide in scope*, give *very high yields*, generate only *inoffensive byproducts* that can be removed by nonchromatographic methods, and be *stereospecific* (but not necessarily enantioselective). The required process characteristics include *simple reaction conditions* (ideally, the process should be insensitive to oxygen and water), *readily available starting materials and reagents*, the use of *no solvent or a solvent that is benign* (such as water) *or easily removed*, and *simple product isolation*. Purification- if required- must be by nonchromatographic methods, such as crystallization or distillation, and the product must be stable under physiological conditions. [82]

Although in principle the term "click chemistry" can be used to describe any reaction that meets this criteria, it is most often used to describe the Cu(I)-catalyzed Huisgen 1,3-dipolar cycloaddition. This reaction occurs at room temperature with exquisite specificity between an alkyne group and an aliphatic azide, yields no synthetic byproducts, and the reactants are orthogonal to most known biomolecules under physiological conditions. [83] Although further review of "click" chemistry developments and applications are beyond the scope of this thesis, the proposed mechanism of the Cu(I)-catalyzed Huisgen 1,3-dipolar cycloaddition used throughout this paper is described in Figure 2.4.5 as a courtesy to the interested reader.

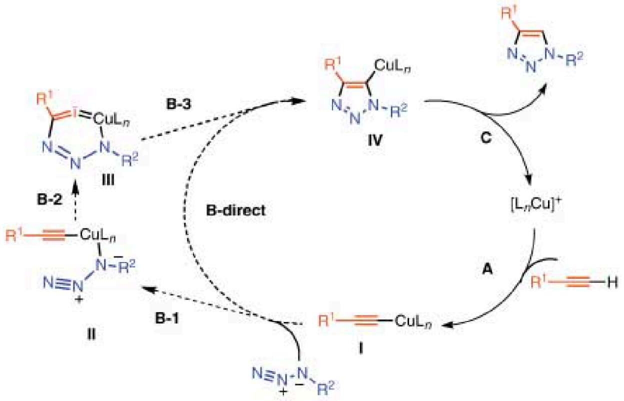

Figure 2.4.5: A proposed mechanism for the Cu(I)-catalyzed Huisgen 1,3-dipolar cycloaddition. Reproduced from [83].

PAMAM dendrons with azide/alkyne functionality have been reported in the literature, but like other PAMAM dendrons/dendrimers they problematically make use of extremely slow reactions and require months or longer to synthesize. [84] To overcome this practical limitation, we developed a scheme that enables rapid *assembly* of PAMAM-like dendrons from three branched subunits that can be synthesized in parallel (Figures2.4.6 and 2.5.1). Briefly, it relies on the differing lability of triethylsilyl (TES) and triisopropylsilyl (TIPS) alkyne protecting groups, allowing for sequential subunit ligations while avoiding indiscriminate polymerization (Figures 2.4.6, 2.5.2): first, the TIPS-protected "starting" subunit **1d** is reacted with 2 equivalents of the "intermediate" subunit **2c** and catalytic quantities of sodium ascorbate and $CuSO_4$. Following isolation of the reaction product **4a**, the TES protecting groups are removed using mild conditions that leave the focal-point TIPS protecting group intact, yielding **4b** and preparing the growing dendron for another ligation round. Primary amine functionality can then be added by ligation of "final" subunit **3b** to create **4c**, the focal group alkyne of which is then deprotected using tetrabutylammonium fluoride to yield **4d**. [85] Each dendron growth phase can be conducted overnight, and the product can be isolated without the use of chromatography. This allows higher-generation, triazole-bridged, PAMAM-like dendrons to be synthesized in a matter of days as opposed to months.[6] Once complete, the dendrons can be conjugated to any azido-functionalized central moiety in a single convergent step. In this study, we coupled the dendrons to Pd-tetraazidotetrabenzoporphyrin, an azido-functionalized PdTCTBP derivative (Figure 2.5.3).

---

[6] Although in principle this approach can be used to synthesize PAMAM-like dendrons of an arbitrary generation, for the purposes of this project we stopped at the second generation. Note that ligating this second generation dendron to the tetraazido- phosphorescent core (Figure 2.4.6) creates a third-generation dendrimer nanoconjugate, as the overall structure contains three sets of dendron subunit layers.

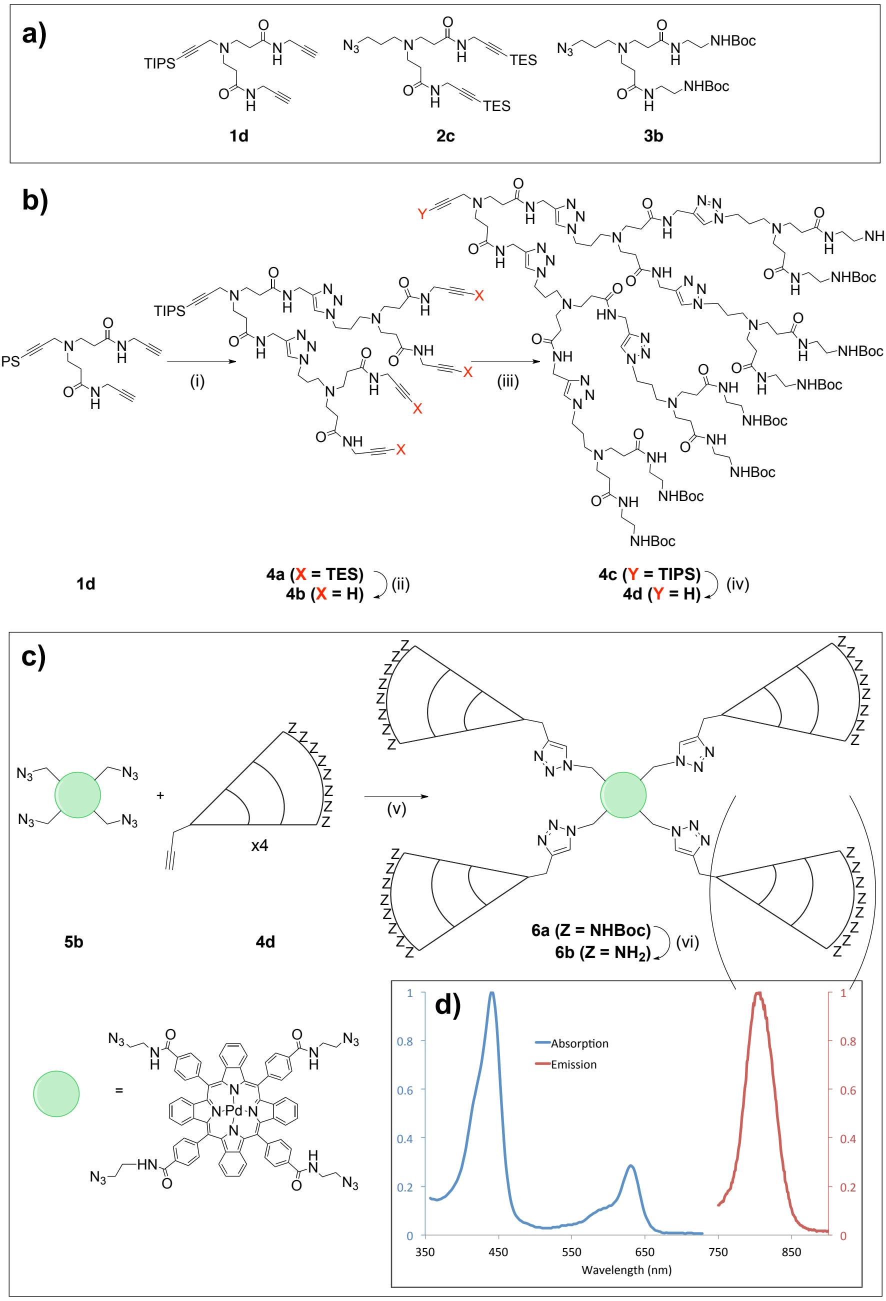

Figure 2.4.6: Generalized overview of the synthetic scheme used in the synthesis of CAOS nanoconjugates. **A**: Dendron subunits used in the assembly of the PAMAM-like dendron. Numbering refers to the labeling scheme used in the supplemental information; importantly, the TES and TIPS protecting groups differ in their lability. **B**: Synthesis of G3 PAMAM-like dendrons through sequential click ligation of subunits. i) 1 eq. **1d**, 2 eq. **2c**, 0.2 eq. $CuSO_4$, 0.4 eq. sodium ascorbate, DMF/H_2O, r.t.; ii) 50 eq K_2CO_3, MeOH, 36h, r.t.; iii) 1 eq. **4b**, 4 eq. **3b**, 0.2 eq. $CuSO_4$, 0.4 eq. sodium ascorbate, DMF/H_2O, r.t.; iv) 5 eq. TBAF, THF, r.t.. **C**: Overview of the convergent nanoconjugate assembly step. v) 1 eq. **7b**, 5 eq **4d**, 12 eq. $CuSO_4$, 24 eq. sodium ascorbate, DMF/H_2O, r.t.; vi) TFA, DCM, r.t.. **D**, inset: Normalized absorption and emission spectra of the G3 CAOS nanoconjugate.

Using this sequential click method, we synthesized third-generation (G3) CAOS nanoconjugates from G2 PAMAM-like dendrons. As can be seen in Figure 2.4.6, the penultimate step in our synthetic scheme involves ligating the dendron **4d** to the Pd-tetraazidotetrabenzoporphyrin core (**5b**), which is capable of reacting with up to four equivalents of dendrons. In practice, a distribution of adducts was observed. These G3 CAOS nanoconjugates were characterized via NMR and MALDI-TOF MS as being composed of mono-, di- and tri-dendron adducts; NMR integration suggests that, on average, between two and three dendrons are attached to each nanoconjugate (Figures 2.5.4, B.21-B.23).

G3 CAOS nanoconjugates were studied in a dense, protein-rich environment and were found to exhibit uniform oxygen sensitivity. To evaluate the photophysical properties of G3 CAOS, we dissolved the nanoconjugate in 2% bovine serum albumin (BSA) and monitored its phosphorescence lifetime as a function of pO_2. [44] Recall that oxygen quenching of phosphorescence lifetime is traditionally described using the Stern-Volmer relationship (Eq. 2.6), where τ is the exponential lifetime of the phosphor, k_q is the quenching coefficient, pO_2 is the partial pressure of dissolved oxygen, and τ_0 is the exponential lifetime of the phosphor in the absence of oxygen. [44] k_q is a function of the phosphor's chemical environment and reflects the sensor's dynamic range; in general, a lower k_q of <1000 mmHg^{-1}s^{-1} is desirable. We compared the k_q and τ_0 of G3 CAOS to Oxyphor G2 (Figure 2.4.7, 2.4.1), which possesses a PdTCTBP core surrounded by second generation glutamate dendrons. Given that both molecules possess the same phosphorescent core but have different dendron functionalities, G3 CAOS should therefore exhibit a similar τ_0 but a different k_q relative to Oxyphor G2. As expected, we observed that the order of magnitude of the k_q observed for G3 CAOS is consistent with that of Oxyphor G2, the calibration is linear, and the dynamic range is sufficient for oxygen measurement across physiological ranges. [44, 63]

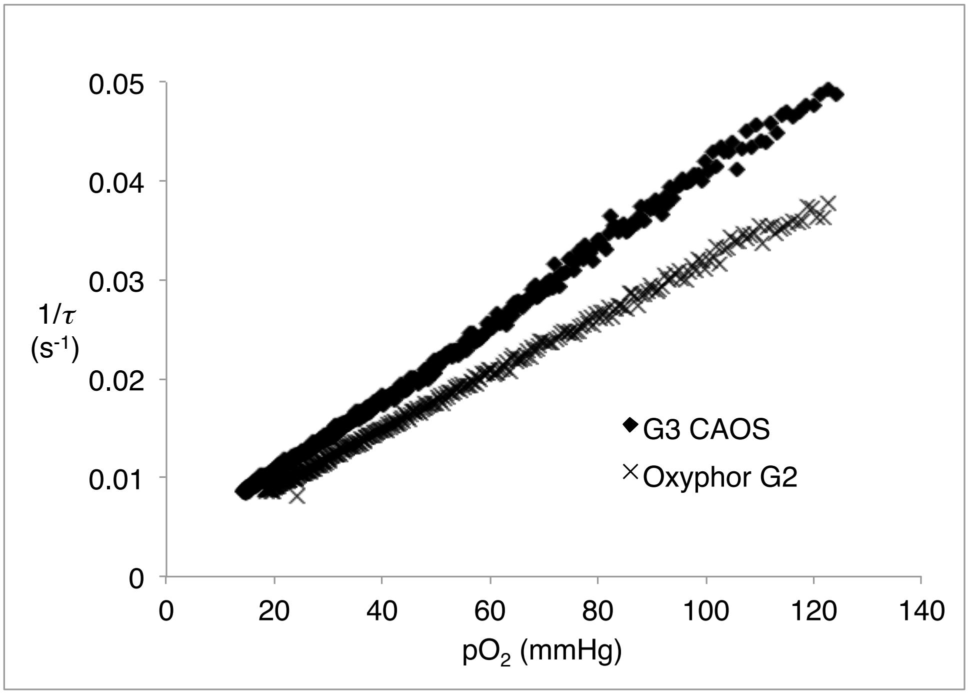

Figure 2.4.7: Calibration data for G3 CAOS and the commercially available Oxyphor G2. τ = phosphorescence lifetime (s).

	$\tau_o(\mu s)$	$k_q(\mathrm{mmHg^{-1}s^{-1}})$
G3 CAOS	173	377
Oxyphor G2	178	283

Table 2.4.1: Calibration constants for G3 CAOS and Oxyphor G2. τ_o = phosphorescence lifetime in zero oxygen, k_q = phosphorescence quenching constant.

Having verified that G3 CAOS nanoconjugates exhibit the desired calibration properties, we next tested their uptake in cells. Given the low quantum yield ($< 1\%$) of PdTCTBPs in ambient oxygen conditions and the low NIR throughput and sensitivity of commercially available microscopes, we first tagged G3 CAOS with AlexaFluor 488 to enable straightforward visualization of the G3 CAOS's subcellular localization using confocal fluorescence microscopy.[7] Confocal imag-

---

[7] The ever-attentive reader will note that the quantum yield of the same porphyrin in deoxygenated solution was earlier cited to be greater than 11%; this demonstrates the strong oxygen-dependence of quantum yield, as oxygen quenching offers a competitive and non-emissive energetic relaxation.

ing of OvCa cells treated for 40 minutes with 500 nM AlexaFluor 488-G3 CAOS confirmed uptake and a punctate subcellular localization pattern consistent with lysosomal uptake (Figure 2.4.8), as described by previous reports. [77] An MTT viability assay confirmed the lack of toxicity at all doses used (1 μM - 10 μM, Figure A.2).

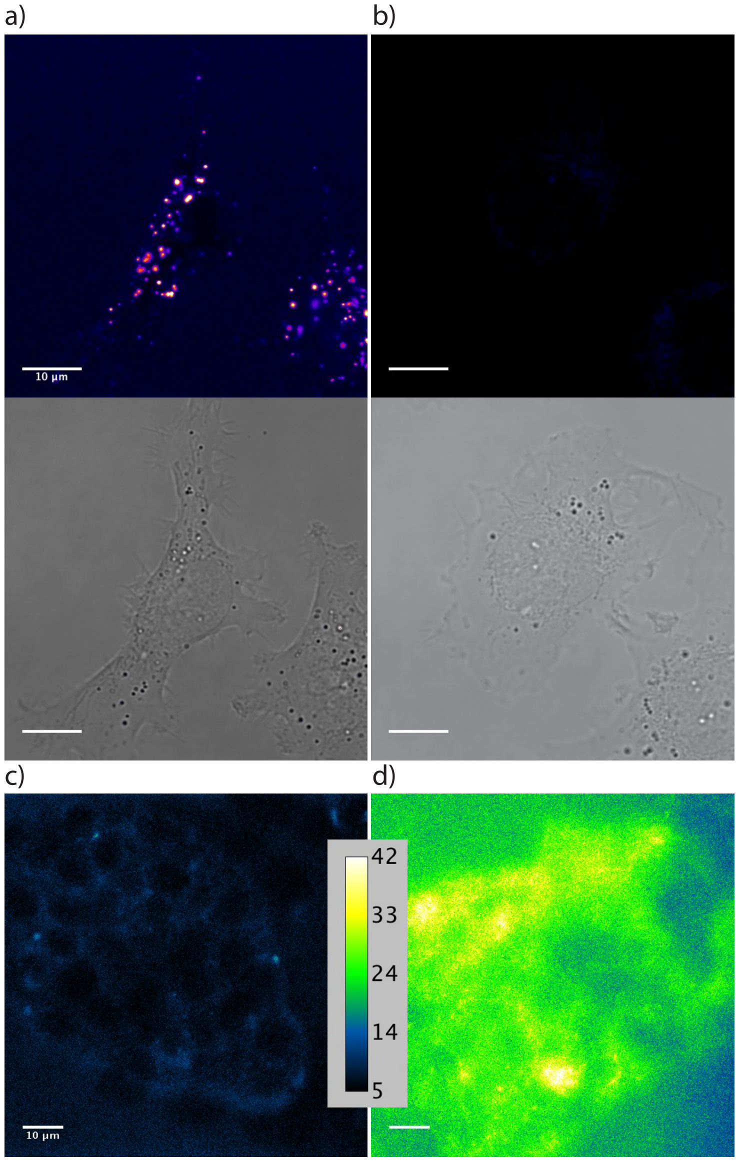

Figure 2.4.8: Confocal fluorescence and NIR phosphorescence microscopy verifies the spontaneous uptake of G3 CAOS probes and their response to oxygen changes. **A**: Monolayer OVCAR5 cells treated for 40 minutes with 500 nM AlexaFluor 488-G3 CAOS (false color, purple) exhibit a punctate subcellular localization pattern consistent with lysosomal uptake. **B**: Monolayer OVCAR5 cells, no treatment control. Note that the difference in background between **A** and **B** is attributable to small amounts of binding of the positively-charged G3 CAOS to the culture dish. **C**: False color image of monolayer OVCAR5 cells treated for one hour with 1.5 μm G3 CAOS, imaged under room air. Legend bar: phosphorescence photon count. **D**: Monolayer OVCAR5 cells treated for one hour with 1.5 μm G3 CAOS, imaged after a nitrogen purge. Note that **A** and **B** were acquired in a separate experiment using the Olympus FV1000 confocal microscope, whereas **C** and **D** were acquired using the custom confocal phosphorescence microscope described in 2.5.12.

To image the weak, oxygen-dependent phosphorescence of the G3 CAOS nanoconjugates, we built a single-photon counting confocal microscope and optimized its performance for imaging in the 800-900 nm NIR wavelength range corresponding to G3 CAOS's emission (Figure 2.5.6). We used this system to confocally image the phosphorescence of non-labeled G3 CAOS in monolayer-plated OvCa cells, thereby demonstrating our successful creation of a cell-penetrating oxygen-sensitive nanoconjugate (Figure 2.4.8).[8] We also observed the phosphorescence intensity's inverse dependence on pO_2, noting a two- to four-fold increase in signal following a purge of the cell culture dish with nitrogen, consistent with the increase observed in other early phosphorescence imaging experiments. [48]

Using this photon-counting NIR confocal microscope, we confirmed that G3 CAOS nanoconjugates penetrate 3D OvCa spheroids. Prior to imaging, spheroids were incubated with 2 μM G3 CAOS for four hours. 3D volume acquisition with confocal optical sectioning revealed that phosphorescence signal could be observed throughout each spheroid at depths exceeding 100 μm, whereas signal was not observed in untreated spheroids (Figure 2.4.9). Finally, to confirm that the probe is sensitive to oxygen levels, we purged the culture dish with nitrogen, and observed that spheroids exhibited an approximate doubling of phosphorescence signal. To avoid the influence of photobleaching, different spheroids were imaged before and after the nitrogen purge.

---

[8] The wonderfully attentive reader will note the apparent difference in staining pattern between Figures 2.4.8a-b and 2.4.8c-d. This imaging artifact is due to the reduced spatial resolving power of the custom-built NIR phosphorescence imaging system used in c-d relative to the commercial fluorescence system used in a-b, a phenomenon for which there are two independent explanations. First, the use of an 850 nm NIR-emissive probe reduces the maximum diffraction-limiting resolution relative to A488 (approximately 354 nm vs. 203 nm, respectively). Second, more subtly, and most importantly, is that the pixel densities used for each image differ, a conscious design choice made to facilitate more rapid phosphorescence imaging. The images of cells treated with G3 CAOS-488 were acquired on an Olympus FV1000 with a 60x objective set to a zoom of 3.5x, whereas the images of G3 CAOS alone were acquired on a custom-built microscope with an effective 60x objective set to a zoom of 1x (see Sections 2.5.12 vs. 2.5.9); both images were acquired using approximately the same number of total pixels (512 x 512 for the Olympus, 500 x 500 for the custom phosphorescence microscope). Thus, *ceteris paribus*, a given area imaged using the phosphorescence microscope will be sampled by fewer pixels than the same area imaged using the FV1000. In the context of imaging weakly emissive phosphors, this is beneficial as it results in more phosphor molecules per pixel, generation of more intense phosphorescence, and shorter required imaging/dwell time per pixel. However, this also leads to spatial under-sampling of the lysosomes in each cell relative to the FV1000, leading to the microscope's inability to resolve finer structures and the observed loss of punctate appearance. This balance between imaging speed and resolving power is a common trade-off made when imaging weakly emitting species such as oxygen-sensing phosphors.

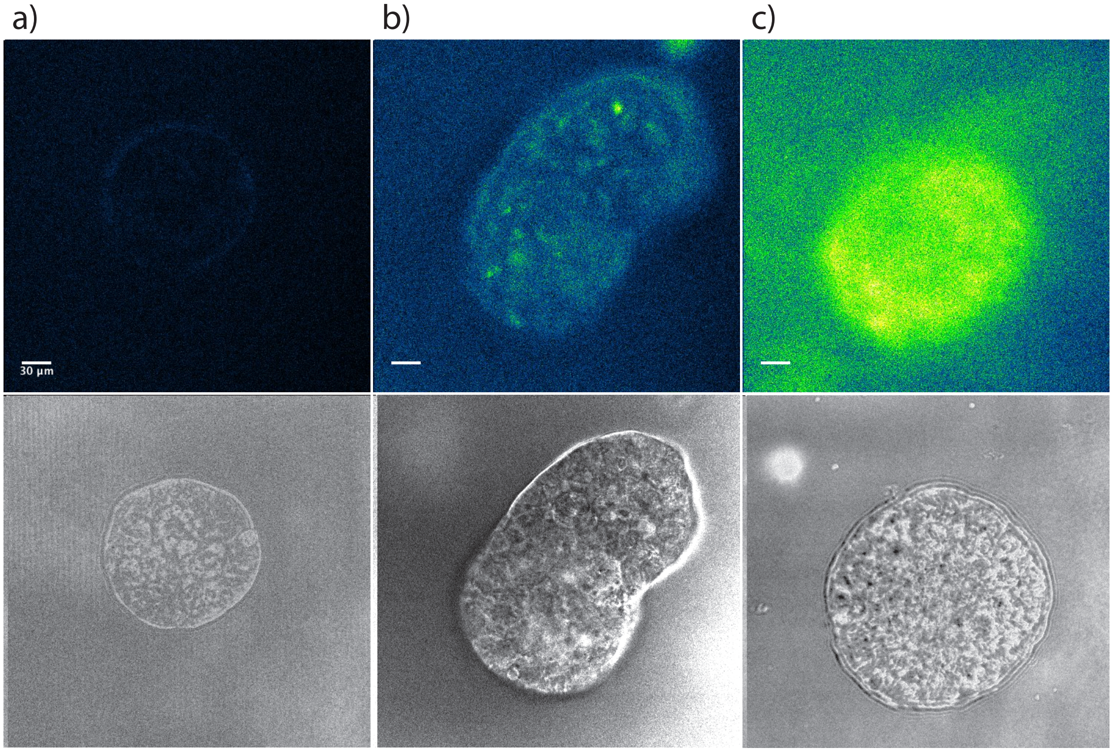

Figure 2.4.9: NIR Phosphorescence confocal microscopy imaging reveals that G3 CAOS probes spontaneously penetrate 3D OvCa spheroids. **A**: 3D OvCa spheroids, no treatment control (bottom/grey: transmission channel). **B**: False-color image of spheroids treated for 4 hours with 2 μM G3 CAOS, imaged under room air. Legend bar: phosphorescence photon count **C**: Spheroids treated for 4 hours and imaged after a nitrogen purge. All images were acquired at the approximate midpoint along the z-axis of each spheroid, corresponding to an approximate depth of 100 μm.

Taken together, these data show that we have developed a novel approach for the synthesis of oxygen-sensitive nanoconjugates and provided proof-of-concept that click-assembled nanoconjugates can be used as deep tissue imaging agents for 3D oxygen-sensitive imaging. Our novel assembly strategy does not require the long reaction times typically necessary to achieve higher generation dendrons. Future work in this area will involve the synthesis and testing of a ratiometric CAOS nanoconjugate, which would facilitate more straightforward calibration and quantitative oxygen mapping in the complex cellular environment. Additionally, we chose PdTCTBP for an initial demonstration of the CAOS approach due to the extensive body of work describing its use for quantitative oxygen measurements in biological systems;[44] future work will make use of phosphorescent porphyrins with a higher quantum yield, thereby enabling imaging on less specialized microscopes and reducing the barrier to the use of CAOS-type nanoconjugates in biological experiments.

2.4.1 Future directions and work

The above project demonstrates proof-of-concept that NIR-emissive phosphorescent oxygen-sensing porphyrins can be delivered to depths of hundreds of microns through multicellular, avascular structures; it additionally shows that these porphyrins retain their oxygen sensitivity and that their emission can be imaged using confocal microscopy techniques and modest pixel dwell times (approximately 10 μs; see Section 2.5). Although these are crucial milestones in the development of a useful, quantitative system capable of optically measuring oxygen in solid tumors and other tissues, many hurdles remain to be crossed before this goal becomes reality. First and foremost, a protocol must be developed that enables effective and reliable calibration of such sensors in the intracellular environment. This task is challenging for a number of reasons: as discussed in Section 2.3.4, the phosphorescence lifetime/intensity of phosphorescent dendrimers is highly dependent on the chemical environment surrounding each probe molecule and the proteins with which the molecule is interacting. If the average protein distribution within a single sample differs from cell to cell, or even across subcelluar organelles within a single cell (*e.g.*, lysosomes), this might cause equivalent oxygen tensions to yield different lifetimes or intensities as a function of spatial location, thereby making it challenging to generate a universal calibration valid in all spatial locations. One potential solution to this problem would be to employ chemical means to better insulate the dendrimer core from protein interaction, thereby reducing the effects of heterogeneity in the biochemical microenvironment. Rozhkov *et al.* demonstrate that phosphorescent oxygen-sensing dendrimers coated in short-chain poly(ethylene glycol) (PEG) demonstrate identical calibration curves in PBS and dense albumin solution, a fact putatively attributable to the outer PEG layer's ability to chemically block heterogeneous protein interactions. [44, 86]

While effective for blood-borne oxygen sensing dendrimers that can simply be injected into the blood stream intravenously, PEGylation could be problematic for CAOS-style molecular probes intended for intracellular use, in that the presence of PEG dendrimers could alter the probe's uptake properties. A potential solution involves ligation of uptake-enhancing targeting moieties such as RGD or folate to the dendrimer surface. Cyclic RGD peptide has been demonstrated to enhance cellular uptake of ligated molecular cargos such as PAMAMs and upconverting nanophosphors. [87–93] In a 2012 publication, Guo *et al.* demonstrate that ligation of multiple (≥ 3) 5 kDa PEG moieties to a CyAL5.5 fluorophore serves to both enhance the fluorophore's quantum yield as well to protect it from "troublesome interactions" with endogenous biomolecules. The authors additionally show that this approach can be combined with molecular targeting through additional ligation of an RGD targeting moiety to the PEGylated conjugate to achieve targeted uptake. [93] This method, which the authors term "PEG-fluorochrome shielding," could be applied to both facilitate uptake of phosphorescent dendrimers as well as to homogenize their phosphorescence lifetime in a variety of biological contexts. Alternatively, folate has been observed to achieve both molecular specificity of binding as well as targeted uptake, in particular for folate receptor expressing variants of tumors such as many ovarian cancers; folate targeting could therefore be considered a supplement to or replacement for RGD-based approaches. [94–101]

It is important to note that the calibration of phosphorescent pH sensors such as Oxyphor G2 is pH sensitive; thus, the presence of intracellular pH variation (*i.e.*, cytoplasm vs. lysosomes) could itself affect the accuracy of oxygen measurements. [63] However, for the illustrative example of Oxyphor G2, this effect is small (1-2% of τ_0, within error for k_Q). If dendrimer pH sensitivity were indeed to prove problematic during calibration, modification to the dendrimer surface groups (*e.g.*, PEGylation of carboxylic acid groups) could be performed to reduce the molecule's overall pH sensitivity.

At present, our evidence suggests CAOS sensors exhibit a lysosomal uptake pattern, although this has been difficult to definitely confirm using phosphorescence imaging in part due to the resolution-related reasons described in a footnote above. Importantly, from the calibration perspective, the tendency of CAOS sensors to localize to subcellular organelles has the potential to create challenges, as there exists no "gold standard" comparator method capable of achieving subcellular resolution against which to compare and verify our results. It will nonetheless be important to rigorously demonstrate that the probe's performance at a given oxygen level is independent of its subcellular environment. One approach would be to perform a series of point lifetime measurements across all subcellular environments to which CAOS sensors localize and show that the response is similar across all tested points. This could be performed by fluorescently tagging the CAOS sensor to facilitate visualization of subcellular probe localization via confocal microscopy, allowing cells to take up the probe, then varying the partial pressure of oxygen present in the media and collecting separate point phosphorescence lifetime traces from all cellular organelles to which the sensor localizes. In principle, this experiment could also be conducted in a wide-field geometry with a time-resolved camera, although the focal blurring resulting from the absence of a confocal pinhole might make resolution of subcellular compartments difficult. Note that in both experiments, great care would have to be taken to avoid photodamage and/or photolysis of subcellular organelles.

In reality, the experiments described above could be complicated by the presence of local oxygen gradients within the cell, for example, in regions proximal to the mitochondria; this would create a scenario wherein it would be impossible to differentiate "real" changes in pO_2 from changes related to differential subcellular microenvironments. One possible means by which to overcome this challenge would be to arrest primary oxygen-consuming cellular processes (*i.e.*, oxidative phosphorylation) using mitochondrial poisons such as cyanide and acquire phosphorescence lifetime data before and after at each datapoint. An alternative protocol could involve allowing monolayer cells to take up CAOS sensors, then fixing and permeabilizing the cells to eliminate oxygen consumption; this would preserve local biochemical environments while arresting all active cellular processes, thereby rendering cells as passive biochemical spectators throughout the calibration process.

Although this work demonstrates oxygen-sensitive intensity imaging, it does not report *quantitative* oxygen imaging, as the pixel intensities represent photon counts/intensities and not oxygen lifetimes *per se*. Although widefield, non-time-resolved images reporting phosphorescence intensity can be used for quantitative oxygen sensing in certain situations (see Chapter 3), quantitative confocal microscopy of phosphoresce intensity is challenging for a number of reasons, including but not limited to impractical imaging times, phosphor photobleaching, and cellular damage through generation of singlet oxygen. Confocal phosphorescence lifetime imaging suffers from similar drawbacks, as the dwell time and per-pixel imaging parameters required are similar. To overcome this barrier, our group is currently exploring numerous alternatives. One such approach involves conjugation of an oxygen-insensitive fluorophore to the oxygen sensitive phosphor, thereby creating a self-referencing, ratiometric sensor that can be read using hyperspectral or dual-channel imaging instead of lifetime imaging. Calibrations achieved using this approach have been demonstrated by our group and others to be linear and effective.[42, 44, 66–68, 70–72, 102, 103]

While this approach is in principle straightforward, its implementation in the tissue environment poses subtle challenges. First, optical imaging in tissue is ideally conducted in the NIR "optical window" due to reduced tissue scattering and absorption; therefore, both members of the oxygen sensitive/insensitive ratiometric dye pair would ideally be emissive in the NIR range, as differential emission across a broader range would introduce variable depth dependence of scatter as an additional experimental variable. However, the range of commercially available NIR dyes is limited, and those that are available often overlap at least partially with the emission profile of the porphyrins used in the CAOS study. While in principle substantial dye overlap can be unmixed using hyperspectral imaging approaches, the problem is compounded by the fact that all commercially available fluorophores have significantly higher quantum yields relative to the phosphor used in G3 CAOS, such that even seemingly minute regions of spectral overlap can in fact result in the phosphor's signal being completely overwhelmed and effectively obliterated by the tail end of a fluorphore's emission band. To overcome this problem, we are considering stoichoimetric integration of a fluorescent reference dye, such that the dye is only conjugated to a fraction of the total CAOS sensors present (*e.g.*, one out of twenty). However, early experiments performed within our lab indicate that such stoichiometric approaches need to be carefully controlled to ensure that the presence of a fluorescent reference dye will not affect the localization of the CAOS sensors relative to untagged molecules.

Finally, it is intriguing and often inspiring to briefly think several steps down the road regarding potential end applications this work might enable. The ability to quantitatively measure oxygen in individual cells could provide the basis for a powerful *ex vivo* therapy screening platform, wherein patient tissue/cell samples derived from biopsies, smears, or fine needle aspirates are grown into 3D spheroids and their degree of hypoxia assessed. These cultures could then be exposed to a panel of cytotoxic agents such as chemotherapeutics and radiation to determine their specific sensitivity. In principle, this information could also be combined with "next generation" high-throughput whole-exome or whole-genome sequencing technologies to provide a comprehensive susceptibility panel for each patient, as well as the means to experimentally validate any results generated through this approach. [104–106] Beyond providing patient caregivers with potentially life-extending information, this information could be pooled to generate a database of both genotype/susceptibility phenotype correlates. Additionally, physiological findings such as hypoxia could then be associated with a particular genotype, enabling a more detailed molecular inquiry as to the genetic underpinnings of hypoxia in tumors.

Another potential end application involves incorporation of oxygen-sensing materials into medical materials such as bandages, enabling measurements of important physiological parameters such as dermal oxygenation. This is an area of active investigation in our lab and will be discussed in Chapter 3.

Note: Aspects of the work described above have been published in Angewandte Chemie, International Edition. [107]

2.5 MATERIALS AND METHODS

2.5.1 GENERAL INFORMATION

Unless otherwise stated, all chemical compounds and solvents were purchased from Sigma or Fisher Scientific and used without further purification. 3-(triethylsilyl)prop-2-yn-1-amine (TES-propargylamine) and 3-(triisopropylsilyl)prop-2-yn-1-amine (TIPS-propargylamine, **1a**) were synthesized as previously reported. [85] Thin Layer Chromatography (TLC) was performed on 20x20 cm, glass-supported silica gel plates with fluorescent indicator (Sigma). The plates were visualized either under UV light or by staining with a potassium permanganate solution in water. Column Chromatography was performed on silica gel 60 (Alfa Aesar). NMR spectra were collected on a Bruker 300 MHz Ultrashield magnet using Topspin software and referenced as previously described; [108] MALDI-TOF mass spectra were acquired on a Bruker Microflex MALDI-TOF mass spectrometer using α-cyano-4-hydroxycinnamic acid as matrix, unless otherwise indicated. UV-Vis spectra of porphyrins and porphyrin products were acquired using either a Varian Cary 100 or a Nanodrop ND-1000; emission spectra were acquired using a Horiba FluoroMax fluorimeter, exciting at 632nm. For optimization of the analysis of higher generation PAMAM-like dendrons as well as the G3 CAOS sensor with MALDI-TOF MS, protocols that exist in the National Institute of Standards and Technology (NIST) database for analyzing poly(amidoamine) dendrimers were followed for sample preparations, using 7-hydroxycoumarin as matrix (http://polymers.msel.nist.gov/maldirecipes/ and [109]). All NMR and MALDI-TOF spectra are displayed in Section B.

Chemical Abbreviations used in the following sections: MeOH: methanol; EtOAc: ethyl acetate; DMF: N,N-Dimethylformamide; DCC: N,N'-Dicyclohexylcarbodiimide;

HOBt: 1-Hydroxybenzotriazole; THF: tetrahydrofuran; DCM: dichloromethane; NaOH: sodium hydroxide; HCl: hydrochloric acid; Na_2SO_4: sodium sulfate; H_2O: water; $CuSO_4$: copper sulfate.

2.5.2 Dendron subunit syntheses

Synthesis of dendron subunits proceeded according to scheme described in Figure 2.5.1.

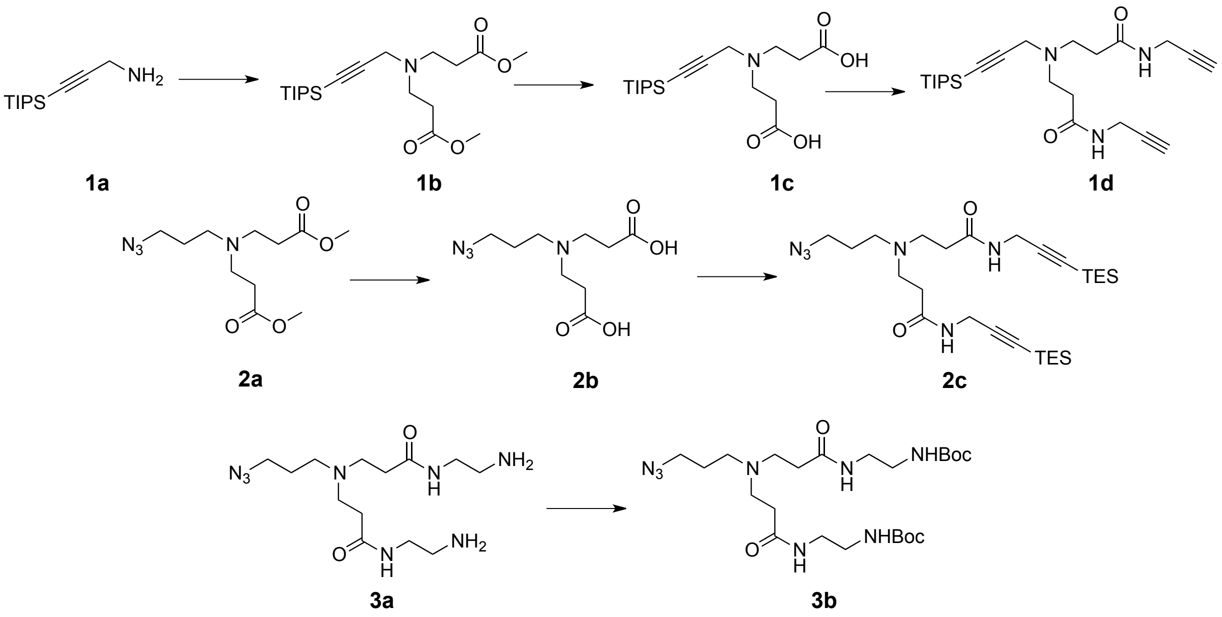

Figure 2.5.1: Synthetic scheme for CAOS dendron subunits.

Synthesis of TIPS-alkyne subunit **1d**

1a: **1a** was synthesized as previously reported. [85]

1b: A magnetically stirred solution of methyl acrylate (3.26 g, 4 eq.) in 6 ml MeOH was cooled with an ice bath, and a solution of **1a** (2 g, 1 eq) was added dropwise over a period of 1 h. The resulting solution was allowed to warm to room temperature and stirred for 48 hours. The volatiles were removed by rotary evaporation, and the residual methyl acrylate was further removed using a 1:1 azeotropic mixture with MeOH. The product was easily purified by column chromatography using a 1:1 hexanes/EtOAc solvent system. The solvent was removed by rotary evaporation to yield

3.5 g of pure product as a flaky powder (96% yield). The product was characterized by NMR and MALDI-TOF MS. ^{1}H NMR ($CDCl_3$): δ 3.66 (s, 6H), 3.46 (s, 2H), 2.84 (t, 4H, J=7.2Hz), 2.46 (t, 4H, J=7.2 Hz), 1.06 (s, 3H), 1.05 (s, 18H); MALDI-TOF MS: *m/z* 384.33 (M+H)+, calc. 383.60.

1c: In a 50 ml round bottom flask, 500 mg **1b** were dissolved in 500 μl MeOH, 500 μl H_2O, and 4.5 ml THF. 1.5 g NaOH were added and the solution was stirred for 2 hours. The solution was acidified (pH = 2) by addition of 1M HCl, and the organic component was removed by rotary evaporation. The remaining aqueous slurry was diluted with a small volume of H_2O, transferred to a 30 mL separatory funnel, and extracted 5 times with *n*-butanol. The butanol fractions were combined, dried over Na_2SO_4, and the butanol removed by rotary evaporation. Residual butanol was removed by azeotropic rotary evaporation with hexanes and the flask dried overnight, yielding **1c** as a pure, flaky powder in quantitative yield. The product was confirmed by NMR. ^{1}H NMR (methanol-d4): δ 4.33 (s, 2H), 3.59 (t, 4H, J=6.9Hz), 2.93 (t, 4H, J=6.9 Hz), 1.13 (br.s, 21H).

1d: To a solution of 51 mg **1c** (1 eq.) in DMF were added 88.79 mg DCC (3 eq.), 69.78 mg HOBt (3 eq. of 20% hydrate), and 23.7 mg propargylamine (3 eq). The reaction was stirred overnight at room temperature. Reaction completion was monitored using TLC (3:1 THF:DCM) and via MALDI-TOF MS. The solvent was removed via rotary evaporation. The product was purified on a silica column using 3:1 THF:DCM to give **1d** as flaky white powder in 76% yield. Purity was confirmed by NMR and MALDI-TOF MS. ^{1}H NMR ($CDCl_3$): δ 6.96 (t, 2H, J=4.5Hz), 4.06-4.07 (m, 4H), 3.49 (s, 2H), 2.86 (t, 4H, J=6Hz), 2.38 (t, 4H, J=6 Hz), 2.22 (t, 2H, J=2.7 Hz), 1.06 (s, 3H), 1.05 (s, 18H); MALDI-TOF MS: *m/z* 430.45 (M+H)+, 452.46 (M+Na)+, calc. 429.67.

2.5.3 SYNTHESIS OF AZIDO-TES SUBUNIT **2C**

2a: 2a was synthesized as previously reported. [110]

2b: 2b was synthesized identically to **1c** as described above, yielding **2b** as a thick oil in quantitative yield. The product was confirmed by NMR. ^{1}H NMR (methanol-d4): δ 3.35 (t, 2H, J=6.6Hz), 3.21 (t, 4H, J=6.6 Hz), 3.11 (t, 2H, J=7.8Hz), 2.50 (t, 4H, J=6.6Hz), 1.92-1.83 (m, 2H).

2c: To a solution of 40 mg **2b** (1 eq., 0.143 mmol, MW = 280) in DMF was added 101 mg DCC (3.4 eq.), 89 mg HOBt (20% hydrate, 3.4 eq.), and 83 mg of TES-propargylamine (3.4 eq.) The reaction was stirred overnight at room temperature. The following day, product formation was confirmed via TLC (3:1 THF:DCM) and MALDI-TOF MS. The product was purified using column chromatography in a 3:1 THF:DCM system, and the solvent was removed via rotary evaporation. The product was characterized by MALDI-TOF MS and NMR. The product was isolated as a waxy solid in 75% yield. ^{1}H NMR ($CDCl_3$): δ 6.68 (t, 2H, J=4.2Hz), 4.08 (d, 4H, J=5.1Hz), 3.27 (t, 2H, J=6Hz), 2.67 (t, 4H, J=6 Hz), 2.45 (t, 2H, J=6.6Hz), 2.31 (t, 4H, J=6Hz), 1.73-1.65 (m, 2H), 0.98 (t, 18H, J=7.8Hz), 0.59 (q, 12H, J=7.8Hz); MALDI-TOF MS: *m/z* 547.54 (M+H)+, calc. 546.90.

SYNTHESIS OF AZIDO-NBOC SUBUNIT **3B**

3a: **3a** was synthesized as previously reported [111].

3b: 10 mg of **3a** were dissolved in 200 μl methanol, to which 16 mg di-*tert*-butyl bicarbonate were slowly added. The reaction was sealed and allowed to stir overnight. After confirming product formation via MALDI-TOF MS, the solvent was removed and the filmy plaque redissolved in a 50:50 THF/EtOAc mixture and extracted 3x with brine. The organic layer was dried dried over

Na_2SO_4, filtered, and dried again overnight under vacuum, yielding the product as a waxy plaque in 96% yield. The product was confirmed by NMR and MALDI-TOF MS. ^{1}H NMR ($CDCl_3$): δ 7.24 (br.s, 2H), 5.44 (br.s, 2H), 3.30-3.18 (m, 10H), 2.64 (t, 4H, J=6Hz), 2.43 (t, 2H, J=6.6 Hz), 2.30 (t, 4H, J=5.7Hz), 1.70-1.61 (m, 2H), 1.39 (s, 18H); MALDI-TOF MS: *m/z* 529.63 (M+H)+, calc. 528.65.

2.5.4 G2 Dendron Synthesis

Synthesis of the G2 dendron proceeded according to the scheme described in Figure 2.5.2.

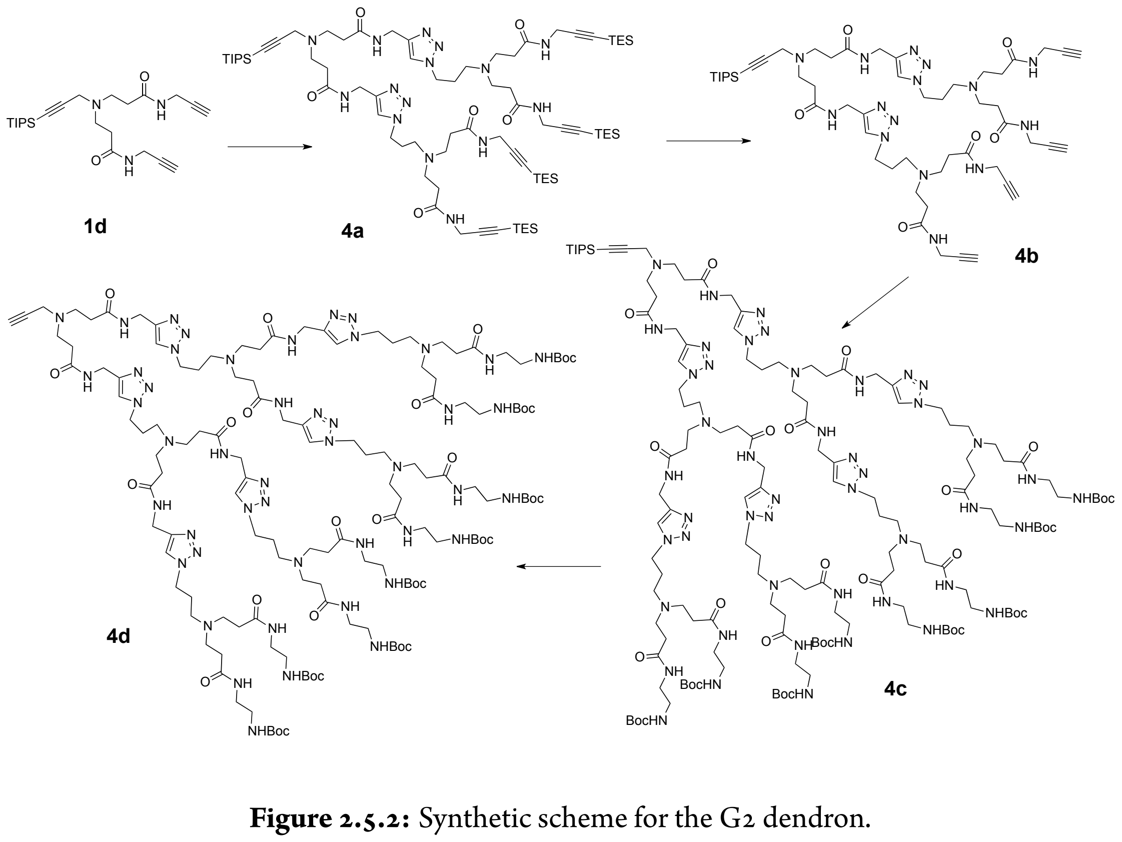

Figure 2.5.2: Synthetic scheme for the G2 dendron.

4a: 25 mg **1d** (1 eq.) and 63.7 mg **2c** (2 eq.) were dissolved in 500 μl DMF. 1.86 $CuSO_4$ in 20 μl H_2O (0.2 eq.) and 4.61 mg sodium ascorbate in 30 μl H_2O (0.4 eq.) were added sequentially, and the solution was allowed to stir overnight at room temperature. Product formation was confirmed by MALDI-TOF MS. The solvent was removed via rotary evaporation and the product was dissolved in 10 ml diethyl ether. The product was washed three times with water (1 ml) and once with brine (2 ml), dried for 15 minutes over Na_2SO_4, and the solvent was removed via rotary evaporation; excess solvent was removed overnight under high vacuum to yield 86 mg of product (97% yield). ^{1}H NMR ($CDCl_3$): δ 9.17 (t, 2H, J=5.7 Hz), 7.73 (t, 4H, J=5.1 Hz), 7.61 (s, 2H), 4.49 (d, 4H, J=5.7), 4.28 (br.s, 4H), 4.17 (d, 8H, J=5.1Hz), 3.30 (s, 2H), 2.67-2.57 (m, 12H), 2.27 (m, 12H), 2.04 (m, 8H), 1.01-1.00 (m, 21H), 0.94 (t, 36H, J=7.8H), 0.54 (q, 24H, J=7.8H); MALDI-TOF MS: *m/z* 1524.93 (M+H)+, 1546.98 (M+Na)+, calc. 1523.46.

4b: Removal of the triethylsilyl protecting groups from **4a** was carried out using a modified version of a previously described protocol [85]. To a solution of 79.3 mg **4a** in 5 ml MeOH was added 360 mg K_2CO_3 (50 eq.); the reaction was allowed to stir for 36 hours. MeOH was removed via rotary evaporation to form a dense salty slurry, and the remaining powder was dried using argon flow. The thick powder product was dissolved in a 1:1 EtOAc:THF solution and washed 3x using brine. The product was dried over Na_2SO_4 and the solvent was removed via rotary evaporation. The product was then redissolved in DCM and extracted a second time using H_2O, dried over Na_2SO_4, and the solvent removed via rotary evaporation. Reaction completeness was verified by MALDI-TOF MS and the product characterized by NMR. Notably, NMR showed the presence of trace residual triethylsilyl chloride; because this salt would not interfere with the remaining conjugation reactions, the solution was deemed sufficiently pure. Overall reaction yield was determined by integration of the relative product peaks and determined to be 87%. Any residual triethylsilyl chloride was removed in the purification steps that followed additional reactions. ^{1}H NMR ($CDCl_3$): δ 9.29 (br.s, 2H), 7.92 (t, 4H, J=5.1 Hz), 7.66 (s, 2H), 4.50 (d, 4H, J=5.7), 4.33 (br.s, 4H), 4.13-4.11 (m, 8H), 3.32 (s, 2H), 2.72-2.63 (m, 12H), 2.33-2.32 (m, 12H), 2.09 (m, 8H), 1.03-1.02 (m, 21H); MALDI-TOF MS: *m/z* 1067.49 (M+H)+, 1089.48 (M+Na)+, calc.

1066.42.

4c: 10 mg **4b** (1 eq.) were dissolved in 200 μl DMF, to which 19.8 mg **3b** (4 eq.) were added. 0.3 mg $CuSO_4$ in H_2O (38.4 mg/ml, 0.2 equivalents) and 0.74 mg sodium ascorbate in H_2O (63.5 mg/ml, 0.4 equivalents) were added sequentially, and the mixture was allowed to stir overnight at room temperature. The solvent was removed via argon flow-assisted evaporation, and the product was dissolved in 2:1 EtOAc:THF. The product was extracted three times with H_2O and dried over Na_2SO_4, the solvent was removed via rotary evaporation, and the product was dried overnight under vacuum to give **4c** as a waxy product in 87% yield (26 mg). Product purity was confirmed via NMR. ^{1}H NMR (methanol-d4): δ 7.98 (m, 6H), 4.56-4.24 (m, 24H), 3.26 (m, 16H), 3.15 (m, 16H), 2.82-2.63 (m, 24H), 2.42-2.29 (m, 40H), 2.09-1.94 (m, 12H), 1.42 (s, 72H), 1.09-1.08 (m, 21H); MALDI-TOF MS: *m/z* 3204.83 (M+Na)+, calc. 3181.00.

4d: To a solution of 26 mg of **4c** in 100 μl THF were added approximately 5 equivalents of "anhydrous" tetrabutylammonium fluoride (TBAF). The solution was allowed to stir overnight at room temperature. THF was removed by evaporation and the product was redissolved in MeOH. A modified version of a previously published protocol was used to facilitate straightforward TBAF removal.[112] An excess of calcium carbonate and DOWEX 50WX8-40 was added to the reaction solution, and the resulting slurry was allowed to stir for 1-2 hours. The product was filtered through Celite and dried over Na_2SO_4. The solvent was removed via rotary evaporation and the product was dried overnight under vacuum to give 26.16 mg of a waxy product (94% yield). Notably, the triisopropylsilyl fluoride salt that results from the deprotection is not removed by the reaction with the DOWEX resin and remains in the product; however, as above, it does not interfere with any future reaction steps so no further purification was attempted. If desired, it can be removed by washing the product with ether to obtain pure product. ^{1}H NMR (methanol-d4): δ 4.72-4.54 (m, 12H), 3.57-3.49 (m, 32H), 3.27-3.18 (m, 38H), 2.86-2.78 (m, 16H), 2.60-2.47 (m, 12H), 1.43 (s, 72H); MALDI-TOF MS (using 7-hydroxycoumarin as matrix): *m/z* 3027.02 (M+H)+, 3049.24 (M+Na)+, calc. 3024.66.[9]

2.5.5 Synthesis of Pd-tetraazidotetrabenzoporphyrin

Pd-Tetraazidotetrabenzoporphyrin was synthesized according to the scheme outlined in Figure 2.5.3.

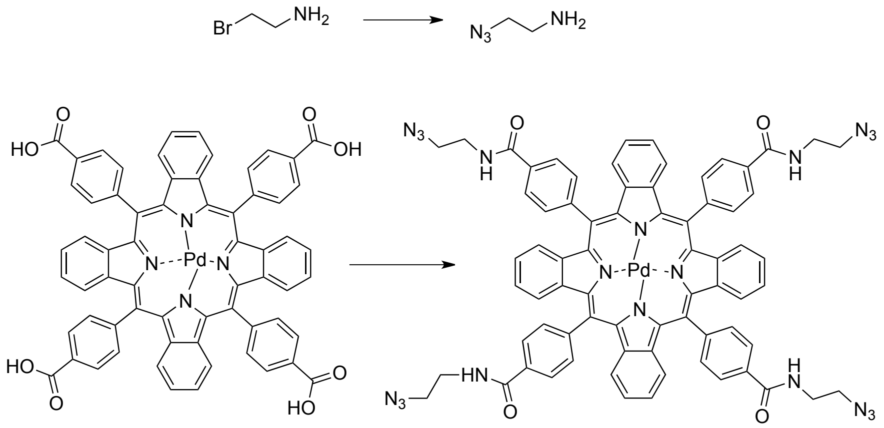

5a **5b**

Figure 2.5.3: Synthetic scheme for the tetraazidotetrabenzoporphyrin **5b**.

2-azidoethylamine: 5 g 2-bromoethylamine hydrobromide (1 eq.) were dissolved in 28 ml water, to which 8.9 g sodium azide (3.36 eq) in 42 ml H_2O were slowly added. The solution was stirred under reflux overnight and allowed to cool the following morning. Approximately 2/3 of the water was removed via evaporation, and the remaining volume was diluted with 140 ml diethyl ether. The solution was cooled to 0 °C and 11.1 g potassium hydroxide pellets (1.75 equivalents) were added to promote phase separation. The organic phase was collected and the remaining aqueous layer was extracted three times with 84 ml diethyl ether. The organics were combined, dried over

---

[9] Empirical evidence suggests that yields from this step are optimal if Alan Jackson's "Chasin' that Neon Rainbow" is playing in the background during the workup.

Na_2SO_4, and concentrated by rotary evaporation to afford 2.72 g of the product as a pure yellow oil (78% yield). ^{1}H NMR ($CDCl_3$): δ 3.31 (t, J=5.7 Hz, 2H), 2.82 (t, J=5.7 Hz, 2H), 1.40 (br.s, 2H).

5a: **5a** was synthesized as previously described [63, 64].

5b: O-(Benzotriazol-1-yl)-N,N,N′,N′-tetramethyluronium hexafluorophosphate (HBTU; 14 mg, 7.8 eq.) was added to a magnetically stirred solution of Pd-tetracarboxytetrabenzo porphyrin (**5a**, 5 mg, 1 eq.) in N,N-Dimethylformamide (0.5 mL), and the mixture was stirred for 5 min at r.t.. N,N-Diisopropylethylamine (12 mg, 19.6 eq.) was added, followed immediately by 2-azidoethylamine (3 mg, 7.8 eq.), and the resulting solution was stirred overnight at r.t. After dichloromethane was added to the reaction mixture, it was extracted with water, and the organic phase was collected, dried over magnesium sulfate, and the solvent was removed by rotary evaporation. The resulting residue was purified by column chromatography (20:1 to 4:1 DCM:MeOH), to afford the product (4 mg, 64% yield) as a green solid. MALDI-TOF MS: *m/z* 1366.65 (M)+, calc. 1366.35.

2.5.6 G3 CAOS NANOCONJUGATE SYNTHESIS

G3 CAOS synthesis was performed according to the scheme described in Figure 2.5.4.

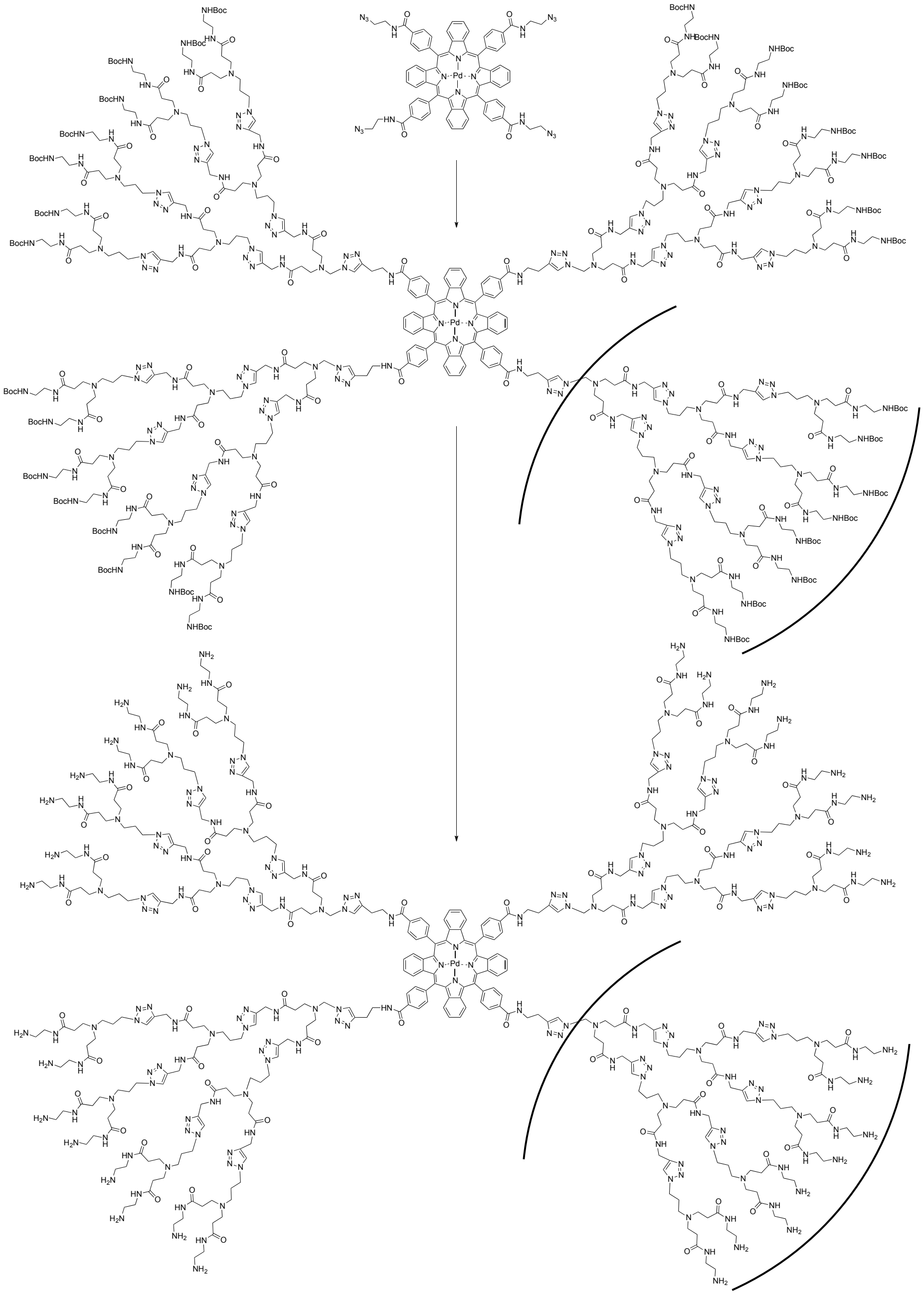

5b

6a

6b

Figure 2.5.4: The scheme used to synthesize the G3 CAOS nanoconjugate, **6b**. Note that the presence of the tetra-adduct CAOS nanoconjugate was not confirmed, as indicated by the brackets in the chemical structures.

6a: 565 μg **7b** were dissolved in 200 μl freshly distilled DMF, to which were added 6 mg **4d** (5 eq). Air was purged from the vessel and the solution was placed under argon. 789 μg $CuSO_4$ (12 eq.) in 8 μl H_2O and 1.96 μg (24 eq.) sodium ascorbate in 10 μl H_2O were added sequentially under argon, and the mixture was allowed to stir under argon at room temperature for 48 hours. The disappearance of unreacted porphyrin was monitored by MALDI-TOF MS. The solvent was removed by argon-assisted evaporation and the product was dissolved again in MeOH and dried again to remove any residual DMF.

6b: To cleave the protecting groups on the dendrimer's primary amine groups and yield **6b**, the product was dissolved in a large excess of neat trifluoroacetic acid and stirred overnight. The product was dried under argon flow, washed with dichloromethane to remove residual trifluoroacetic acid, and dissolved in acidified water. The product was purified overnight via dialysis in H_2O to remove salts and unreacted, low-molecular weight dendrons. The product was lyophilized and weighed to afford 1.6 g of a green fluffy product (2-step 34% yield). ^1H NMR (methanol-d4, water suppression pulse sequence): δ 8.22-7.95 (m, 24H), 3.7.82-7.54 (m, 38H), 7.14-7.08 (m, 16H), 6.51 (m, 10H), 4.34-4.00 (m, 68H), 3.55-3.36 (m, 48H), 3.12-3.03 (m, 122H), 2.72-2.55 (m, 130H), 2.33-2.16 (m, 154H), 1.93-1.72 (m, 64H). MALDI-TOF MS data are discussed below.

Characterization of 6b: *NMR Analysis*: Comparison of the integration of the peaks centered at approximately 7.1 ppm and 4.2 ppm, which correspond to the aromatic protons on **5b** (integration of 16) and the methylene protons adjacent to either side of the triazole rings on **4d** (theoretical integration of 112; observed integration of 68), respectively, indicates an average of between two to three dendrons per nanoconjugate (Figures B.21 and B.22). *MALDI-TOF MS Analysis*: As indicated in the main body text, MALDI-TOF MS analysis using 7-hydroxycoumarin as matrix revealed the presence of the mono-, di-, and tri-dendron adducts, as indicated by the presence of broad bell-shaped peaks at the appropriate mass regions (Figure B.23); however, the peak intensities observed via MALDI-TOF MS are not quantifiable and can therefore offer no insight into the relative quantities of each adduct. In figure B.23, the inset shows the specific peaks corresponding to the di- and tri-adduct; these spectra were acquired by changing the acquisition parameters to suppress lower molecular weight peaks, thereby changing the effective dynamic range of the detector and optimizing it for a particular mass ion region.

2.5.7 Dye/CAOS-PAMAM Conjugation Protocols

2.32 μl of a 1 mg/ml AlexaFluor-488 NHS stock solution (1.2 equivalents) in dimethyl sulfoxide were added to 10 μl of a 300 μM G3 CAOS stock solution (1 equivalent) in H_2O at the bottom of an Eppendorf tube. The tube was placed in a rack on a rotary stirrer and stirred for 2 hours in the dark at room temperature. After 2 hours, the product was dissolved in 100 μl H_2O, dialyzed overnight against water using a 3,500 MWCO dialysis device, then lyophilized. An analogous protocol was used to conjugate AlexaFluor-488 NHS to G4 PAMAM. The product was verified by UV-Vis spectrophotometry.

2.5.8 Time-resolved phosphorescence measurements and microscopy

Phosphorescence lifetime measurements

Phosphorescence lifetime measurements require a time-gated light source, the pulse width of which is ideally smaller than the lifetime range of the phosphor. To create an economical 632 nm "pulsed" laser source, we adopted an existing prototype design (Joel A. Spencer, personal communication). Briefly, a single scanning galvo operating at 200 Hz was centered on a variable width slit positioned in the focal plane of a beam-expanding telescope; each sweep of the CW laser across the slit creates an effective laser "pulse", the duration of which can be varied by adjusting the slit width and/or the scan rate (Figure 2.5.5). Using this method, pulses with temporal FWHM of approximately 15 μs were achieved. The output light was incident upon a NIR, air-spaced doublet lens with a 30 mm working distance (ThorLabs ACA254-030-B), which focused it into a temperature- and atmosphere-controlled, stirred UV-fused silica cuvette (T = 23 °C). Generated phosphorescence was propagated back through the system to a dichroic mirror (640nm long-pass), which redirected the light to a Hamamatsu H7422PA-50 PMT. One lifetime trace was recorded per pass of the laser across the slit over a period of 1000 μs; 500 traces were averaged to create a single curve. Temperature control was provided through the use of a ThorLabs TH10K thermistor, HT15W heater, and a TC200 heater controller. Oxygen measurements were collected using a freshly calibrated Unisense OX-N microsensor and an OXY-Meter picoammeter. The entire phosphorimeter assembly was controlled by a custom-made LabView program (available upon request), which made automated measurements every one to five minutes; an automated shutter protected the cuvette from excess beam exposure in between measurements.

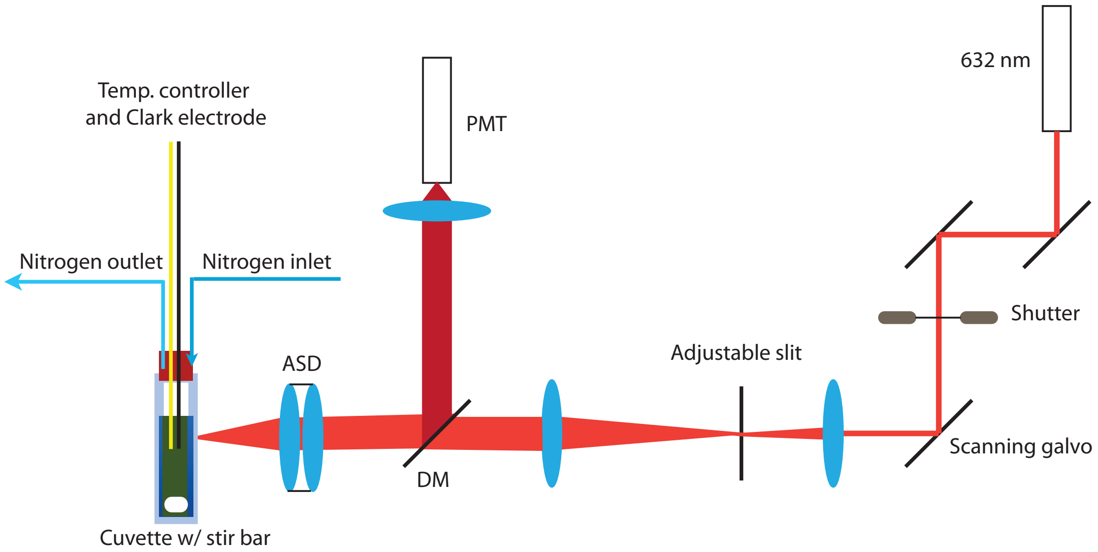

Figure 2.5.5: The phosphorimeter used for the calibration of G3 CAOS. DM = dichroic mirror; ASD = air-spaced doublet lens; PMT = photomultiplier tube.

A typical experiment was conducted as follows: after transferring the CAOS/BSA solution to the cuvette, installing the required sensors, the system was purged with room air and allowed to equilibrate. Once the OX-N recorded a level baseline, the system was turned on and lifetime traces were recorded as described above. The room air flow was turned off and replaced with nitrogen flow. Traces were collected until the OXY-N probe read a value close or equal to the calibrated "zero oxygen" value, indicating all oxygen had been purged from solution. The lifetime curve acquisition rate was varied from one minute to five minutes over the course of the experiment. Upon reaching "zero oxygen" or attainment of a steady, time-invariant reading at close to zero mmHg, pO_2, the nitrogen flow was turned off, the air flow was turned back on, and a calibration curve was collected in the opposite direction.

Data processing and excitation pulse deconvolution were performed using a custom-made MatLab script (available upon request).

2.5.9 CELL CULTURE AND 3D *IN VITRO* TUMOR MODEL

OVCAR5 monolayer cells and *in vitro* spheroids were grown and maintained as previously described. [41]. Spheroids were imaged at day 10 of growth and all monolayer cells were used within 24 hours of plating, unless otherwise described.

CONFOCAL AND TWO-PHOTON FLUORESCENCE MICROSCOPY

Confocal fluorescence imaging of AlexaFluor 488 was performed on an Olympus FV1000 inverted confocal microscope using the 488 nm line of an argon ion laser and the manufacturer's recommended filter settings. Two-photon imaging experiments were performed using an integrated MaiTai DeepSee tunable Ti:Sapphire laser, tuned to 750 nm. Z-stacks were acquired at intervals of 1.5 μm/slice.

2.5.10 MONOLAYER UPTAKE EXPERIMENTS

OVCAR5 cells were plated as previously described. [41] Approximately 12-18 hours after plating, the culture medium was removed and replaced with 1 ml of a 500 nM AlexaFluor 488-G4 PAMAM solution, prepared in serum-free media. Cells were incubated at 37 °C for 45 minutes under

5% CO_2; upon completion of the incubation period, the cultures were gently washed with PBS followed by media. Following the washes, the media was replaced and the cells were transported to the microscope for immediate imaging. AlexaFluor 488-G3 CAOS and G3 CAOS uptake experiments were performed in an analogous fashion using the concentrations indicated in the manuscript.

2.5.11 Spheroid imaging experiments

OvCa 3D spheroids were grown for ten days as previously described. [41] On day 10, the culture medium was removed and replaced with 1 ml of a 500 nM solution of AlexaFluor 488-G4 PAMAM in serum-free media. Controls were incubated with serum-free media. The culture was incubated for either 3.5h (AlexaFluor-PAMAM) or 4h (G3 CAOS) at 37 °C in a 5% CO_2 incubator. Upon completion of the incubation period, the cultures were gently washed with PBS followed by media. Following the washes, the media was replaced and the cells were transported to the microscope for immediate imaging. Treatment with Oxyphor G2 and G3 CAOS were performed in an analogous fashion using the concentrations and incubation times indicated.

2.5.12 Confocal phosphorescence microscopy

Cellular and spheroid phosphorescence imaging was performed using a custom-made, single-photon counting, NIR-optimized confocal microscope (Figure 2.5.6). Briefly, a 632 nm CW laser was passed through a beam-expanding telescope and indecent upon a 640 nm long-pass dichroic mirror, where it was passed into an XY scan head. The scanhead consists of two galvanometric mirrors (Cambridge Technologies) separated by an optical relay providing in total threefold beam magnification.[113] The light is directed into a modified Axiovert 200, where it was relayed to the microscope objective; this microscope also contained the optics necessary for *trans* illumination and visualization using a built-in eyepiece. During imaging, samples were maintained in an atmosphere- and temperature controlled chamber (DH35i, Warner Instruments), which was set to 37 °C and maintained under either 5% CO_2 or nitrogen, as appropriate. Cells imaged under nitrogen were first purged for 45-60 minutes to drive dissolved oxygen from the culture medium. Phosphorescence images were collected using either a Zeiss IR-Achroplan water objective (40x, 0.8 NA) for 3D OvCa spheroids or an Olympus UPLSAPO water objective (60x, 1.20 NA) for monolayer cells. Generated phosphorescence was relayed back down the optical path to the dichroic mirror, after which it passed through a 100 μm optical pinhole and recollimated using two 50 mm lenses. The light was focused onto an H7422PA-50 PMT, the output of which was connected to a C9744 photon counting unit. Images were acquired with a pixel dwell time of 10 μs and an average power of approximately 50 μW. Z-stacks were acquired using a PIFOC piezo flexure objective scanner at intervals of 10 μm/slice.

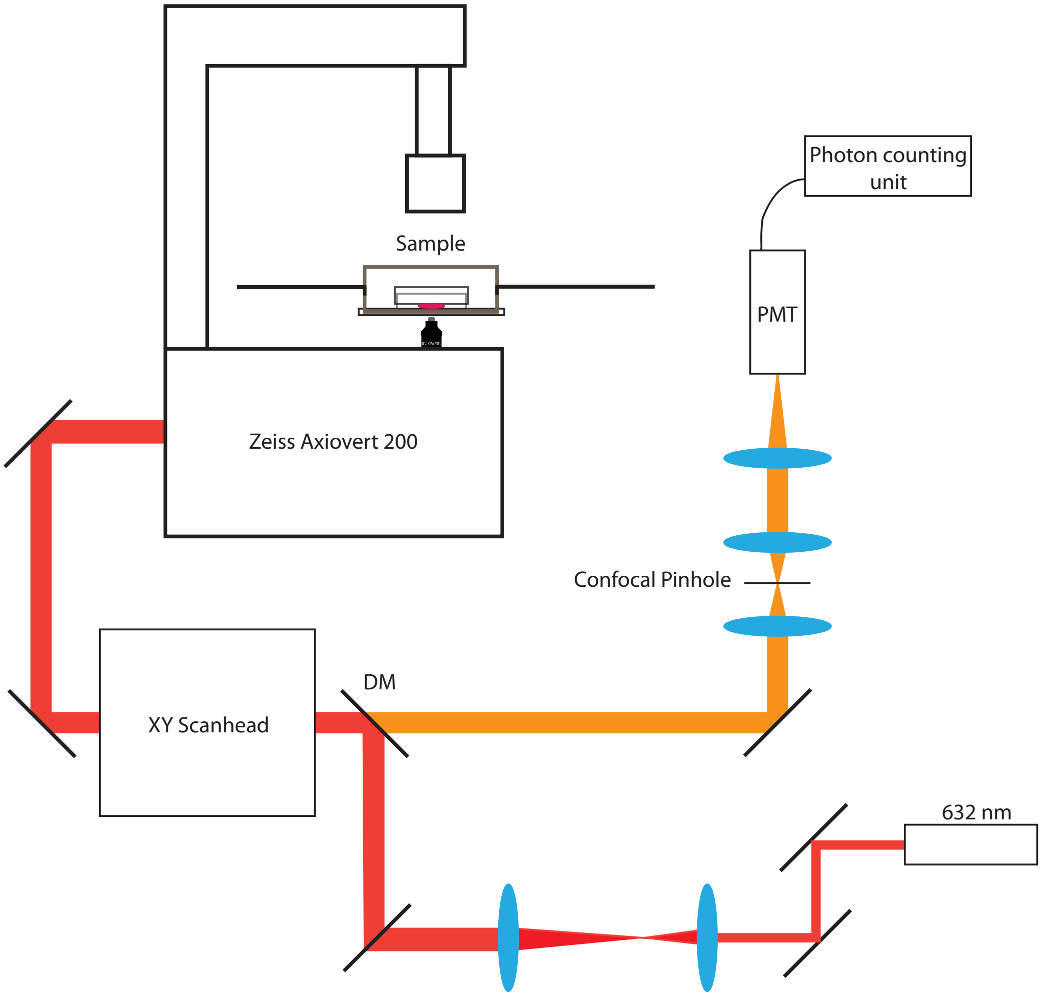

Figure 2.5.6: The confocal phosphorescence microscope. DM = dichroic mirror; PMT = photomultiplier tube.

2.5.13 OvCa viability studies

OVCAR5 cells (P13) were trypsinized as reported previously and seeded as a single-cell suspension in a clear plastic 48-well plate (BD Falcon) and incubated at 37 °C for 24 hours in a 5% CO_2 incubator prior to the experiment. Cells were seeded using 500 *ul* of a 100,000 cell/ml suspension, with N=4 wells for experimental conditions and N=8 for control conditions. Under subdued light, working treatment solutions at the appropriate concentrations were made for G3 CAOS in complete cell culture media (CellGro) supplemented with 10% HI-FBS (GIBCO) and 1% penicillin/streptomycin mixture. The culture medium was carefully aspirated from individual culture wells, and the wells were dosed with 200 μl of the appropriate G3 CAOS stock solution. NT controls were treated with culture media. Cells were incubated at 37 °C in a 5% CO_2 incubator for 45 minutes, following which the treatment media was aspirated and the wells were washed with culture medium to remove residual compound. Fresh media was replaced, and the cells were returned to the 5% incubator for 24 hours at 37 °C.

24 hours after the above treatment, cellular viability was evaluated using an MTT viability assay. Briefly, a 1 mg/ml solution of MTT reagent (thiazolyl blue tetrazolium bromide; Sigma) was prepared in warmed complete media; the media from all culture wells was removed and replaced with the freshly prepared MTT reagent mixture (400 μl/well). Cells were incubated at 37 °C for 1 hour in a 5% CO_2 incubator. After 1 hour, the MTT reagent-containing media solution was carefully aspirated to ensure the complete removal of residual extracellular reagent. Cellular formazan resulting from the hydrolysis of the MTT reagent by cellular mitochondrial enzymes was then extracted by the addition of DMSO to sample wells (400 μl per well). Samples were incubated for a period of 15 minutes at room temperature under subdued light and plates were rocked and swirled periodically, to allow for complete and uniform solvation of formazan into DMSO. The formazan-containing DMSO was then aliquoted in triplicate (100 μl volumes) for each sample well into a clear plastic 96-well plate (BD Falcon) alongside twelve "blank" control wells containing an equal volume of neat DMSO to be used later for subtraction of background signal from the solvent and to compensate for any instrument noise.

The absorbance of all DMSO solutions in the 96-well plate(s) was measured at 570 nm using a SpectraMax M5 plate reader. Measured absorbance values were averaged and the standard deviation calculated. Outlier analysis was performed and outlier values were removed, with outliers defined as greater than +/- two standard deviations from the mean. The individual absorbance values from the data set (with outliers removed) were normalized to the average of absorbance values from untreated control samples to yield the normalized absorbance/viability for each value. These normalized values were then entered into JMP statistical analysis to generate a data plot and determine statistical significance using the pairwise student's t-test.

3

Non-invasive transdermal two-dimensional mapping of cutaneous oxygenation

3.1 INTRODUCTION

Oxygen is essential for maintaining the viability of skin and its contents. [114] The ability to measure cutaneous oxygen status non-invasively is needed for the treatment of a variety of skin diseases including chronic and ischemic wounds, burns, and large complex wounds that require skin replacement. Measuring tissue oxygen tension helps diagnose, prevent and monitor the therapeutic response of ischemic conditions. It also allows for the monitoring of surgical flap/graft perfusion and aids in the early detection of flap/graft failure. Additionally, measuring the dynamic changes in pO_2 on the skin surface can provide information on the oxygen consumption properties of the underlying tissue, which can in turn help identify tissue that is metabolically deviated from normal.

Chronic wounds, largely resulting from ischemia, account for twenty percent of non-traumatic wounds, with an estimated $25 billion dollars in treatment cost per year. [115, 116] The prevalence of these wounds is linked directly to increased aging demographics, vascular disease, venous insufficiency, mechanical pressure and diabetic vasculopathy. Chronic wounds that develop due to tissue hypoxia are not only painful, but are a leading cause of prolonged hospitalization. [117] If not treated properly, infections and other complications may occur. The presence of tissue hypoxia also significantly worsens disease prognosis. [114, 115, 118, 119] Wound healing is highly oxygen-dependent due to the increased energy demand for tissue reparative processes such as cell proliferation, response to infections, and collagen synthesis; damaged tissue deprived of adequate blood flow has a decreased ability to heal. [114, 120]

The surgical treatment of burns is another example where objective measurement of cutaneous oxygenation may improve outcomes. Currently, the clinical determination of burn depth and therefore the intraoperative decision for debridement depends on subjective visual assessments, or rarely, invasive techniques such as a skin biopsy. Accurate determination of burn depth based on cutaneous oxygenation may limit the degree of surgical intervention. The ability to determine tissue viability would also allow for the monitoring of skin graft and skin substitute integration in patients who require skin replacement after burn debridement.

Many previous attempts have been made to develop technologies that allow the detection of tissue oxygenation. Histochemical staining with hypoxia markers such as pimonidazole provides semi-quantitative detection of tissue hypoxia, and radioactively labeled markers have been developed that can be imaged by position emission tomography (PET). [121–123] However, this method requires the injection of exogenous markers and either tissue biopsy or use of specialized instrumentation to identify these markers; this method is therefore labor-intensive and also may be limited by the spatial resolution of PET scanners. The needle-type Clark electrodes, as discussed in Section 2.3.1, can precisely measure pO_2 and are the gold standard for assessment of tissue oxygenation. [114] However, placing a needle electrode into tissue 1) is necessarily restricted to point measurements, 2) is invasive and can be painful, and 3) causes tissue injury that can alter microcirculation and thus the pO2 levels being measured. [124] Although planar electrodes have been designed that allow the measurement of transcutaneous oxygen pressure ($TcpO_2$) by attaching probes on the skin surface, these tools require heating the examined skin to 44-45 °C, beyond the average physiological temperature. Furthermore, $TcpO_2$ devices only allow point measurements, making multiple measurements necessary for the assessment of the entire area under examination. [125, 126]

Other non-invasive methods, such as pulse oximetry, estimate tissue oxygenation by calculating the ratio between oxygenated and deoxygenated hemoglobin using its oxygen-dependent spectral properties. [127] However, the results of this indirect approach do not necessarily represent absolute tissue oxygenation, since 1) they only provide the relative amount of oxy/deoxy hemoglobin (oxygen saturation) but not total oxygen supply, and 2) they provide no information about oxygen consumption rate. For example, an inflammatory area with normal oxygen saturation as measured in the blood vessels can still be hypoxic due to rapid oxygen consumption by the highly metabolic cells surrounding the blood vessel. Due to these crucial limitations, few studies exist on tissue oxygenation in acute wounds and fewer still on tissue oxygenation in chronic wounds. [114] These and other factors have created a long-standing need for a technology that allows rapid and non-invasive tissue oxygenation quantification across a wound site without cumbersome tools, and one that can be read easily and without extensive training.

As discussed in Chapter 2, a sensitive approach to quantify tissue oxygenation utilizes a process known as oxygen-dependent quenching of phosphorescence. [43] Recall that phosphorescence of a molecular sensor can be quenched by collision with oxygen resulting in energy transfer from the excited triplet state of the phosphor to ground-state triplet oxygen molecules. As a result, the sensor's phosphorescence lifetime decreases and is inversely proportional to the concentration of oxygen present in the molecule's surroundings (Eq. 2.6). Among the existing oxygen-sensing phosphors, metalloporphyrins have attracted much attention due to their unique photophysical properties, such as multiple excitation bands and relatively long-lived, room temperature phosphorescence in the red and near-infrared spectral region. Metalloporphyrin-based molecular sensors have been used to measure vascular oxygen tension in organs such as kidney, heart and brain in various animal models. [63, 128–134] Creating a layer of film containing such phosphors for the monitoring of tissue oxygenation status has the potential to provide a continuous, quantitative two-dimensional map of pO_2 in real time as opposed to the single point measurement obtained by the $TcPO_2$ device, therefore allowing for a more rapid and comprehensive assessment of tissue perfusion. Such an approach would not, in principle, require any patient-specific calibration and could be carried out repeatedly under physiological conditions. Pioneering work in the development of such sensing films has been reported by Wolfbeis and his colleagues, who have demonstrated their application in visualizing wounds and infections via both lifetime measurements and measuring changes in phosphorescence intensity. [42, 135–137]

Thus, there is an unmet clinical need for the development of a breathable, transparent, simple-to-apply-and-read and easily removable bandage for mapping oxygen across skin, burns and grafts, that can report oxygen, protect the underlying tissue, and enable visual inspection of tissue through the bandage itself. [138] Here, we present a novel oxygen-sensing, rapid-drying paint-on bandage that can be applied to the surface of skin for two-dimensional tissue oxygenation mapping, designed for the monitoring of burns and tissue grafts. By embedding oxygen-sensing molecules within a transparent, polymeric liquid bandage material, the sensor can be painted on the surface of the skin as a viscous liquid and allowed to dry against the wound topology to form a solid tight seal. To ensure facile oxygen sensing a porphyrin-dendrimer was utilized, where a metallated porphyrin as phosphorescent core was surrounded by a dendritic structure. The dendrimer not only reduced the collisional frequency of oxygen with the porphyrin core by attenuating oxygen diffusion through its branches, but also increased the porphyrin's chemical compatibility with the liquid bandage components, allowing for homogeneous distribution of the molecule throughout the bandage setting process. This strategy enabled the bandage to reach an optimum dynamic range for oxygen sensing throughout physiological pO_2 values, and minimized porphyrin-porphyrin interactions that could lead to a decrease in porphyrin emissivity caused by self-quenching. Once the sensor was applied to the skin, a transparent barrier film was placed on top of the sensing bandage to reduce, but not eliminate, ambient oxygen exchange. The phosphorescence emission of the sensing bandage was captured by a custom camera and used to generate a two-dimensional oxygen map of the underlying tissue, via either a ratiometric or a lifetime-based approach. To enable highly sensitive measurements of skin oxygenation, a delay-trigger mechanism was designed to suppress tissue autofluorescence. Moreover, by temporally integrating the oxygen consumption beneath the bandage, tissue viability could be inferred. After use, the bandage was easily removed without disrupting the underlying tissue. This bandage system was first validated using an *in vivo* rat model to sense tissue ischemia. It was then tested on porcine burn models *ex vivo* and *in vivo* to monitor burn progression. Lastly, it was applied to an *in vivo* porcine graft model to visualize the integration of full-thickness and partial-thickness skin grafts.

3.2 Materials and methods

3.2.1 Oxygen-sensing paint-on bandage and camera based readout system

The oxygen sensitive phosphor and reference dye used in creating the sensing bandage were Pd-meso-tetra-(4-carboxyphenyl)porphyrin-dendrimer (Oxyphor R2) (Oxygen Enterprises, Ltd., Philadelphia, PA) and Coumarin 500 (Exciton, Dayton, OH), respectively. The long-lifetime Oxyphor R2 was specifically selected so that its long-lived phosphorescence could be distinguished from tissue autofluorescence using inexpensive timing circuitry. To ensure the solubility of the porphyrin dendrimer as well as its effective mixing with the liquid bandage components in both liquid and dried form, the terminal carboxy groups of the Oxyphor R2 were reacted with ethanol to form ethyl esters. The paint-on bandage mixture was formulated by mixing ethanol solutions of the esterified Oxyphor R2 (4.2 mM) and Coumarin 500 (10 mM) with the New-Skin®liquid bandage (Prestige Brands, Tarrytown, NY) at a volumetric ratio of 2:1:10. The breathable transparent film dressing Tegaderm®(1622W, 3M, Saint Paul, MN) was used as the barrier layer covering the sensing bandage to reduce the oxygen exchange between the sensing bandage and room air (Figure 3.2.1).

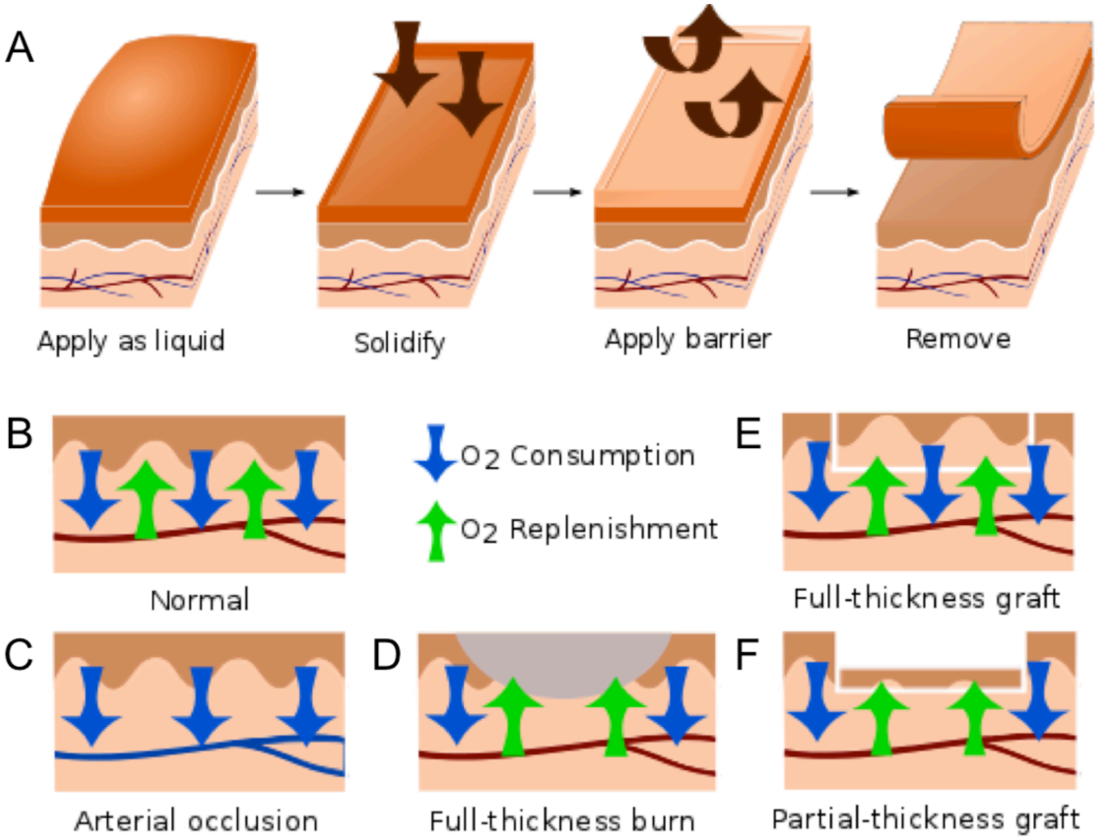

Figure 3.2.1: A: Schematic diagram showing the application of the pO_2-sensing bandage as a liquid, bandage solidification, application of the barrier layer, and bandage removal after pO_2 measurement. The supply and consumption of oxygen in tissue balance to yield a measurable tissue oxygenation. **B**: Balanced O_2 consumption and replenishment in normal skin. **C**: Decreased surface pO_2 during tissue ischemia induced by arterial ligation. **D**: Elevated surface pO_2 due to decreased O_2 consumption by necrotic tissue in a full-thickness burn. **E**: Unaffected or slightly elevated surface pO_2 in a full-thickness skin graft. **F**: Elevated surface pO_2 due to decreased O_2 consumption at a partial-thickness skin graft, which is composed of non-viable epithelial cells and only a thin layer (30/1000 inch) of dermal cells.

Two Thyristor®electronic flash units (285-HV, Vivitar, Edison, NJ) equipped with 400/70 nm bandpass filters were used to provide a brief pulse of blue excitation light for both the oxygen-sensing phosphor (λ_{ex}= 415 nm) and the reference dye (λ_{ex}= 392 nm). A NIR CMOS camera (DCC3240N, Thorlabs, Newton, NJ) equipped with a 60 mm macrolens (Nikon, Melville, NY) was used to collect the emitted light from the sensing bandage. The phosphorescence of Oxyphor

R2 (λ_{em},max= 690 nm) was captured as the "red-channel" image by placing a 700/70 nm bandpass filter at the camera lens front. The reference dye, Coumarin 500 (λ_{em},max= 495 nm), was imaged with a 510/10 nm bandpass filter and served as the "green-channel." The flash onset and the opening of the camera shutter were temporally coordinated by a digital delay/pulse generator (Stanford Research System, Sunnyvale, CA), so that images could be taken at arbitrary time points after the flash was triggered. Image analysis routines were performed in Matlab to generate the two-dimensional oxygen maps.

3.2.2 System calibration using phosphorescence intensity and lifetime

The oxygen-sensing paint-on bandage was calibrated by placing a dried sensing film inside a quartz cuvette with an oxygen partial pressure controlled by a gas mixing system. The oxygen content was adjusted step-wise from 160 mmHg to 0 mmHg, and monitored in real-time using a needle-based Clark electrode (Unisense, Aarhus, Denmark). The system was allowed to stabilize at each step for 5 min before images were taken. Each calibration curve was averaged across three independent measurements.

For intensity-based calibration, a ratiometric approach was used. One red-channel (800 μs delay) and one green-channel (0 μs delay) image were taken at each pO_2. Reference-controlled phosphorescence intensity was calculated as red-to-green intensity ratio between the two channels and the reciprocal of this ratio was plotted over oxygen tensions to generate the intensity calibration curve.

For lifetime-based calibration, a series of red-channel/phosphorescence images were taken with the delay times set between the flash and the camera exposure varying from 0 to 10 ms. The intensity over delay time plot was obtained at each pO_2, and the phosphorescence lifetime τ was extracted from the curve. The reciprocal of the lifetime τ was then plotted over oxygen tensions to generate the lifetime calibration curve.

3.2.3 SENSING TISSUE ISCHEMIA IN HINDLIMB USING AN *IN VIVO* RAT MODEL

Animal housing and maintenance: A total of eight Sprague-Dawley rats, weighing an average of 275 grams, were used. All rat procedures were performed within the Beth Israel Deaconess Medical Center animal facility. All members of the research team had completed the necessary CITI and LATA training modules for The Humane Care and Use of the Laboratory Rat, Aseptic Surgery of Rodents, Anesthesia and Analgesia of Rodents, Laboratory Rabbit, Laboratory Canine, and Laboratory Animals. The animal surgery protocol was reviewed and approved by the Institutional Animal Care and Use Committee (IACUC) at the Beth Israel Deaconess Medical Center.

Anesthesia: The rats were placed into an induction chamber with 3% isoflurane in 100% oxygen at a flow rate of 1L/min. When the rat was unresponsive to external stimuli, it was removed from the induction chamber and placed on a nose cone for maintenance of anesthesia. General anesthesia was maintained by administering 2% isoflurane at a 1L/min flow rate.

Vessel exposure and occlusion: After inducing a complete state of anesthesia, the abdomen, thigh and ventral side of the animal's hind limb were shaved and aseptically prepared for surgery. Rats were positioned on their back and fixed in an X-shape using tape. A linear skin incision of 3 cm was made at the *linea alba* to expose the abdominal cavity. After cautious retraction of intra-abdominal organs, the retroperitoneal cavity was opened to ensure an optimal exposure of the descending aorta. Normal transdermal pO_2 was first measured on the left hind limb as a control (obtained under normal perfusion). A Clark electrode (Unisense, Aarhus, Denmark) was inserted into the gastrocnemius muscles of the hind limb of the rats to monitor the real-time in-tissue oxygen tension. The sensing bandage was painted onto the shaved skin above region monitored by the electrode. The bandage was allowed to dry in air for 1 minute, and the barrier layer was applied. Equilibrium red- and green-channel images were captured after 15 min. After collecting images on the control leg, hindlimb ischemia was induced by clamping the animal's descending aorta with surgical micro vessel clips. The sensing bandage was then applied to the right hind limb and the imaging procedures were repeated to measure the transdermal pO_2 under ischemic conditions. Tissue pO_2 imaged were generated by calculating the intensity ratio between the red- and green-channel images and calibrated to the intensity calibration curve described in Section 3.2.2.

Euthanasia: The rats were euthanized while under anesthesia by opening the diaphragm to elicit iatrogenic pneumothorax. They were then placed in a euthanasia chamber and 100% CO_2 was introduced. A fill rate of 10% to 30% of the chamber volume per minute with carbon dioxide (added to the existing air in the chamber) was used to achieve a balanced gas mixture and induce rapid unconsciousness with minimal distress to the animals. Death was confirmed by noting the animal's fixed and dilated pupils.

3.2.4 Measuring burn wound oxygenation on porcine skin explants

Full-thickness burns were created on freshly excised porcine skin *ex vivo* by bringing a brass rod, heated to 150°C, in contact with the surface of the skin for 15 seconds. Burn tissue damage was confirmed by histological analysis using hematoxylin and eosin staining. The oxygen-sensing bandage was applied 1 hour after the burn had been created, and allowed 1 min to dry in air. The bandage was also applied to an unburned skin sample that served as a control. The barrier layer was applied, and red- and green-channel images were taken both immediately and after 15 minutes of equilibration.

Tissue oxygenation in the *ex vivo* burn models was quantified based on phosphorescence intensity or lifetime. For intensity-based measurements, an 800 μs camera delay time was used while capturing the red-channel image to completely eliminate the skin autofluorescence background. The intensity of the red-channel image was divided by the intensity of its co-registered green-channel image and reconstructed into a ratiometric image using Matlab. 2-D tissue oxygenation maps were then obtained by correlating the intensity of the ratiometric image with pO_2 values at each image pixel, using the intensity calibration curve described in Section 3.2.2. For lifetime-based measurements, three points on each decay curve were used for curve fitting to extract the phosphorescence lifetime τ. The lifetime at each image pixel was then correlated to pO_2 using the lifetime calibration curve described in Section 3.2.2 to construct the 2-D tissue oxygenation map.

3.2.5 MONITORING WOUND PROGRESSION OF *IN VIVO* PORCINE FULL-THICKNESS BURNS

Animal housing and maintenance: A Yorkshire cross-bred female pig (Midwest Research Swine, Gibbon, MN) aged 6 months and weighing 40-50 kg was used. This study was reviewed and approved by the Institutional Animal Care and Use Committee (IACUC) at the United States Army Institute of Surgical Research (USAISR, JBSA Fort Sam Houston, TX). All animals received care in strict compliance with the 2011 *Guide for the Care and Use of Laboratory Animals* by the National Research Council and were maintained in a facility accredited by the Association for Assessment and Accreditation of Laboratory Animal Care International (AAALAC, Int.).

Anesthesia, pre- and post-operative care: Pigs were anesthetized with Telazol®(6 mg/kg), intubated and maintained on isoflurane throughout the procedure. A 100 μg Fentanyl patch was applied to the right ear for pain management. Prior to completion of the procedure, 4 mg hydromorphone was given intramuscularly for 6-8 hours of pain management. Following procedures, wound dressings, consisting of antibiotic-impregnated petrolatum (Xeroform™) and cotton gauze, were secured to the wound beds for 7 days with Ioban™. The dressing was removed at day 7 post operation. For follow-up observations, pigs were sedated with ketamine 10 mg/kg and maintained on isoflurane.

Burn creation: Five 6-cm wounds were marked (4 cm from each other and 2 cm from the spine) on each dorsal side of the animal and edges were tattooed. To create full-thickness burn, a brass cylinder (6 cm diameter) heated to 100°C was applied to the tattooed circles for 30 seconds. The total wound area accounted for less than 10% total body surface area. The animal was allowed to recover for 7 days during which time a burn eschar developed.

For oxygen assessment, the sensing bandage was painted across the boundary of a burn wound. The camera was positioned so that the field of view spanned across a region that included both the tissue directly affected by the burn injury and the adjacent unburned skin. The barrier layer was applied and the bandage was allowed to equilibrate for 15 min. A green-channel image of the reference dye was captured with the 510/10 nm filter. The red-channel image was captured using the 700/70 nm filter with the camera delay time set to 800 μs to eliminate the skin autofluorescence background. Ratiometric images were constructed by plotting the intensity ratio between the red- and green-channel images, and a tissue oxygenation map was obtained by applying intensity calibration to the ratiometric image. A follow-up assessment 7 days post-burn was performed to monitor the progression of the burn injury.

3.2.6 MONITORING INTEGRATION OF FULL-THICKNESS AND PARTIAL THICKNESS SKIN GRAFTS USING IN VIVO PORCINE GRAFT MODELS

Animal housing and maintenance: The animal used in this experiment, the housing and maintenance procedures were the same as described in Section 3.2.5.

Anesthesia, pre- and post-operative care: Pigs were anesthetized with Telazol®(6 mg/kg), intubated and maintained on isoflurane throughout the procedure. The back of the pig was sterilized by prepping with povidone-iodine solution and sterile surgical field was maintained throughout the procedure. Following suturing of the skin graft, wound dressings consisting of a bolster containing antibiotic-impregnated petrolatum (Xeroform™) and cotton gauze were secured to the wound bed for 7 days. Additional protective dressing consisting of Ioban™and cloth jacket were applied. The dressing was removed 7 days post operation.

Excision and grafting: Five 6-cm wounds were marked (4 cm from each other and 2 cm from the spine) on each dorsal side of the animal and edges were tattooed. Total wound area was less than 10% total body surface area. After full-thickness excision down to muscle fascia, wounds were covered with split-thickness autologous skin from a hindlimb donor site. Autografts of 30/1000th of an inch thickness were harvested using a Zimmer pneumatic dermatome (Zimmer Surgical, Inc., Dover, OH) and cut to fit the defects. Full-thickness autograft skin was harvested from the original full-thickness wound creation and defatted surgically.

Tissue oxygenation in the full-thickness and partial-thickness skin grafts was assessed both immediately post grafting, as well as at 1-month follow up. The sensing bandage was painted across the boundary of the graft, and the camera was positioned so that the field of view spanned across a region that included both the graft and the skin immediately surrounding it. The barrier layer was applied and the bandage was allowed to equilibrate for 15 min. As above, a green-channel image of the reference dye was captured with the 510/10 nm filter. The red-channel image was captured using the 700/70 nm filter with the camera delay time set to 800 μs to eliminate the skin auto-fluorescence background. Ratiometric images were constructed by plotting the intensity ratio between the red- and green-channel images, and tissue oxygenation map was obtained by applying intensity calibration to the ratiometric image.

3.3 RESULTS AND DISCUSSION

3.3.1 QUANTIFYING OXYGEN WITH RATIOMETRIC PHOSPHORESCENCE IMAGING AND TISSUE AUTO-FLUORESCENCE BACKGROUND REMOVAL

The emission intensity and lifetime of a phosphorescent molecule can be used to quantify the O_2 content in the molecule's environment based on an oxygen-dependent quenching process. Molecular oxygen interacts with the excited triplet state of the phosphor through collisions, leading to the exchange of energy resulting in the phosphor's non-radiative decay to its ground state. Therefore, both the phosphorescence intensity and lifetime decrease as a result of increasing oxygen content in the environment. Recall from Eq. 2.6 in Chapter 2 that the relationship between phosphorescence intensity/lifetime and pO_2 is described by the Stern-Volmer equation: [139]

$$\frac{1}{\tau} = \frac{1}{\tau_0} + k_q(pO_2) \tag{3.1}$$

where τ is the phosphorescence lifetime at a given oxygen pO_2, τ_0 is the same measurement in the absence of oxygen, and k_q is the quenching constant. While constructing the imaging device for the oxygen-sensing bandage, a 700/70 nm bandpass filter was chosen to capture the phosphorescence emission of the oxygen-sensing Oxyphor R2 molecule (λ_{em}= 690 nm). The quantification of pO_2 has been achieved on this camera-based imaging device using either phosphorescence intensity or lifetime measurement. The intensity-based approach is described here, and the lifetime approach will be discussed in detail in Section 3.3.2.

Ratiometric approaches take advantage of the presence of an additional fluorophore in the bandage that provides an oxygen-independent signal as a reference and internal, built-in control.[140] In the case of the paint-on bandage described in this work, phosphors and fluorophores are evenly distributed throughout the bandage formulation, such that the phosphorescence/fluorescence ratio is self-calibrated for any variation in bandage thickness over the tissue surface. All phosphorescence measurements recorded in the "red-channel" image were accompanied by a corresponding "green-channel" image of the Coumarin 500 reference dye. The red-to-green intensity ratio was calibrated to oxygen partial pressure.

Skin tissue is known to have strong autofluorescence that can interfere with the measurement of comparatively weak phosphorescence emission from the oxygen-sensing bandage. To actively suppress the short-lived tissue autofluorescence and extract only the longer-lifetime phosphorescence signal of interest, a delay-trigger mechanism was introduced. By opening the camera shutter several hundred microseconds after the flash, fluorescence emission from the skin is gated out, and the long-lived phosphorescence emission can be selectively captured. The maximum phosphorescence-to-autofluorescence signal for the Oxyphor-containing bandage and imaging system was found to occur at a delay of 800 μs. By using this approach, the delay-triggered camera exposure effectively eliminated the tissue autofluorescence background, and significantly increased the system's signal-to-noise ratio. The O_2 sensing calibration curve obtained using this intensity approach is shown in Figure 3.3.1.

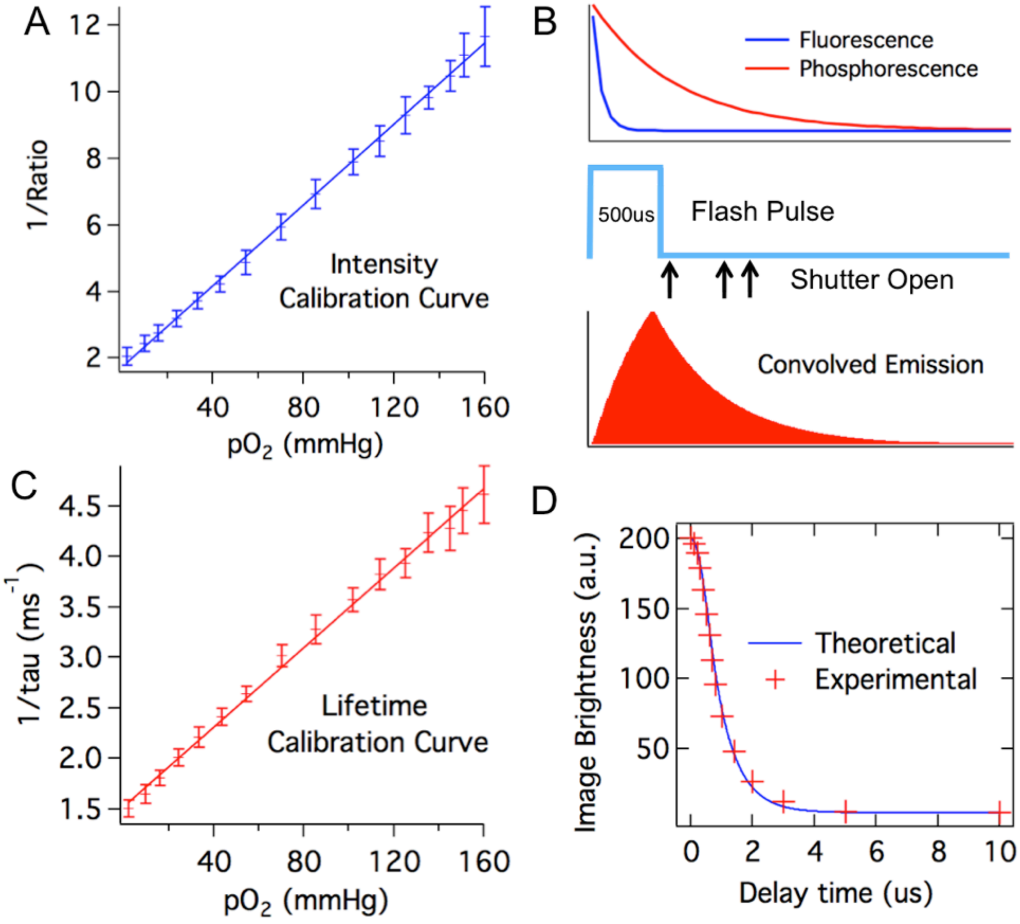

Figure 3.3.1: Calibrating the oxygen-sensing bandage. **A**: System calibration curve based on phosphorescence intensity. Phosphorescence intensity is expressed as red-to-green channel intensity ratio. **B**: Timing events during the imaging process, showing the 500 μs illumination flash pulse relative to the phosphorescence decay of the oxygen sensor and the fluorescence decay of the reference dye. Over the course of several repeated images, the camera shutter opens after predetermined delay times following the flash pulse. Red curve: the phosphorescence emission convolved with the flash pulse. **C**: System calibration curve based on phosphorescence lifetime. **D**: Calculated image intensity at camera delay time between 0 and 10 ms for Oxyphor R2-containing bandage under 0 mmHg pO_2. Calculation of image brightness was based on the assumption that the flash pulse is a square pulse with 500 μs pulse duration, and the phosphorescence lifetime of Oxyphor R2 under 0 mmHg pO_2 is 700 μs.

3.3.2 PHOSPHORESCENCE LIFETIME IMAGING USING A DELAY-TRIGGERED CAMERA

As a means of quantifying oxygen, the phosphorescence lifetime signal is advantageous in that it is independent of any variation in excitation intensities or the amount of phosphor present in an imaged region. [141] Unfortunately, instruments for carrying out lifetime imaging often involve advanced light sources and high-speed detectors that can be expensive and cumbersome to use. [142] Typically, a short (generally nanosecond or shorter) excitation pulse is delivered to a phosphorescent sample, and the photon counts incident upon a detector are measured in a series of discretized time "bins," which group photon counts according to their arrival time at the detector. For a more straightforward and cost effective approach to obtaining two-dimensional maps of phosphorescence lifetime from the paint-on bandage, we utilized regular flash units as light source coupled with the delay-trigger system described above, alongside a mathematical model of phosphorescence decay. The flash units chosen for this study could be operated across a range of power settings, which was found to be advantageous.

Setting the flash units for lower power operation engages built-in circuitry that acts to rapidly quench light emission once the lamps reach a predetermined level, creating a burst of light similar to a square-wave shaped pulse. This enabled the blue excitation light provided by the flash units to be approximated as a square-wave shaped pulse with 500 μs duration (Figure 3.3.1B). The phosphorescence decay of sensor molecules inside the bandage is therefore convolved with the excitation pulse. This convolved decay curve can be generated by taking phosphorescence images of the bandage with a series of delay times set between the flash triggering time and the camera exposure, as shown in Figure 3.3.1. Then a deconvolution algorithm can be applied to this instrument measured decay curve to extract the lifetime of phosphorescence.

To achieve this, a theoretical model was created to describe the instrument-measured decay curve. As described in Chapter 2, the phosphorescence emission by individual phosphor molecules decays over time following:

$$I(t) = I_0 e^{\frac{-t}{\tau_P}} \tag{3.2}$$

where I_0 and $I(t)$ are the phosphorescence intensity at time zero and time t, respectively, and τ_P is the phosphorescence lifetime of the sensor molecule. Assuming the flash pulse is a square wave $P(t)$, the phosphorescence signal convolved with the excitation pulse can be described as:

$$I_C(t) = (I * P)(t) = \int_0^t I(t-x)P(x)dx \tag{3.3}$$

which is a two-segment curve as shown in Figure 3.3.1B. Since the camera exposure time is much longer (15 ms) compared to the duration of the excitation pulse and the phosphorescence emission, the camera effectively integrates all incident phosphorescence intensity after the trigger time point. The brightness of the image captured by the camera as a function of the camera delay time is also a two-segment curve. For camera delay greater than the flash duration, it follows an exponential decay:

$$B(D) = \int_0^\infty I_c(t)dt = N\tau_P^2 I_0 (e^{\frac{\tau_F}{\tau_P}} - 1)e^{-D/\tau_P}, D > \tau_F \tag{3.4}$$

where B is the brightness of the camera-captured image and D is the delay time set between the onset of flash excitation and camera exposure, N is the number of emitters triggered per unit time of exposure to the flash pulse (s^{-1}), and τ_F is the flash pulse duration (s). Using this model, the theoretical intensity-delay curve can be plotted by inserting the measured flash duration (500 μs) and the unquenched phosphorescence lifetime of the Oxyphor R2 (700 μs) found in the literature. [63] The calculated decay curve matches very well with the experimental curve measured under zero oxygen partial pressure as shown in Figure 3.3.1D, validating the model as an accurate description of the system.

It should be noted from Eq. 3.4 that for delay time t_d greater than the flash duration τ_F, the curve follows an exponential decay with a rate constant equal to the phosphorescence lifetime of the sensor molecules. The unquenched phosphorescence lifetime of Oxyphor R2 extracted from the acquired decay curve was measured to be $692 \pm 20\mu s$, which closely matches the reported lifetime of the molecule under similar conditions ($701 \pm 12\mu s$). Using this approach, the phosphorescence lifetime of the molecules inside the sensing bandage under different oxygen partial pressures was obtained from the experimentally measured intensity-delay curves under each pO_2 condition; in this manner, a lifetime calibration curve was generated for the system (Figure 3.3.1C).

3.3.3 Sensing tissue ischemia in rats during arterial ligation

In a first validation experiment, the oxygen-sensing bandage was used to directly measure transdermal oxygenation through intact skin, where the equilibrium oxygen partial pressure reported by the bandage reflects the perfusion status of the underlying tissue. This application is of clinical relevance in the early detection of ischemic conditions and can be applied to monitor tissue ischemia at the engraftment sites on patients following graft, flap or other reconstructive surgeries for the early detection of graft/flap failure due to poor tissue perfusion. It can also be used to monitor other ischemic conditions such as recurrent decubitus and diabetic ulcers, where tissue oxygenation plays a critical role in determining whether an ulcer will remain unhealed. [115, 143, 144]

To demonstrate the oxygen-sensing bandage's ability to report tissue oxygenation *in vivo*, the bandage was applied to the hind limbs of eight rats where tissue ischemia was induced by arterial ligation. The average baseline intramuscular pO_2 in the rat's hindlimb recorded by a needle-based Clark electrode was 70 mmHg. The oxygen-sensing bandage was painted onto the skin of the rat's hindlimb directly above the region monitored by the Clark electrode. A two-dimensional map of transdermal pO_2 measured by the oxygen-sensing bandage under normal conditions is shown in Figure 3.3.2. Under normal perfusion, the average transdermal pO_2 measured was 91.3 mmHg. When the descending aorta of the rats was surgically ligated, the intramuscular pO_2 measured by the Clark electrode decreased to 25 mmHg within 3 minutes and maintained between 20 and 30 mmHg throughout the duration of the ligation. This ischemia leads to a concomitant decrease in the observed transdermal pO_2 as shown in Figure 3.3.2B. The average transdermal pO_2 under ischemia after 15 min of vessel ligation recorded by the oxygen-sensing bandage is 51.9 mmHg.

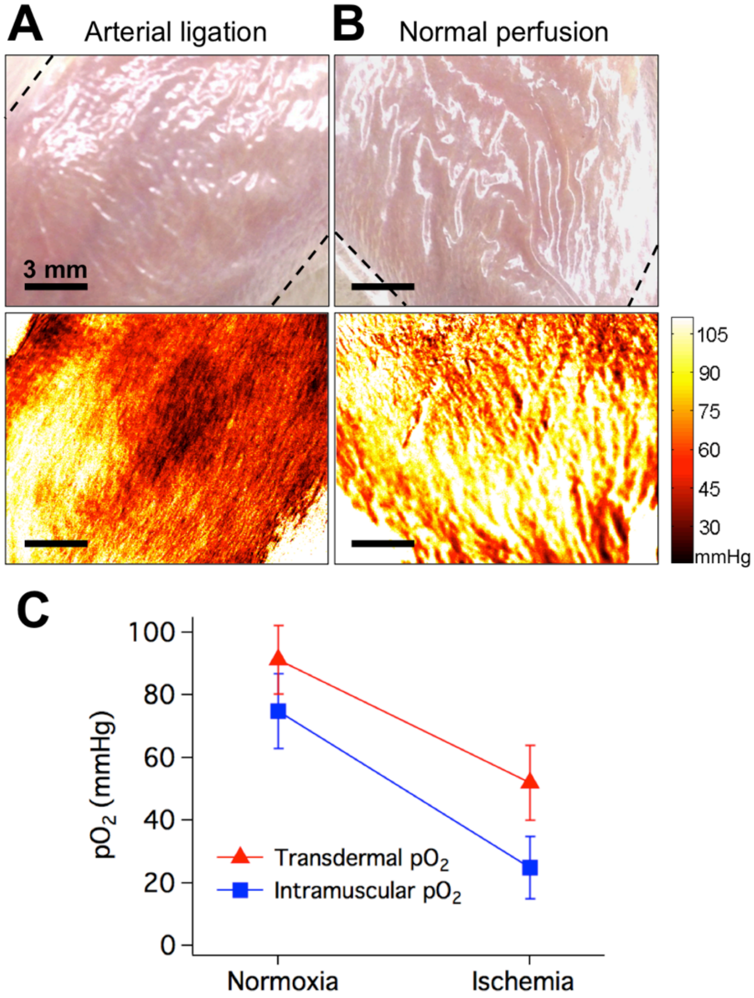

Figure 3.3.2: Sensing tissue ischemia in the rat hindlimb. Red indicates lower tissue oxygenation and yellow indicates higher tissue oxygenation. Dashed lines indicate boundaries of bandage-covered region. **A**: Photograph (top) and tissue oxygenation map (bottom) taken during arterial ligation (lower tissue oxygenation). **B**: Photograph (top) and tissue oxygenation map (bottom) taken under normal perfusion (higher tissue oxygenation). **C** Transdermal pO_2 measured by the sensing bandage and intramuscular pO_2 measured by the Clark electrode during normal perfusion and ischemia induced by arterial ligation.

The results measured by both methods were summarized in Figure 3.3.2C. The subcutaneous pO_2 measured by the Clark electrode under normoxic and ischemic conditions were consistent with the values measured by polarographic electrodes and $TcpO_2$ devices reported in the literature [145, 146]. However, the transdermal pO_2 reported by the oxygen-sensing bandage was consistently higher than that measured with Clark electrode. This is expected because the surface of skin is partially oxygenated by room air through diffusion through porous structures. [114] Additionally, the absolute measurements by the bandage should always be higher, since it is experiencing a mixture of both tissue and room oxygen levels. If necessary, this difference could be systematically accounted for and corrected, as it does not affect the bandage's ability to sense the magnitude of changes in tissue oxygenation, as can be seen on Figure 3.3.2C.

3.3.4 Visualizing burns in porcine skin explants based on reduced oxygen consumption of necrotic tissues

In addition to direct measurement of tissue oxygenation, the oxygen-sensing bandage can also be used to quantify average oxygen consumption rates by measuring the difference between initial and equilibrium pO_2 after applying the barrier layer. Given that all living, healthy mammalian tissues consume oxygen, this provides a tissue"vitality" map, and is especially useful in detecting tissue that is metabolically compromised (*e.g.*, necrotic tissue in burns). Thus, in this context the bandage can potentially serve as a guide during burn debridement as well as in monitoring flap/graft viability in patients.

Acute and preoperative burns are characterized by the presence of a necrotic tissue layer, within which protein components of the dermis are coagulated along with dead cells. [147] Surrounding this damaged tissue is a region characterized by reduced perfusion, where both cell viability and metabolism can be compromised. Thus, when monitored transdermally, the oxygen consumption rate of tissue located at a burn wound is lower compared to healthy skin regions (Figure 3.2.1D), as there is less healthy tissue consuming O_2. During standard-of-care debridement surgeries, it is not always possible to definitively determine where the necrotic zone ends and the zone of decreased perfusion begins, forcing surgeons to make subjective judgements that potentially subject patients to either the cosmetic consequences of overzealous debridement or the poor surgical outcomes associated with insufficient debridement. A technique based on measurement of tissue oxygen tension could allow the mapping of transdermal oxygen consumption rates for rapid visual identification of necrotic tissue within burn wound beds, potentially enhancing surgical efficacy and work flow.

To test the oxygen-sensing bandage's ability to visualize necrotic tissue in burns via oxygen consumption mapping, the bandage was first tested *ex vivo*. Full-thickness circular burns were created on freshly excised (still viable) porcine skin, and the oxygen-sensing bandage was painted over the burn as well as the surrounding skin area. Phosphorescence emission from the sensing bandage was first taken immediately after the application of the Tegaderm barrier layer to capture the initial pO_2 at the measurement site. After 15 minutes, images were taken again to capture the final oxygen partial pressure in the bandage environment after the bandage was given time to equilibrate with the underlying tissue. Percent tissue oxygen consumption rate (%) at each image pixel was calculated by taking the difference between the initial and equilibrium pO_2 and normalizing this value as a percentage of the maximum consumption measured in healthy skin.

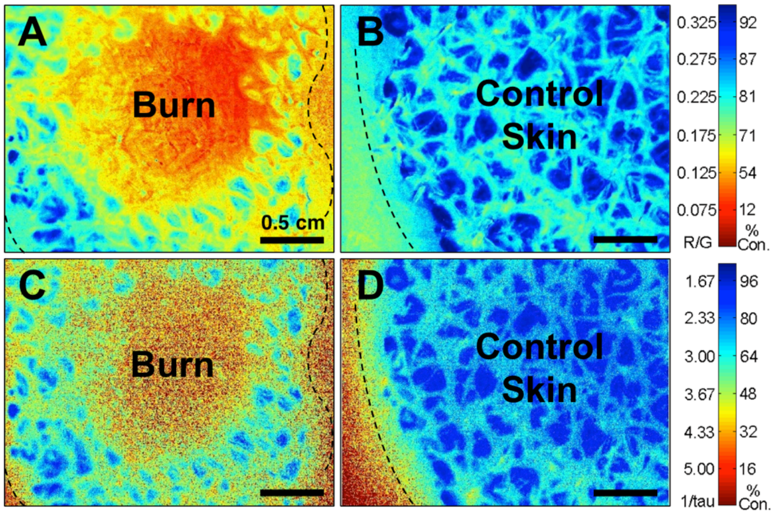

Figure 3.3.3: Equilibrium oxygen maps showing a decrease of tissue oxygen consumption (expressed as normalized % consumption) by compromised tissue on freshly excised porcine skin obtained using intensity- and lifetime-based measurement approaches. Blue indicates higher oxygen consumption by tissues. Red indicates lower oxygen consumption by tissues (provides a visual "warning" for physiologically compromised tissue in clinical applications). Dashed line indicates boundaries of bandage-covered region. Images shown for **A**: Circular burn imaged using intensity approach; **B**: Control skin imaged using intensity approach; **C**: Circular burn imaged using lifetime approach; **D**: Control skin imaged using lifetime approach.

The two-dimensional oxygen maps of burn wounds and control healthy skin were obtained using both intensity- and lifetime-based approaches and the results are compared in Figure 3.3.3. In the oxygen map generated using the ratiometric intensity-based approach, the circular burn region at the center of the skin sample can be seen to have a lower phosphorescence ratio compared to the surrounding skin area, which corresponds to higher equilibrium oxygen partial pressure, and thus lower oxygen consumption. This is consistent with the lower O_2 consumption rate of necrotic tissue. This is in clear contrast to the healthy control skin, where the equilibrium oxygen was low across the bandage-covered region. In the lifetime-based image of the burn sample, the circular burn region demonstrated shorter phosphorescence lifetime of the bandage sensor, which also corresponds to higher oxygen partial pressure and lower oxygen consumption in the region.

When comparing the images obtained using the intensity- and lifetime-approach, it can be observed that the oxygen consumption rates measured by the two methods show similar patterns across the surface of the samples. The oxygen consumption values obtained using the intensity- and lifetime-calibration curves also correlate well with each other. Notably, it is easier to distinguish bandage-covered regions from bare skin on the lifetime-based images. This is because the signal generated from uncovered, bare skin contains only short-lived autofluorescence signal, the lifetime of which can be distinguished from that of the long-lived phosphorescence emission within the bandage. It is also worthwhile to note that in comparing the images of the burn wound (Figure 3.3.3A and C), the image of the burn region generated by the lifetime approach contains more noise. This is the direct result of the higher intrinsic error associated with high-oxygen tension lifetime measurements: when pO_2 values are high, the lifetime of the sensor molecule becomes much shorter and closer to zero, thereby increasing the intrinsic noise of the imaging system and the associated determination of phosphorescence lifetime.

As the surface of skin is not perfectly flat, surface roughness and tissue curvature can affect measurements in three ways. First, the natural curvature of the skin can in some cases cause only portions of tissue to lie within the camera's focal plane. While this may be challenging in future applications, the images taken in this study were acquired from relatively small, flat regions of skin such that the imaged tissue fell within the depth-of-field of the camera lens. Secondly, since the bandage is applied to the skin as a liquid, it coats the skin according to its surface topography, which means that the thickness of the bandage can vary with the small ridges and grooves of the skin. This effect is not expected to interfere with oxygen measurements, since the use of a reference dye effectively controls for the uneven distribution of bandage thickness, and lifetime measurements will not be effected by bandage thickness. Under certain conditions, surface roughness can lead to uneven attachment of the barrier layer. Small air pockets may form between the barrier layer and the natural grooves in the skin, which would, in turn, affect the oxygen equilibration process between the bandage and the underlying tissue. When present, these air bubbles would lead to the measurement of oxygen consumption at values slightly lower than the rest of the skin.

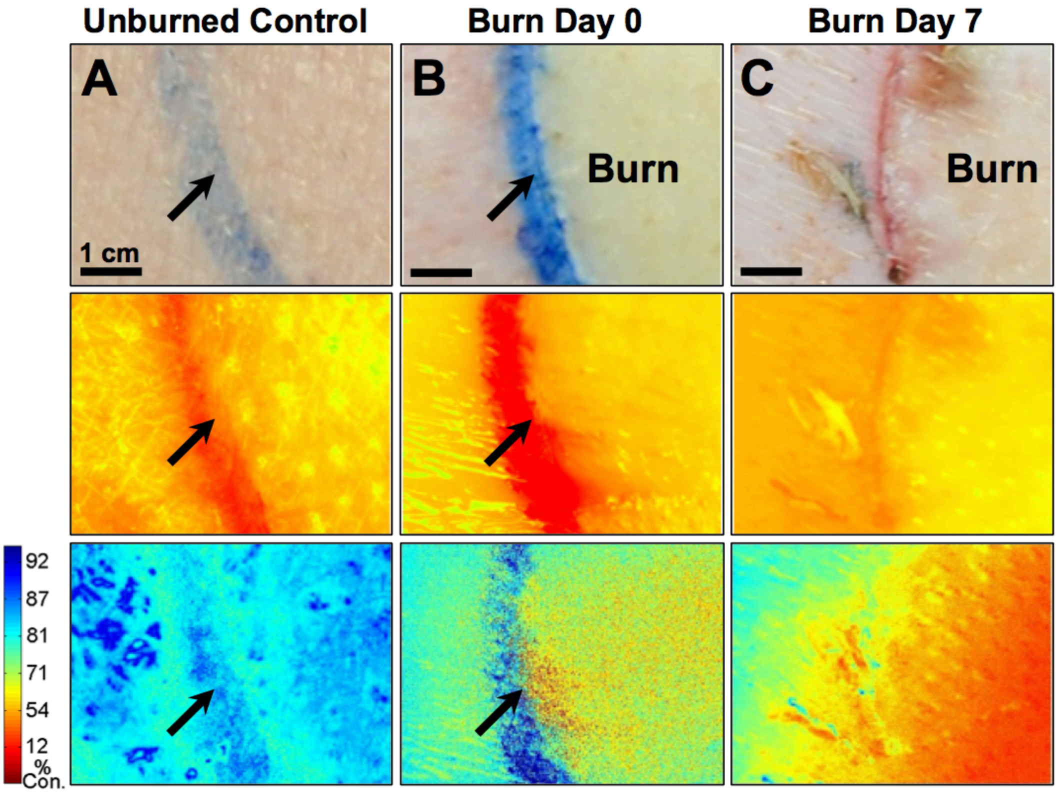

Figure 3.3.4: Progression of a full-thickness burn on the paraspinal skin of a Yorkshire pig monitored by oxygen-sensing paint-on bandage. Images shown for **A**: control skin; **B**: immediately post-burn; and **C**: 7 days post-burn. Top row: regular photographs; middle row: emission at 700 nm, where oxygen-dependent phosphorescence signals are overwhelmed by the skin autofluorescence background; bottom-row: percent oxygen consumption (%) maps obtained after eliminating autofluorescence. Blue indicates higher oxygen consumption by tissues. Red indicates lower oxygen consumption by tissues. Arrows indicate ink marks dividing burn and surrounding skin.

3.3.5 MONITORING *IN VIVO* BURN WOUND PROGRESSION USING OXYGEN-SENSING BANDAGE IN A PORCINE FULL-THICKNESS BURN MODEL

Following testing with porcine explants, the next set of experiments focused on the bandage's ability to monitor burn wounds *in vivo*. Full-thickness circular burns were established on the paraspinal skin of a Yorkshire pig. Burn wound oxygenation was measured with the oxygen-sensing bandage both immediately after the creation of the burn and 7 days post-insult. Normal color photographs of the burn and control regions are shown in the top panel of Figure 3.3.4. The middle panel shows the bandage emission captured at 700 nm without the delay exposure setting; therefore these images contain significant skin autofluorescence background. The bottom panels show the ratiometric intensity-based oxygen maps captured by the camera, where the autofluorescence background is eliminated by introducing the delay exposure mechanism. The early stages of tissue necrosis can be observed immediately after the creation of the burn as a region with elevated equilibrium pO_2 due to decreased tissue oxygen consumption. Progression of the burn injuries was observed during the 7-day follow-up assessment. A higher deviation from normal oxygen consumption rate was found, which correlated with an increased severity of tissue necrosis. Importantly, the oxygen-sensing bandage revealed that the area of necrosis had extended beyond the original burn region, an observation not easily made from the color photograph.

These results match the physiological changes known to occur following burn injuries. The local response to burn gives rise to three distinct tissue zones: the zones of coagulation, stasis, and hyperemia. The zone of coagulation refers to the central necrotic region and is characterized by irreversible tissue loss; the surrounding zone of stasis is potentially salvageable, but can convert into complete tissue loss if the perfusion is poor; the outermost zone of hyperemia features increased perfusion as a response to the insult. In the photograph of the burn wound taken immediately following the injury, the region inside the tattoo line shows apparent changes in tissue color (blanching), which marks irreversible cell necrosis. The O_2 consumption map shows a corresponding decrease of pO_2 consumption in the necrotic region, and also a slight elevation of pO_2 in the region immediately outside the tattoo line. This regional elevation can likely be attributed to increased perfusion corresponding to the zone of hyperemia. In the O_2 consumption map obtained during the 7-day follow-up, the region inside the tattoo showed greater deviation from normal tissue consumption, which can be explained by a deepening of the wound. The area immediately surrounding the original burned region also showed significant deviation from normal consumption, which is to be linked to wound progression and widening from additional tissue loss. [148]

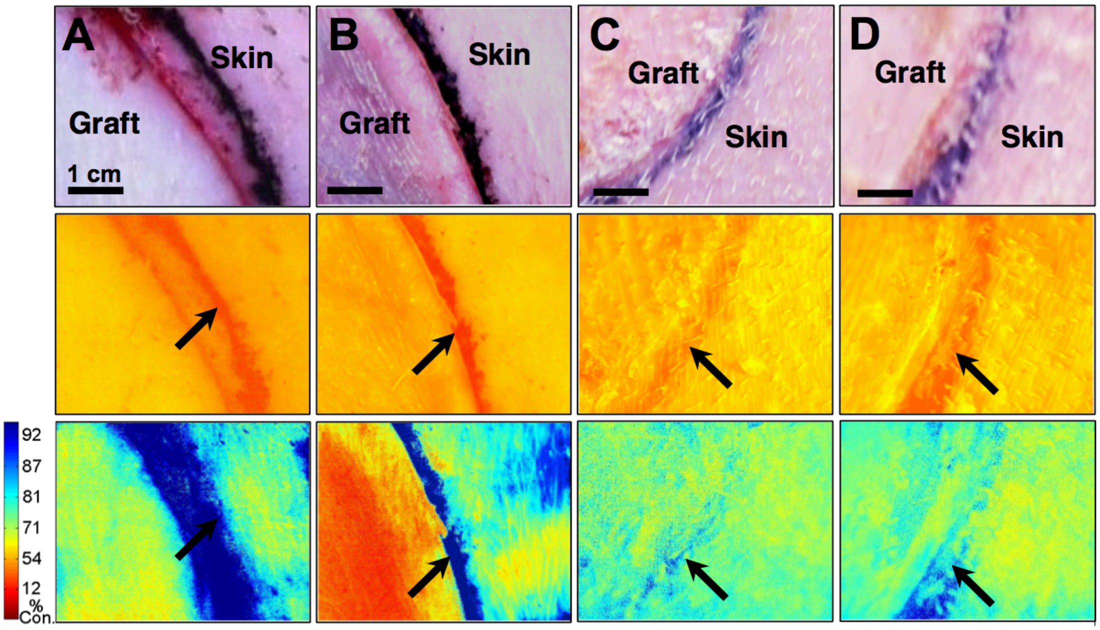

Figure 3.3.5: Incorporation of full-thickness and partial-thickness skin grafts on the paraspinal skin of a Yorkshire pig observed with the oxygen-sensing paint-on bandage. Top row: regular photographs; middle row: emission at 700 nm, showing that oxygen-dependent phosphorescence signals are overwhelmed by the skin autofluorescence background; bottom-row: percent oxygen consumption (%) maps obtained after eliminating autofluorescence, where blue indicates higher oxygen consumption by tissues. Red indicates lower oxygen consumption by tissues. Arrows indicate tattoo marks dividing grafts and surrounding skin. Images shown for **A**: full-thickness graft immediately post-grafting; **B**: partial-thickness graft immediately post-grafting; **C**: full-thickness graft at 1-month graft assessment; **D**: partial-thickness graft at 1-month graft assessment.

3.3.6 VISUALIZING *IN VIVO* GRAFT INCORPORATION USING THE OXYGEN-SENSING BANDAGE IN A PORCINE GRAFT MODEL

Skin transplants are commonly used in burn interventions, with full-thickness skin grafts providing the best functional and aesthetic outcomes in patients. [147] However, their application is limited as it is often difficult to obtain enough autologous full-thickness skin from a patient. [149] Thus, autologous partial-thickness skin grafts are frequently used because they can cover larger tissue areas while requiring less donor skin (especially when processed by a skin mesher). [150] Partial-thickness grafts, however, lack significant dermal structures and require oxygenation through direct diffusion from the underlying wound bed. Therefore, it is important for physicians to monitor the oxygenation of partial-thickness grafts to ensure they are successfully integrated following the engrafting procedures.

The oxygen-sensing bandage was tested on an *in vivo* porcine graft model that simulates the reconstructive surgical procedures used in many burn interventions. Full-thickness skin grafts and partial-thickness skin grafts were applied to circular excisional wounds established on the paraspinal skin of a Yorkshire pig. Graft oxygenation was measured with the oxygen-sensing bandage immediately post-grafting and during the 1-month follow-up assessment session. Full-thickness grafts (3.2.1E) containing all the layers of the skin, as well as their underlying supporting tissue, demonstrated normal or slightly decreased oxygen consumption rate immediately after grafting (Figure 3.3.5A). On the other hand, partial-thickness grafts (Figure 3.2.1F) were observed to have a much slower oxygen consumption rate (Figure 3.3.5B). The consumption rates for both the full- and partial-thickness grafts were observed to have resumed to normal level after one month, showing that both grafts were successfully integrated (Figure 3.3.5C, D).

3.4 Conclusions

A paint-on bandage was developed for non-invasive, two-dimensional mapping of tissue oxygenation and oxygen consumption using a camera-based device. The bandage contains oxygen-sensing molecules whose phosphorescence emission intensity and lifetime values change in a pO_2-dependent fashion. The system was tested on an *in vivo* rat ischemic limb model, which demonstrated its ability to sense tissue ischemia. It was then used to monitor the progression of burns in both *ex vivo* and *in vivo* porcine burn models. Lastly, it was applied to an *in vivo* porcine graft model to monitor the integration of full-thickness and partial-thickness skin grafts.

By incorporating oxygen-sensing capabilities into wound dressing materials, the transparent paint-on bandage described in this work may be applied to provide long-term wound protection and continuous access to the status of skin and wound oxygenation. This system has the potential to improve the clinical care of chronic ischemic wounds, burns, skin grafts/flaps, and other tissue injuries where tissue oxygenation plays an important role in the patient's prognosis. The bandage is composed of materials known to be biocompatible and/or materials already in clinical use, thereby potentially reducing the barrier to both in-human clinical trials and future clinical use. Additionally, the imaging device developed here is portable and stable, does not require bedside calibration, and can be easily engineered for bedside use. As a non-invasive, passive device for tissue oxygenation measurement of both intact and compromised skin, this technology has excellent translational potential. It will also facilitate the study of local regulation of skin oxygenation that may lead to a better understanding of a variety of skin conditions.

Note: Following the acceptance of this thesis, the work described in this chapter was published in Biomedical Optics Express. [151]

As a math atheist, I should be excused from this.

-Calvin (*Calvin & Hobbes*)

4

Non-linear approaches to pheomelanin imaging

4.1 INTRODUCTION

4.1.1 BRIEF OVERVIEW OF MELANOCYTE AND MELANIN BIOCHEMISTRY

Cutaneous primary melanoma is a disease commonly associated with the presence of visible pigmentation on the dermal surface. As such, it is often considered to be one of the more straightforward cancers to detect and resect. A well-established melanoma risk factor is excessive unprotected exposure to UV light, which results in the accumulation of DNA damage and oncogenic driver mutations. [152]

Fundamentally, melanoma is a disease of melanocytes, the dendritic, epidermal cell type in which the pigment melanin is synthesized. Mammalian dermal melanin is principally comprised of two chemical subtypes, eumelanin and pheomelanin (Figures 4.1.1 and 4.1.2). Eumelanin is an insoluble, blackish/brownish, heterogeneous polymer, created at least in part through the oxidative polymerization of *L*-DOPA to create 5,6-dihydroxyindole and 5,6-dihydroxyindole-2-carboxylic acid intermediates; the yellowish/reddish, alkali-soluble pheomelanin is formed through oxidation of cysteinyldopa precursors through intermediates involving benzothiazines and benzothiazoles. [153, 154] Examples of the former include squid-derived *Sepia* melanin and black hair, whereas examples of the latter include hair from individuals of pale complexion as well as hen feathers. [154]

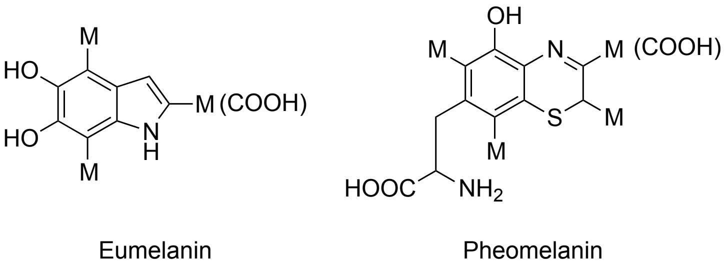

Figure 4.1.1: The primary Monomer subunits of eumelanin and pheomelanin (5,6-dihydroxyindole-2-carboxylic acids and benzothiazine derivatives, respectively). Note that pheomelanin also contains benzothiazones, as shown in 4.1.2. "M" represents an attachment point to an adjacent monomer subunit. Structures described in [155].

Within melanocytes, melanins are synthesized in specialized lysosome-related organelles known as melanosomes. Classical morphological studies describe melanosome development in terms of four stages. Stage I melanosomes, also known as premelanosomes, have not yet begun to synthesize pigment but contain characteristic membranous vesicles that resemble late endosomal multivesicular bodies. By stage II, melanosomes begin to develop a striated appearance on electron microscopy due to the presence of axially polarized intralumenal fibers, which serve as a receiving scaffold for melanin synthesis in later developmental stages. Melanin synthesis begins in stage III, and by stage IV intralumenal melanin deposition is sufficient to efface the appearance of melanosomal struc-

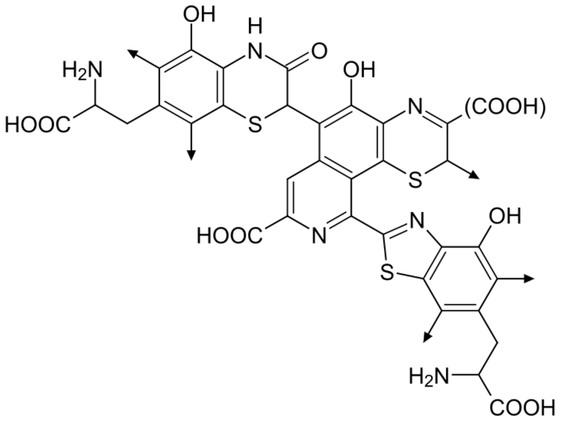

Figure 4.1.2: An example of the polymeric complexity typical of pheomelanins. Described in [156].

tural elements, such that the mature melanosome now appears to be a large "ball" of synthesized melanin. [157, 158]

Importantly, stages I-III of development occur in the perinuclear region; during stage IV, melanosomes bind the molecular motor kinesin and migrate along microtubules towards the cellular periphery. Upon arrival at the periphery, melanosomes detach from microtubule elements and associate with peripheral actin filaments through the molecular motor protein myosin Va, whereupon the melanosome is free to translate locally. [157, 158] Thus, retrograde movement along microtubules is prevented, resulting in the observed peripheral distribution of melanin-rich melanosomes. In dermal melanocytes, the final step occurs when peripheral melanosomes are transferred across the extracellular space and into neighboring keratinocytes. [1] Although the exact mechanism through which this process occurs remains unresolved, putative mechanisms include phagocytosis of melanosome-containing melanocyte dendrites by keratinocytes, direct membrane fusion, and melanocyte exocytosis of melanosomes followed by keratinocyte endocytosis.[157, 158]

---

[1] In addition to dermal melanocytes, there are other melanin-synthesizing cells that occur throughout the body, such as retinal pigment epithelium (RPE) cells and cells of the substantial nigra within the brain.

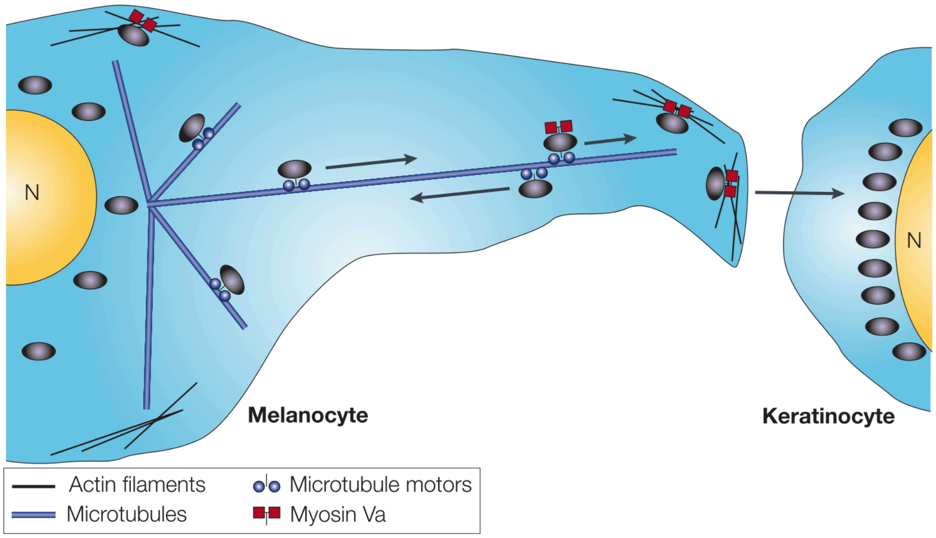

Figure 4.1.3: Schematic illustrating the peripheral migration and localization of stage IV melanosomes within dermal melanocytes, followed by their transfer to keratinocytes. Reproduced from [157].

For many years, the melanoma research and epidemiology community appreciated little functional difference between eumelanin and pheomelanin in terms of their photophysical and photoprotective properties. Although it was clear that light-skinned individuals were at a higher risk for developing UV-related melanoma than dark-skinned individuals, the chromophore composition of skin was often described simply in terms of overall "melanin" content and melanin was considered to be broadly protective against melanoma. [152, 159] However, observations including the fact that melanoma rates remain low even in albino africans (who lack the ability to synthesize any melanins) gave rise to the notion that more subtle aspects of melanin and/or melanocyte biochemistry may play a role in determining melanoma risk. Subsequent *in vitro* studies on human melanocytes demonstrated a higher incidence of UVA-induced reactive oxygen species and single-stranded DNA breaks in pheomelanin-rich cells, suggesting that a relative or absolute preponderance of pheomelanin over eumelanin may *ceteris paribus* raise UV-mediated melanoma risk.[152, 160–163] This hypothesis was supported by the well-known observation that "redheads," or paleskinned individuals with fair skin and freckles, have the highest risk of developing melanoma, as the red-head phenotype stems from a genetic polymorphism (described below) that leads to excessive or exclusive production of pheomelanin. [159, 164]

While the evidence to support a UV-based route to melanocyte oncogenesis is incontrovertible, recent work suggests the existence of an alternative melanocyte oncogenesis pathway that is independent of UV-mediated mechanisms. [163] In 2012, Mitra *et al.* created a series of mutant mice on a shared C57BL/6 background that differ in their pigmentation phenotypes. The first set of mice, black/wild type, are black in appearance and create normal quantities of both eumelanin and pheomelanin, the two primary pigments in human skin. The second set of mice, termed "redhead" mice, are homozygous for an inactivating polymorphism in the melanocortin 1 receptor gene *MC1R*, hormonal stimulation of which in WT mice results in a local switch from pheomelanin production to eumelanin production; thus, mice with premature termination of the *Mc1r* transcript ($Mc1r^{e/e}$ mice) synthesize only pheomelanin and exhibit a redhead phenotype. The authors also created an "albino" mouse line with an inactivating mutation at the tyrosinase locus ($Tyr^{c/c}$), which renders them incapable of producing any melanin at all (*i.e.*, neither eumelanin nor pheomelanin). Crucially, the mice additionally possessed both i) transgenic stem cell factor expressed under the keratin 14 promoter (*K14-SCF*), which resulted in epidermal melanocyte localization similar to that observed in human skin, and ii) an inducible, melanocyte-specific expression system for oncogenic BRAF^{V600E} controlled through tamoxifen-mediated activation of Cre recombinase ($Braf^{CA/CA}$ and $Tyr\text{-}Cre(ER)^{T2}$, respectively). Induction of oncogenic BRAF^{V600E} is known in humans, mice, and zebrafish to promote the formation of benign nevi; in this context, malignant transformation to melanoma is constrained through endogenous, senescence pathways that curb further cellular proliferation. [163, 165–169] If these protective, anti-proliferative mechanisms are eliminated, for example through mutational silencing of *CDKN2A*, *TP53*, or *PTEN*, then progression to malignant melanoma will ensue. [163, 165–169]

Following the activation of Cre recombinase and induction of oncogenic BRAF^{V600E}, Mitra *et al.*

kept all animals in UV-light-free environments and tracked their survival over a period of one year (4.1.4); it was observed that over 50% of *Mc1r*$^{e/e}$ red mice, which synthesize only pheomelanin, developed tumors, as compared to much lower numbers for the black and albino control groups (Figure 4.1.4). [163] This difference was observed for sets of animals that both did and did not carry the *K14-SCF* transgene, suggesting the mechanism is independent of melanocyte localization. Based on these and other experiments described within the same work, Mitra *et al.* propose the existence of a UV-independent, pheomelanin-mediated carcinogenesis pathway involving non-UV-mediated oxidative DNA damage.

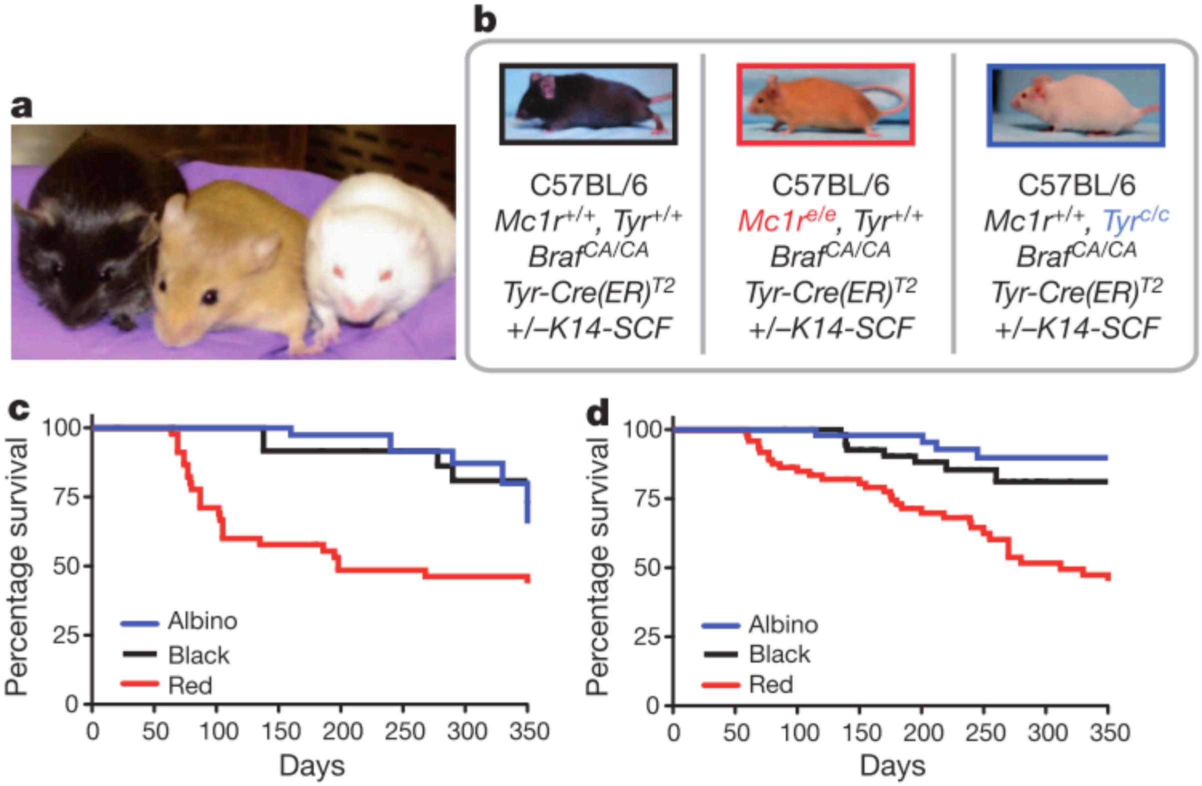

Figure 4.1.4: In the absence of ultraviolet radiation, *BrafCA* "redhead" mice develop melanoma at a higher rate than black and albino *BrafCA* mice. **A**: C57BL/6 variant mice containing the *K14-SCF* transgene exhibit distinctive dermal phenotypes. From left to right: black (wild type), red ($Mc1r^{e/e}$) and albino ($Tyr^{c/c}$). **B**: The genotype of animals used for experimental studies. **C**: Kaplan-Meier survival curves for pigmentation variants not carrying the $K14 - SCF$ transgene ($n_{\text{black}} = 28$, $n_{\text{red}} = 40$, $n_{\text{albino}} = 48$). $P_{\text{black-albino}} = 0.250$, $P_{\text{black-red}} = 0.003$, $P_{\text{albino-red}} = 0.003$. **D**: Survival curves of pigmentation variants carrying the *K14-SCF* transgene, that is, epidermal melanocytes ($n_{\text{black}} = 49$, $n_{\text{red}} = 77$, $n_{\text{albino}} = 41$). $P_{\text{black-albino}} = 0.103$, $P_{\text{black-red}} = 0.009$, $P_{\text{albino-red}}, < 0.0001$. Figure and modified caption reproduced from [163].

The results of Mitra *et al.* provide compelling evidence to support a novel paradigm in melanoma research, namely, that melanomas can originate in pheomelanin-rich lesions even in the complete absence of UV light exposure. Mitra *et al.* also remark that tumors from both redhead and albino mice (*i.e.*, rodents that lack eumelanin) are amelanotic and/or difficult to visualize with white light contrast or with the naked eye, making both laboratory study of their oncogenic progression in mouse models as well as clinical monitoring and diagnosis in redheads a challenging problem.

[163] This observation is consistent with the fact that although redheads suffer from the highest melanoma rate of all skin types, they exhibit the fewest visible nevi. [159, 170] Taken together, these findings support a hypothesis in which redheads develop "invisible" nevi through oncogenic mutation (*e.g.*, $BRAF^{V600E}$ mutation), with or without exposure to UV light; although a fraction of these invisible nevi ultimately progress to frank tumors, their chemical composition renders them difficult or impossible to detect using conventional clinical or biomedical methods. This creates an unmet and compelling need for the development of methods to visualize and monitor pheomelanin-rich nevi in redhead animal models and individuals.

4.1.2 Non-linear optical approaches to molecular imaging of melanins

From the optical imaging perspective, *in vivo* monitoring of pheomelanin is a challenging task. As a poorly soluble, amorphous aggregate with variable physical and chemical properties, pheomelanin is an extremely poor emitter, making fluorescence-based imaging extraordinarily difficult. [171] Pheomelanin also demonstrates a broad and non-specific absorption profile, making absorption-based techniques such as single-photon absorption or photoacoustic tomography nonspecific.[172] Furthermore, absorption techniques typically require a linear detection geometry wherein light passes through a sample and is collected on the other side; this constraint renders such techniques poorly suited to use on *in vivo* targets, where these geometries are cumbersome or impossible. The above problems are additionally aggravated by the fact that melanins are notoriously difficult to extract, isolate, purify, and/or synthesize *in vitro* and *ex vivo*. [154]

In contrast, in recent years there has been exploration of non-linear approaches to melanin imaging, as well as considerable technical advances in the development of non-linear imaging techniques suitable for use with melanins. [173] Among the more compelling bodies of work comes from the laboratory of Warren S. Warren, which recently demonstrated molecule-specific, quantitative, *in vivo* imaging of both eumelanin and pheomelanin using pump-probe microscopy. [174–176] In this technique, an ultrafast laser "pump" pulse is incident upon a chromophore, resulting in the absorption of the laser pulse and promotion of the chromophore to an electronically excited state. After a brief delay (generally picoseconds or femtoseconds), a second ultrafast laser pulse, usually centered at a different wavelength, is incident upon the same sample; this "probe" pulse interrogates the excited state properties of the sample and can be used to study processes such as excited state absorption, ground state depletion, and stimulated emission. [173] Although transient absorption spectroscopy experiments have been conducted on melanins since 2001 and earlier, Warren Warren and colleagues employed the use of lock-in amplification as part of a rapid, highly sensitive detection scheme, thereby facilitating the use of laser scanning and the deployment of the pump-probe approach as a *microscopy* technique capable of imaging melanins against a dermal background. [174–184] Using this technique or variants thereof, Warren Warren's laboratory has performed ratiometric imaging of eumelanin and pheomelanin in skin phantoms, melanoma cell lines, mouse melanoma models, hematoxylin and eosin-stained histologic slides, and thin patient-derived tissue slices. [174, 176, 184, 185]

While promising, the melanin pump-probe microscopy techniques described above suffer from several practical drawbacks. First, the lock-in amplifier-based detection technique, which involves acousto- or electro-optic modulation of the envelope of at least one pulsed source, is complex and difficult to implement, requiring specialized instrumentation as well as considerable expertise. Second, while the group's data unambiguously demonstrate the ability to empirically differentiate eumelanin from pheomelanin by virtue of their respective excited state properties, it remains unclear what those excited state properties are, to which physical processes they correspond, and how variable they will be across variegated chemical environments; furthermore, as presently described, the ability to perform differential molecular imaging requires precise physical translation of a mirror to adjust the interpulse delay time, making quantitative molecular measurements tedious. Third, successful *in vivo* imaging requires the use of so-called epi-mode detection schemes, in which the optical signal being measured is collected back trough the microscope objective; this is in contrast to transmission-mode imaging, in which the signal of interest is collected through separate optics on the distal side of the sample. Although Fu *et al.* as well as Matthews *et al.* demonstrate that epi-mode pump-probe imaging is possible, the power levels presently required to enable this approach (15-25 mW) will require careful evaluation to ensure that the imaging experiment itself does not result in cytotoxicity or carcinogenicity. [184, 185] Fourth, Matthews *et al.* presently report typical *in vivo* imaging times of 17 seconds, a speed that is impractical for longitudinal monitoring and even routine imaging in most animal models where speeds up to video rate (30 frames/second) are preferred. [185]

An alternative modality that is potentially capable of generating pheomelanin contrast is Raman spectroscopy/microscopy. Raman spectroscopy is based off the phenomenon of Raman scattering, first observed by C.V. Raman in 1928, in which light incident upon a molecule is inelastically scattered, resulting in a red- or blue-shifted photon; the energy level difference between the incident and scattered photon corresponds to the energy gap between the molecule's initial and final rotational-vibrational energy levels. [186] (The molecular underpinnings of the Raman phenomenon will be described in greater depth later in this Section.) Because these energy levels are often characteristic of a given molecule, Raman spectroscopy is frequently used for vibrational analysis and/or spectroscopic characterization of an analyte, often in conjunction with the complementary technique of infrared spectroscopy.

Although curiously few studies analyzing the Raman properties of melanins have been conducted, several recent works demonstrate not only that melanins exhibit characteristic Raman peaks, but also that eumelanin and pheomelanin differ in their spectral properties, a fact putatively attributable to the differences in the molecular characteristics of their constituent subunits, including the presence of sulfur in pheomelanin's benzothiazine and benzothiazole-containing intermediates. In 2004, Huang *et al.* reported the first Raman spectrum collected *in vivo* from human melanocytes and show that it contains characteristic peaks at 1380 cm^{-1} and 1580 cm^{-1}; they corroborate this data with reference spectra acquired from eumelanin-rich *Sepia* melanin, although they make no effort to account or control for different spectral properties of pheomelanin and eumelanin during any stage of the study. [187] More recently, Galván *et al.* investigated the Raman properties of both synthetic and avian pheomelanin and determined that they possess a distinctive spectrum from eulmelanin with peaks at 1150, 1490 and 2000 cm^{-1}. [188] In another study, Galván *et al.* confirm the existence of the pheomelanin peaks in a different avian-derived sample and go on to compare them to spectra obtained from eumelanin contained within the same sample, showing that the pigments' differential spectral properties can be used to quantify each pigment in the presence of the other (Figure 4.1.5). [189]

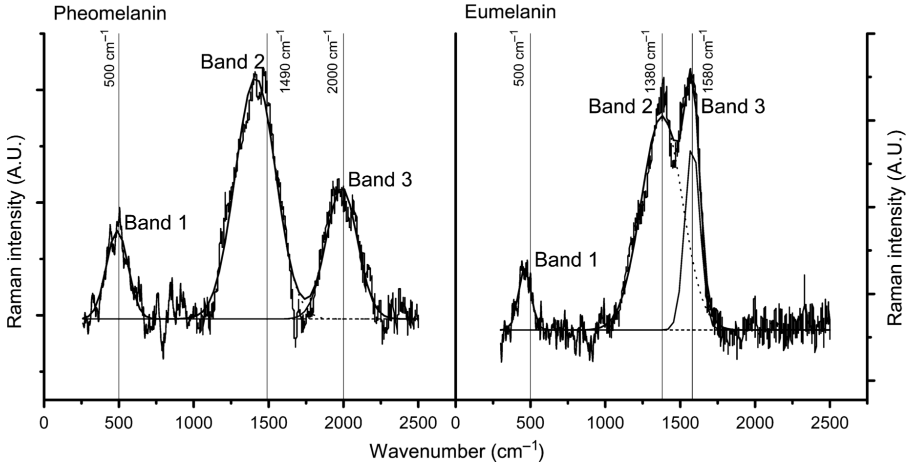

Figure 4.1.5: Raman spectra of pheomelanin and eumelanin isolated from red-legged partridge feathers, showing the characteristic peaks described above as well as the results of Gaussian curve-fitting study. Reproduced from [189]

While the presence of a detectable Raman peak is of course necessary to be able to differentiate pheomelanin from an amelanotic dermal background, it is not sufficient; other, non-pheomelanin molecules must additionally *not* exhibit Raman peaks within the same region to achieve specificity and functional optical contrast. In general, most biological samples possess Raman spectra with similar sets of major peaks, due in part to the ubiquitous nature of biomolecules such as DNA and of moieties such as amide bonds and C-H bonds (Figure 4.1.6). [1] Whereas the region between 600 and 1800 cm^{-1} is especially dense, no peaks are present at 2000 cm^{-1}, where the pheomelanin peak is known to occur. Taken together, these data suggest that Raman spectroscopy possesses the specificity necessary to differentiate pheomelanin from the background of other skin components, and may even be able to differentiate pheomelanin from eumelanin as well.

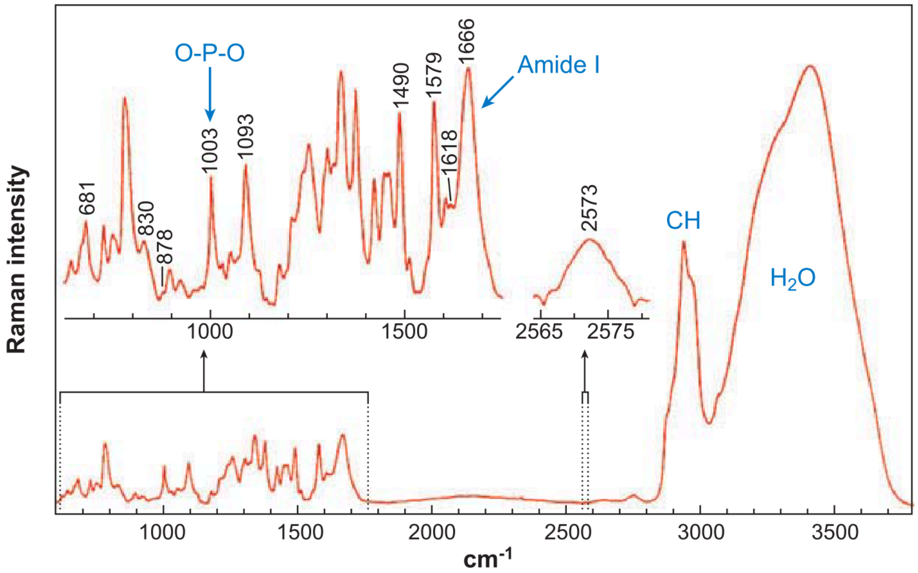

Figure 4.1.6: Raman spectra of a typical biological sample, in this case the P22 virus. Note the presence of peaks corresponding to common biomolecules, as well as the absence of peaks between 1800 and 2700 cm^{-1}. Reproduced from [1]

In principle, Raman spectroscopy could be turned into an imaging tool suitable for use on pheomelanin through use of appropriate laser source and filter selection. Unfortunately, Raman spectroscopy suffers from substantial drawbacks that hamper its utility as a microscopy platform. First and foremost, the Raman effect is an extremely weak phenomenon, with typical photon conversion efficiencies of 10^{-18} or lower. [1] This results in excessively long acquisition times (often 100 ms to 1 s per pixel) and requires that the sample be exposed to high laser powers, resulting in photodamage. [1] Thus, in practical terms, Raman microscopy would be difficult or impossible to implement for long-term pheomelanin monitoring *in vivo*.

A considerable amount of work has gone into development of viable alternatives that exploit the potential of Raman scatter as means of generating label-free, molecular contrast. Among these alternatives, which include surface-enhanced Raman scattering (SERS) and stimulated Raman scattering, coherent anti-Stokes Raman scattering (CARS) microscopy is among the most widely employed and highly developed. Fundamentally, CARS is a four-wave mixing process involving two source beams, a pump beam ω_p and a Stokes beam ω_s. When the difference $\omega_p - \omega_s$ matches the frequency of a Raman-active vibration within the molecule of interest, the Raman oscillators are coherently driven by the "beat" frequency of the combined optical fields; when an additional pump photon ω_p is scattered off this microscopically oscillating polarization, an anti-Stokes photon at the frequency $\omega_{as} = 2\omega_p - \omega_s$ is generated (Figure 4.1.7). [1] As a dual-color, non-linear microscopy technique, CARS has several advantages over Raman, including inherent 3D sectioning ability, blue-shifted emission relative to the laser sources (allowing for straightforward imaging using traditional microscopy filters), and most importantly log-order enhanced sensitivity compared to spontaneous Raman, enabling *in vivo* label-free microscopy at up to video rate. [1, 190]

Although CARS was first described by the Ford Motor Company in 1965, it was not used as a microscopy contrast mechanism until 1982, after which it was not further explored until 1999. [1, 191–193] Since then, CARS microscopy has been used to image a variety of targets, both biological and non-biological. By far the most prominent use of CARS has been label-free lipid imaging, *in vitro*, *ex vivo*, and *in vivo*. Recall from Figure 4.1.6 that there exists a prominent vibrational band at 2845 cm^{-1}; this corresponds to the CH_2 vibrational symmetric stretching frequency and is abundant in saturated and unsaturated lipids as well as fatty acids. [1] Vibrational imaging of lipids has been performed to monitor lipid metabolism in adipocytes, observe nerve bundle structure, function, pathology, and regeneration, monitor brain tissue, observe dermal drug delivery, quantify molecular agents in human hair, and study the mechanism of dermatological therapies including cryotherapy for fat loss, among many other applications. [1, 194–200] For further review of both biomedical and material applications of CARS, interested readers are encouraged to review the excellent review by Evans and Xie. [1]

After a brief introduction to the theory of CARS spectroscopy and microscopy, this chapter will discuss preliminary data from an ongoing project that demonstrates proof-of-concept that CARS microscopy can be used for label-free imaging monitoring of pheomelanin, both *in vitro* and in *ex vivo* cellular isolates from redhead mice. This opens up the exciting possibility that CARS microscopy could ultimately be used *in vivo* on live animals to monitor nevus formation and/or carcinogenesis in redheads.

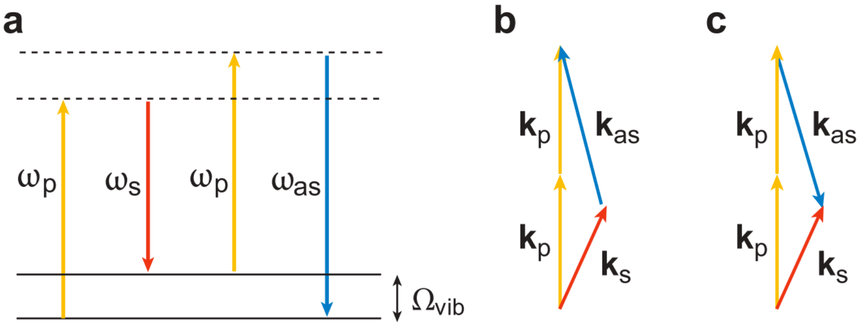

Figure 4.1.7: A: Diagrammatic representation of the CARS four-wave mixing process. **B,C**: Diagrammatic representation of the phase-matching condition for trans- and epi-detection, respectively. Reproduced from [1]

FUNDAMENTALS OF RAMAN SCATTERING

In order to better understand CARS, it is necessary to include a brief mechanistic discussion of Raman scattering. In broad terms, Raman scattering occurs when light incident on a molecule is inelastically scattered; this involves transient promotion of the molecule to a "virtual" state from which it decays into a distribution of vibrational states associated within the manifold of the molecule's ground electronic state. We will define this more rigorously using a classical explanation of the Raman phenomenon and use it to explain both its Stokes and anti-stokes components.

Consider the interaction of a molecule with an electric field $\vec{E}$, resulting in an induced dipole moment $\vec{\mu}$:

$$\vec{\mu} = \tilde{\alpha}\vec{E} \tag{4.1}$$

Where $\tilde{\alpha}$ is the molecular polarizability tensor, a property of the molecule that describes the ability of the driving electric field to interact with the electron density of the molecule and transiently drive it out of equilibrium. The real part of the complex field $\vec{E}$ can be described as follows:

$$\vec{E} = \vec{E}_0 \cos \omega_0 t \tag{4.2}$$

(Although it is important to recall that $\vec{E}$ and $\vec{\mu}$ are vectors and $\tilde{\alpha}$ is a third-rank tensor, this formalism is unnecessary for this description; vector notation will hereafter be dropped.)The polarizability α is not time-invariant; rather, it varies as a function of nuclear motion within the molecule, as the molecule's electrons adiabatically adjust to minimize the system's instantaneous energy. Thus, α is a function of the set of normal modes Q, where Q_k describes the k^{th} normal mode of the molecule at frequency ω_k. Rewriting α as a Taylor series yields:

$$\alpha = \alpha(Q) = \alpha_0 + \sum_k \left(\frac{\delta\alpha}{\delta Q_k}\right)_0 Q_k + \cdots \tag{4.3}$$

Because the normal modes are harmonic, Q_k can be written as:

$$Q_k = Q_{k0} \cos \omega_k t \tag{4.4}$$

Using this result in Eq. 4.3 and plugging into Eq. 4.1 gives the following result:

$$\mu(t) = \alpha_0 E_0 \cos \omega_0 t + \frac{1}{2} Q_{k0} E_0 \sum_k \left(\frac{\delta\alpha}{\delta Q_k}\right)_0 [\cos(\omega_0 - \omega_k)t + cos(\omega_0 + \omega_k)t] \tag{4.5}$$

Importantly, Eq. 4.5 contains three different frequency terms. The first term oscillates at ω_0, the frequency of the driving electric field; this gives rise to elastic Rayleigh scattering, a property of all molecular systems. The second and third terms oscillate at $\omega_0 - \omega_k$ and $\omega_0 + \omega_k$, giving rise to Stokes scattering and anti-Stokes scattering, respectively. By definition, Stokes scattering is redshifted with respect to the driving field, whereas anti-Stokes is blue-shifted. Although both sets provide equivalent information, the anti-Stokes is spectrum is usually omitted from a Raman spectrum as it is much less intense than the Stokes spectrum; this stems from the energetic favorability of Stokes transitions as predicted by Boltzmann statistics. Finally, note that for either Stokes or anti-Stokes scatter to occur, the molecule must possess a non-zero derivative of polarizability with respect to vibrational frequency (*i.e.,* $\left(\frac{\delta \alpha}{\delta Q_k}\right)_0 \neq 0$). This "selection rule" dictates which vibrational modes will be Raman active and also indicates the strength of the Raman-active mode. [186, 201, 202]

Introduction to coherent anti-stokes Raman scatter microscopy (CARS)

As described above and as illustrated in Figure 4.1.7, CARS is a four-wave mixing process that occurs in materials possessing inversion symmetry, wherein a Raman vibration $\omega_v = \omega_p - \omega_s$ is coherently driven by two photons ω_p and ω_s and mixed with another photon at ω_p to generate a fourth anti-Stokes photon at $\omega_{as} = 2\omega_p - \omega_s$. [203] Synonymously, this interaction stems from the generation of a third-order polarization $P^{(3)}(\omega_{as})$, the intensity of which is described by:

$$P^{(3)}(\omega_{as}) \propto \chi^{(3)} E_p^2 E_s^* \tag{4.6}$$

Where E_p and E_s are the pump and Stokes fields, respectively, and $\chi^{(3)}$ is the third order non-linear susceptibility of the material. Through solving the wave equation, the intensity of the anti-Stokes signal intensity can be defined as:

$$I_{as} \propto |\chi^{(3)}|^2 I_P^2 I_s \left(\frac{sin(\Delta kz/2)}{\Delta k/2}\right)^2 \tag{4.7}$$

Where z is the thickness of the sample and $k_i = 2\pi/\lambda_i$ is the wavevector. The term Δk refers to the wavevector mismatch, describes the velocity difference between the three frequencies, and is defined as $\Delta k = k_{as} - (2k_p - k_s)$. Importantly, the sinc function and therefore I_{AS} overall is maximized when Δk approaches zero. This is known as the phase-matching condition, and varies depending on the detection geometry; conveniently for laser-scanning microscopy, this term asymptotically approaches a maximum when using objectives with a high numerical aperture imaging objective (NA ≥ 0.2). Note that the CARS intensity is dependent not on $\chi^{(3)}$, which is linearly proportional to the concentration of the analyte, but instead to $|\chi^{(3)}|^2$. For this and other reasons (described below), the overall CARS signal is proportional not to the concentration of the Raman-active oscillator, but rather to its square. [1, 203] Note also that I_{as} is proportional to the product of the Stokes beam intensity and the square of the pump beam intensity; this introduces the practical requirements *a*) that the pump and Stokes beams tightly overlap in space (*e.g.*, at the focus of a high NA objective), and *b*) the pump and Stokes sources be capable of delivering high photon flux while not damaging the sample. The pump/Stokes spatial overlap requirement introduces a beneficial aspect of CARS microscopy, namely, that signal is only generated at the microscope focus, such that the CARS signal is inherently depth-resolved, as photon flux on either side of the laser focus is not sufficient to generate appreciable signal.

In practical terms, the *de facto* requirement for high laser flux at the focus results in the near-exclusive use of pulsed laser sources for modern CARS imaging experiments. Selection of optimum imaging sources for CARS requires careful balancing of multiple considerations and trade-offs; generally speaking, NIR pulsed sources of pico- or femto- second duration are preferred, although the choice of pico- *vs.* femto requires balancing several competing factors. (NIR sources are preferable for most tissue imaging applications, as they fall within the so-called "optical window" that falls approximately between 650 -1300 nm, wherein tissue-dependent laser absorption and scattering is reduced).

Importantly, $\chi^{(3)}$ has both resonant and non-resonant contributions, $\chi_R^{(3)}$ and χ_{NR}^3:

$$\chi^{(3)} = \chi_{NR}^{(3)} + \frac{\chi_R^{(3)}}{\Delta - i\Gamma} \tag{4.8}$$

Where Δ is the "detuning", or the difference $\Delta = \omega_p - \omega_s - \Omega_R$ and Ω_R is the center frequency of a homogeneously broadened Raman band with width Γ. The second term in Eq. 4.8 is a reflection of the fact that even when the difference $\omega_p - \omega_s$ is off resonance, the beams can still induce a macroscopic polarization ω_{as} due to the bulk electric properties of the material.[1, 203]. Therefore, as $I_{as} \propto |\chi^{(3)}|^2$:

$$I_{as}(\Delta) \propto |\chi_{NR}^{(3)}|^2 + |\chi_R^{(3)}(\Delta)|^2 + 2\chi_{NR}^{(3)}\Re\{\chi_R^{(3)}(\Delta)\} \tag{4.9}$$

Thus, the overall CARS signal intensity is the sum of a resonant, non-resonant, and mixed contribution, as can be seen in Figure 4.1.8. [1]

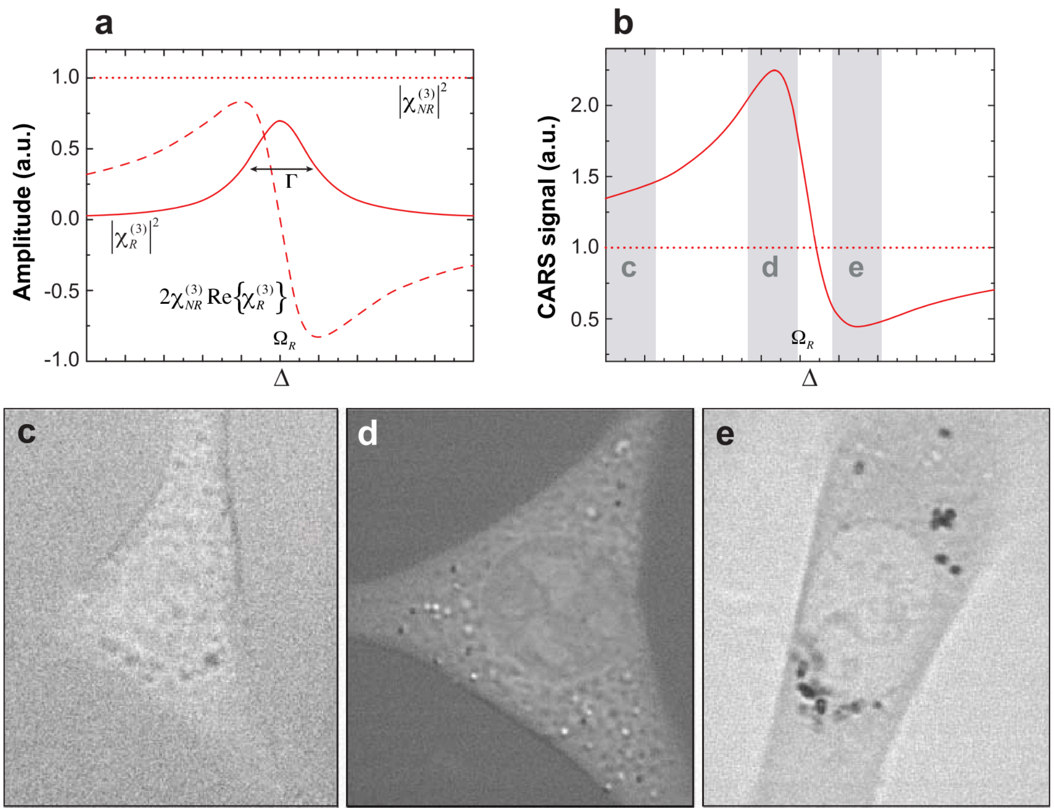

Figure 4.1.8: **A**: The three contributing terms to the CARS signal, illustratively plotted as a function of the Raman detuning Ω_R. Note the resonance-independent contribution $|\chi_{NR}^{(3)}|^2$ and the biphasic line shape of the the mixed term $2\chi_{NR}^{(3)}\Re\{\chi_R^{(3)}(\Delta)\}$. **B**: The summed CARS signal (solid line) and the constant non-linear background (dashed line). **C-E**: Forward-propagating CARS images acquired in the corresponding highlighted regions of the CARS spectrum found in *b*. **C** shows primarily non-resonant background, **D** shows an image acquired at 2845 cm^{-1}, the optimum wavelength for lipid imaging, and **E** shows an image acquired in the "blue dip" of the CH-stretching resonance (2950 cm^{-1}). Reproduced from [1]

Careful consideration of Eq. 4.9 and inspection of Figure 4.8 reveals the important conclusion that the presence of the non-resonant term $|\chi_{NR}^{(3)}|^2$and the mixed term $2\chi_{NR}^{(3)}\Re\{\chi_R^{(3)}(\Delta)\}$ make CARS spectra spectrally shifted from the Raman spectra from which they are physically derived. [1] This has the unfortunate consequence of rendering direct comparison of CARS spectra to existing Raman spectra difficult and increasing spectral congestion in crowded regions, although such overlap can be unmixed using computational techniques. [204] Nonetheless, because CARS is based on the presence of a Raman-active vibration, Raman spectra are frequently used as a starting reference point in determining optimum imaging system settings in CARS spectroscopy and microscopy.

It is important to note that although CARS is a four-wave mixing process, it is only one of many possible four-wave mixing processes that may be relevant in this imaging scenario (Figure 4.1.9). For example, if the transition that occurs when the ω_s photon mixes with the beating of $\omega_p - \omega_s$ occurs near an electronic energy level, then the four-wave mixing process can be electronically enhanced, even if $\omega_p - \omega_s$ is not near a Raman-active molecular vibration (Figure 4.1.9); [203] this may be particularly relevant for a molecule such as pheomelanin, a broad-spectrum absorber with a dense electronic structure. This process is known as electronically-enhanced four-wave mixing (EE-FWM). Processes such as CARS and EE-FWM are not necessarily mutually exclusive and can occur simultaneously within the same sample or system, making careful spectral measurements necessary in order to determine the physical nature of the phenomenon being observed. Whereas a signal originating primarily from CARS will vary approximately according to the linewidth of the corresponding Raman peak (within the limitations described above), a signal that originates primarily from EE-FWM will increase as ω_p approaches the electronic resonance in question. Given that pheomelanin's absorption generally increases in the blue, an EE-FWM-dominated signal would to a first approximation increase as the pump wavelength shifts blue (*i.e.*, as the detuning Δ grows more positive.)

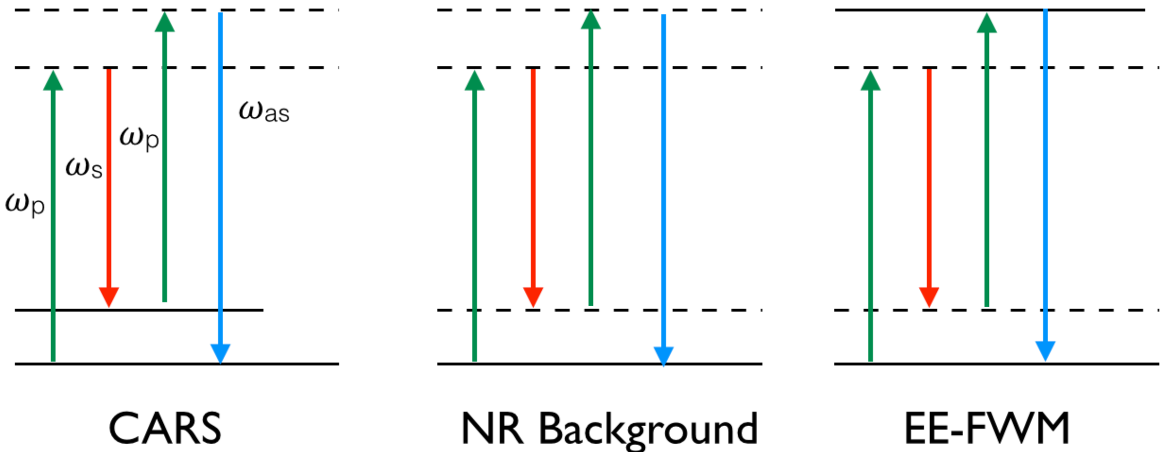

Figure 4.1.9: Jablonski diagram showing the three relevant four-wave mixing processes that can occur during the CARS imaging process. NR = non-resonant. Real electronic and vibrational energy states are depicted by long and short solid lines, respectively, whereas virtual states are represented by dashed lines. Note that this figure describes only a fraction of the many possible non-resonant four wave mixing processes that can occur.

4.2 RESULTS

As described in detail in Section 4.4, we began by constructing a femtosecond-pulsed, spectrally tunable CARS microscope with ω_s fixed at 1040 nm and ω_p tunable over the range 680-1300 nm. To demonstrate our new CARS system's capabilities, we collected an image of a sebaceous gland from an albino mouse ear, with the system tuned to the lipid vibrational stretch at 2845 cm^{-1} (Figure 4.2.1). Temporal detuning (*i.e.,* spatiotemporal separation of two-color pulse overlap) as well as blocking of either beam eliminated the signal, thus confirming that we were indeed observing CARS and not a one-color, multiphoton-induced process. (See Section 4.4). [2]

---

[2] Because lipid imaging was not the end goal of this work, we did not collect a CARS spectrum at 2845 cm^{-1}, as such spectra have been repeatedly published throughout the literature.

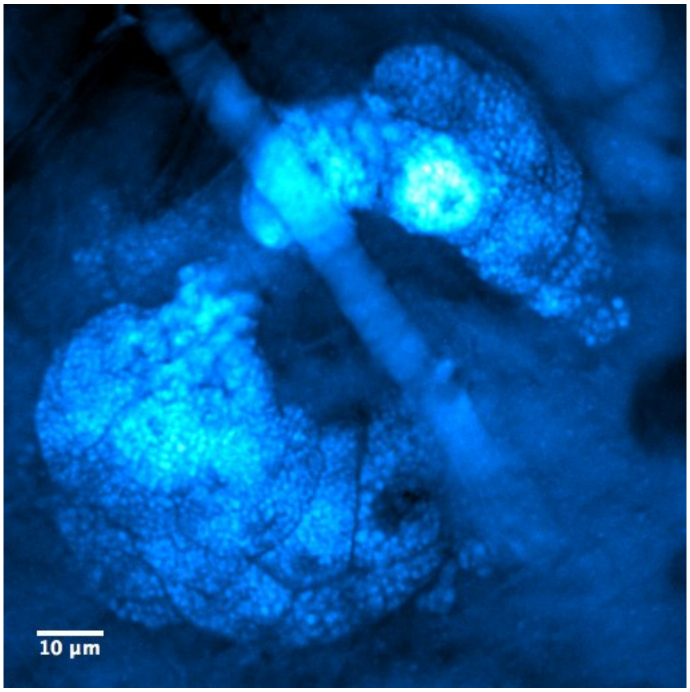

Figure 4.2.1: Projection of an epi-CARS image of a mouse sebaceous gland, acquired *ex vivo*. The system was tuned to the lipid vibrational band at 2845 cm^{-1}.

4.2.1 CARS IMAGING OF SYNTHETIC PHEOMELANIN

As a preliminary test of the ability of our imaging system to image pheomelanin, we synthesized pheomelanin using the mushroom tyrosinase protocol reported by D'Ischia *et al.* (see Section 4.4). [154] As expected, the synthetic protocol yielded a fluffy proteinacious macroscopic aggregate that was insoluble in aqueous solution; due to the highly absorptive nature of pheomelanin, attempts to image these gross aggregates at the 2000 cm^{-1} Raman band resulted in laser absorption and sample detonation (presumably through plasma formation). Reasoning that a microscopic emulsion might provide enough surface area per aggregate to dissipate heat and reduce thermal damage to the sample, we resuspended the pheomelanin in a microscopic emulsion of water and hexane, which allowed imaging without sample destruction. The results are presented in Figure 4.2.2. As before, temporal detuning as well as blocking of either beam eliminated the signal, demonstrating that the signal was generated through a four-wave mixing process (*i.e.*, CARS, EE-FWM, or a combination of the two).

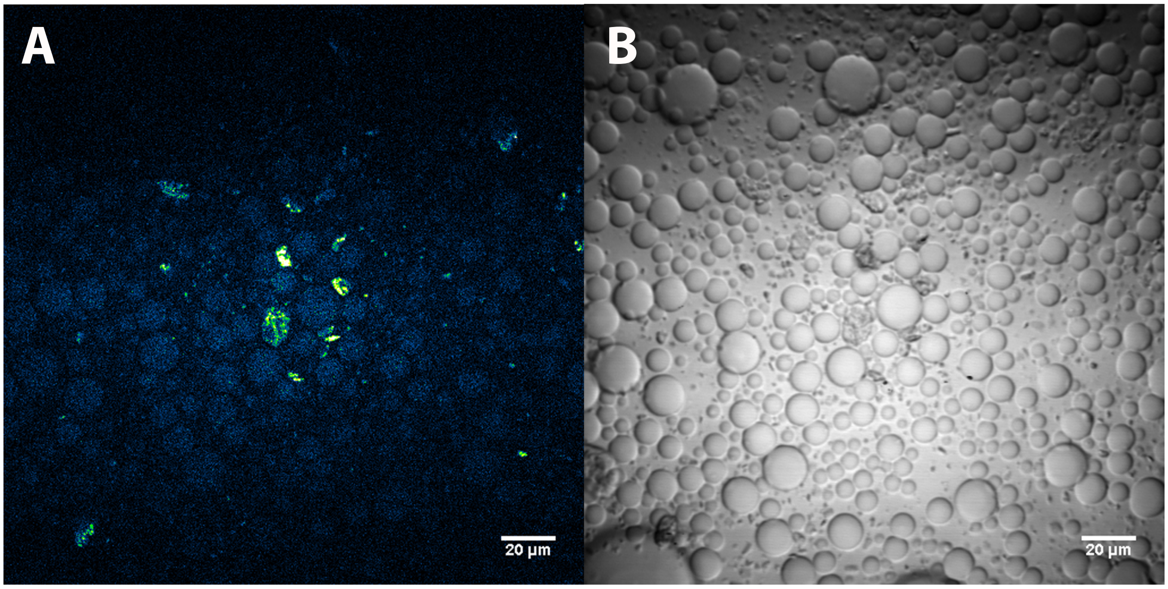

Figure 4.2.2: Synthetic pheomelanin emulsified in a mixture of hexanes and water. **A**: Epi-CARS image acquired at $\omega_p - \omega_s$ = 2000 cm^{-1}. ω_p = 861 nm, ω_s = 1040 nm. **B**: Transmission image acquired during CARS imaging. Pheomelanin can be visualized as small, insoluble aggregates near the center of the field of view; these aggregates correspond to the areas of signal intensity observed in **A**.

To better understand the physical nature of the generated signal, we collected a CARS spectrum. In such experiments, the presence of optical chromatic aberrations throughout the imaging system as well as chromatically-variable laser output power make it necessary to provide a constant reference for each spectral point to serve as an internal normalization/correction factor, as these factors can cause considerable variation within the CARS signal. We selected the non-resonant background from the glass microscope slide coverslip to serve this purpose, as it contains no Raman-active resonances, is independent of ω_p and ω_s, and can rapidly be gathered for each point through adjustment of the microscope focus. Figure 4.2.3 shows both the uncorrected CARS spectrum (Figure 4.2.3A) as well as the corrected CARS spectrum (Figure 4.2.3B). A comparison of Figure

4.2.3 to Figure 4.1.5 reveals the presence of nearly identical spectral features at 2000 cm^{-1}, consistent with the notion that our signal stems at least in part from CARS. To demonstrate that the pheomelanin signal is independent of the solvent or emulsion, we also collected a spectrum of an imaging region containing no pheomelanin, which showed a spectral response effectively identical to that of the non-resonant background (Figure 4.2.3C-D).

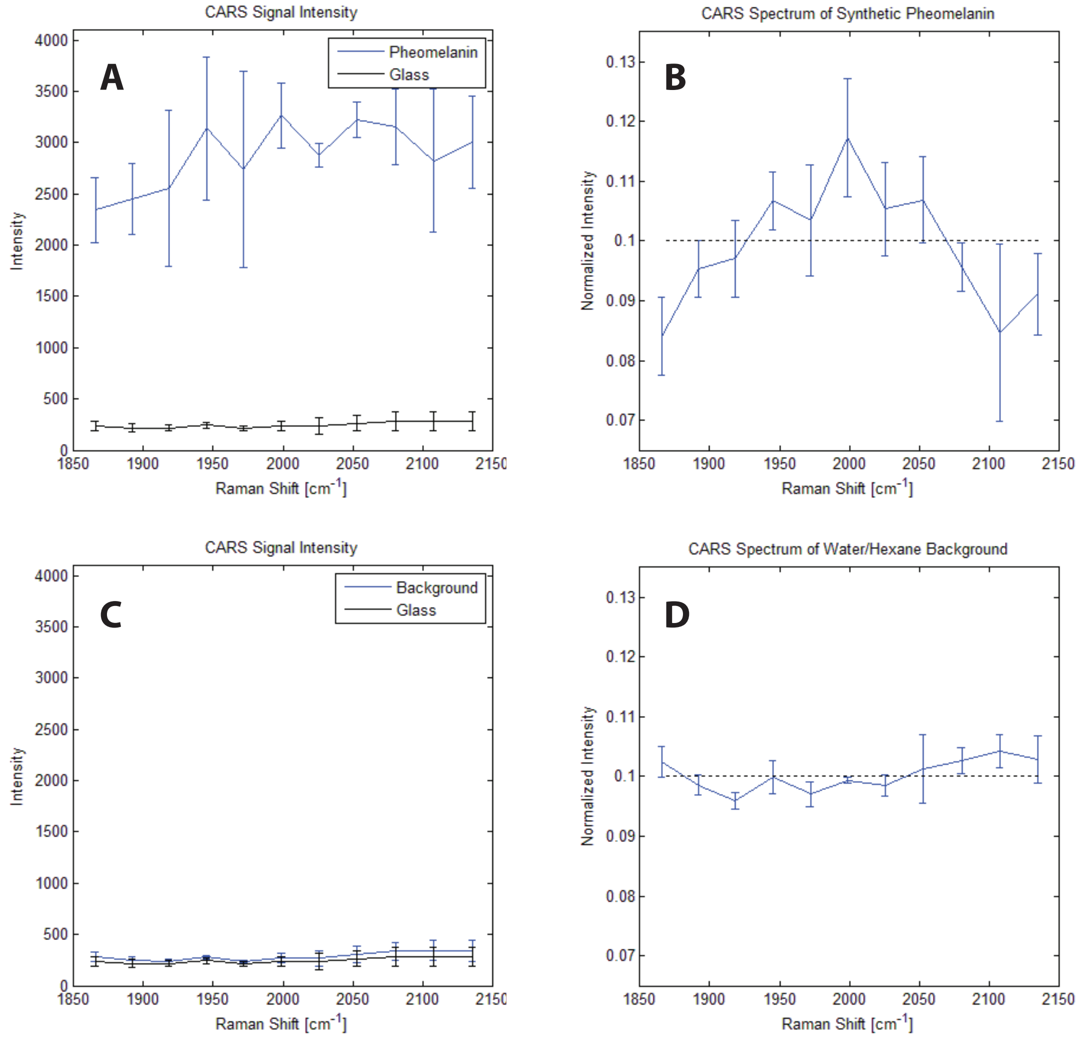

Figure 4.2.3: CARS spectrum of synthetic pheomelanin. **A**: Raw CARS signal intensity of synthetic pheomelanin ($n = 4$) and glass coverslip ($n = 2$). **B**: CARS spectrum of synthetic pheomelanin, corrected for wavelength-dependent variation and normalized by area under curve. Dotted line represents a theoretical flat normalized spectrum. **C**: Raw CARS signal intensity of water/hexane background and coverslip. **D**: CARS spectrum of water/hexane background, corrected for wavelength-dependent variation and normalized by area under curve. The spectrum closely matches the theoretical flat normalized spectrum, indicating that the signal from the sample background is independent of Raman shift. For details, see Section 4.4.

4.2.2 CARS imaging of putative melanocytes from redmice mice

To test the ability of our coherent Raman imaging system to image pheomelanin, we developed a protocol for isolation of putative melanocytes from redhead mouse pups and imaged redhead mouse melanocytes *ex vivo*. In addition to the redhead mice described above, the laboratory of our collaborator David Fisher has created a redhead Mc1r^{e}/^{e} mouse line, the melanocytes of which express the fluorescent marker tdTomato, thereby in principle rendering melanocytes easily identifiable via their fluorescence signal. To isolate dermal melanocytes, tdTomato/redhead mouse pups were sacrificed, their skin harvested, and the dermal cells separated, antibody stained, and FACS-sorted based on the ratio of tdTomato fluorescence to that of a FITC-tagged antibody targeting c-Kit, a known melanocyte surface marker (Section 4.4). [205] Cells were then fixed, slide-mounted, and imaged (Figure 4.2.4). Upon imaging, we noted that the observed signal was not symmetrically distributed throughout cells, but rather was apically polarized and seemed to exhibit a punctate/vesicular appearance, consistent with known developmental biology of stage III/IV melanosomes (Section 4.1.1).[3] Additionally, melanocytes isolated from albino mice did not exhibit these features, offering further evidence that the observed signal is melanin-specific (Figure 4.2.5). As before, the signal's intensity dropped dramatically with temporal detuning and blocking of either beam, demonstrating that the contrast source stems from a two-color, four-wave mixing process (Figure 4.2.5).

Notably, although the "melanocyte-specific" tdTomato expression (see footnote) in principle makes for straightforward isolation of cells, it also introduces a potential complication, as tdTomato is multiphoton excitable and will therefore exhibit fluorescence that may bleed through onto the CARS channel. Although the extent to which this contributes to the observed "CARS" signal can

---

[3] The observant reader will note that not all the cells imaged in Figure 4.2.5 exhibit signal upon CARS imaging; according to collaborators within the Fisher lab, this is because the promotor driving tdTomato expression is known to be "leaky," in that some other non-melanocytic cell types have been observed to express it. Thus, these cells are likely non-melanocytes and possess no melanin. (David Fisher, private communication).

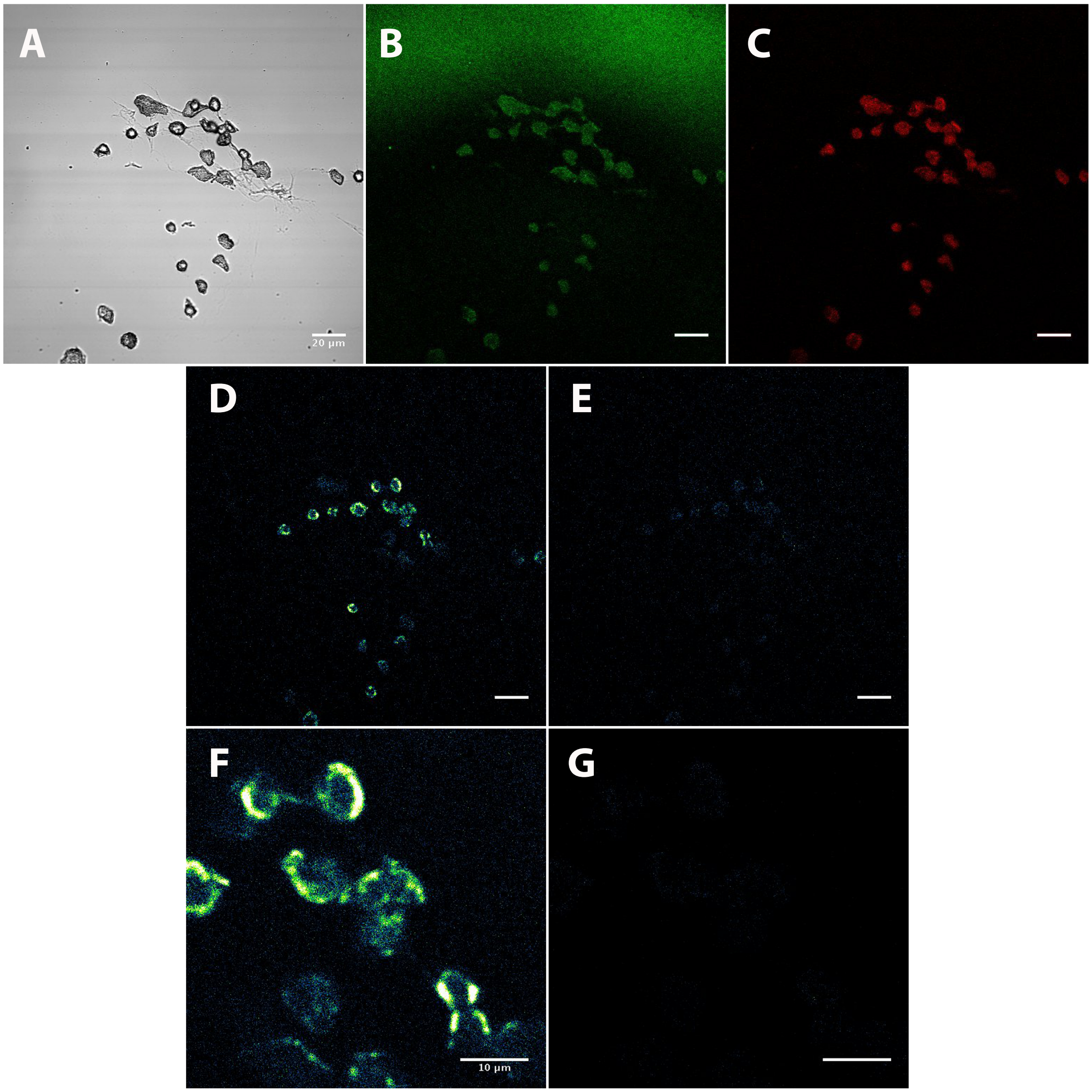

Figure 4.2.4: Melanocytes isolated from redhead C57BL/6 $Mc1r^{e/e}$ mice exhibit putative CARS signal at 2000 cm^{-1}. **A**: Transmission image of melanocytes. **B**: Confocal image of FITC c-Kit antibody staining. The diffuse signal at the top of the field is likely confocal reflectance. **C**: Confocal image of tdTomato fluorescence. **D**: False color epi-CARS image ($\omega_p - \omega_s = 2000\ \text{cm}^{-1}$) showing putative pheomelanin signal. **E**: Epi-CARS image after temporal detuning. No signal is present, suggesting that four-wave mixing is required to generate the signal. **F**: Zoomed epi-CARS image of melanocytes showing the intracellular distribution of signal intensity. Imaged is 5x zoomed relative to **D**. **G**: Zoomed image as in **F**, but with ω_p blocked.

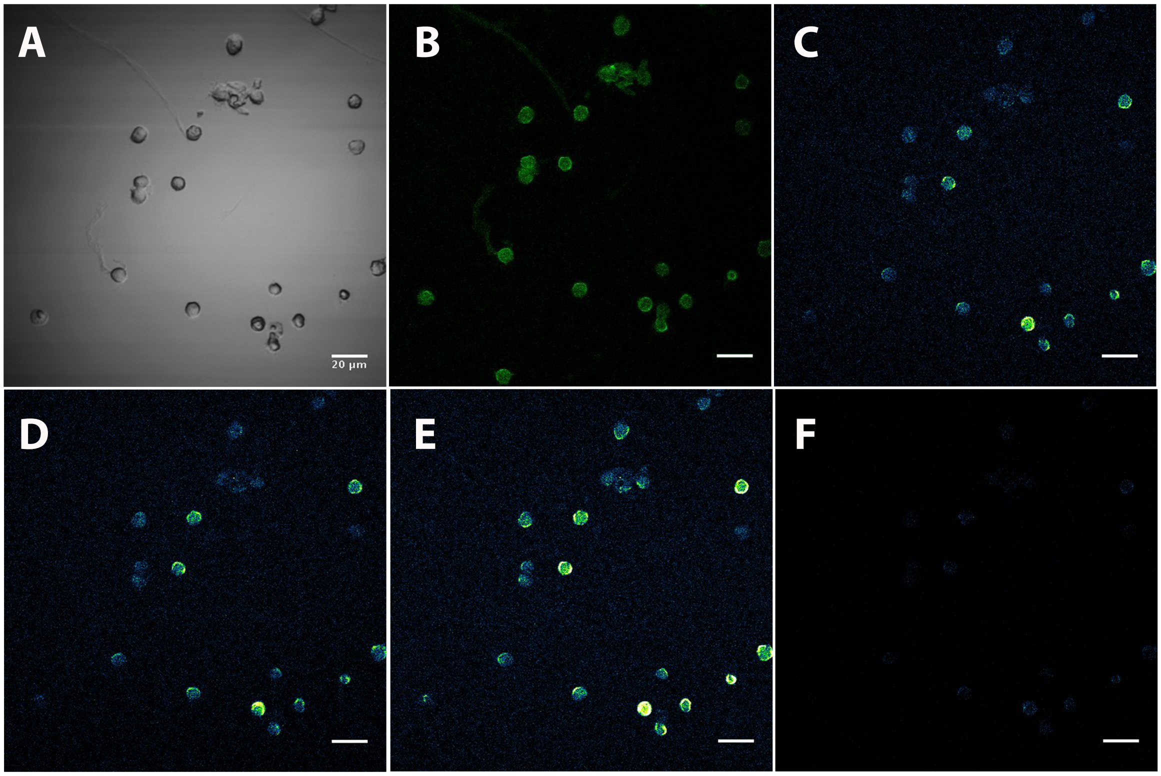

Figure 4.2.5: Melanocytes isolated from albino C57BL/6 *Tyr*$^{c/c}$ exhibit only multiphoton fluorescence when imaged with epi-CARS. **A**: Transmission image of melanocytes. **B**: Confocal image of tdTomato fluorescence. **C**: False color epi-CARS image ($\omega_p - \omega_s = 2000$ cm^{-1}). The observed signal is not dependent on a four-wave mixing process. **D**: Epi-CARS image after temporal detuning. The signal is unchanged relative to **c**, indicating that temporal pulse overlap is not required for its generation. **E**: Multiphoton imaging using ω_p only shows that ω_p is sufficient to generate signal and two colors are not required. **F**: Multiphoton imaging using ω_s only, demonstrating that ω_s does not contribute appreciably to signal generation.

be determined through temporal detuning and monochromatic excitation experiments (*cf.* Figure 4.2.5), if present, such signal cannot easily be distinguished from the CARS signal and will likely contribute to an elevated background, superimposed on the already ubiquitous non-resonant background characteristic of the CARS process. This should be taken into consideration when planning future CARS imaging studies on tdTomato-labeled melanocytes or during *in vivo* studies of tdTomato-expressing mice. Additionally, a comparison of Figures 4.2.4F and 4.2.5D shows that the tdTomato signal generated through multiphoton excitation differs considerably between the two cell samples tested; this is likely a reflection of varied tdTomato expression levels between the two lines.

4.2.3 Imaging of UACC 257 human melanoma cells and siRNA knock-down strategy

Although useful in providing early evidence of melanin-specific imaging in the appropriate biological context, the FACS-based, *ex vivo* experiments described in Section 4.2.2 suffered from low cell counts as well as large tdTomato multiphoton fluorescence contamination, making follow-up experiments challenging. We therefore considered an alternative approach involving siRNA knockdown of key genes in the melanin synthesis pathway in UACC 257 human melanoma cells.

As a melanotic human melanoma cell line, UACC 257 cells appear pigmented to the eye and under normal conditions synthesize a mixture of eumelanin and pheomelanin. [206, 207] In this molecular approach, siRNAs against key molecules important in the melanin synthesis pathway were used to bias cultures either towards or away from pheomelanin synthesis. Specifically, the transcription factor MITF is an upstream upregulator of MC1R, a receptor associated with increased eumelanin synthesis, whereas the transcription factor NNT upregulates the transcription of precursors required for pheomelanin synthesis.[4] [206] Thus, to a first approximation, siRNA against *MITF* should bias cells towards pheomelanin synthesis, whereas siRNAs against *NNT* should

---

[4] The function of NNT is an area of active investigation. This experiment was based on a communication with Elizabeth Roider, MD, a fellow in David Fisher's lab.

increase production of both pigments, with the potential to generate more eumelanin than pheomelanin. Finally, tyrosinase/TYR is common and necessary for both eumelanin and pheomelanin synthesis; treatment of cells with siRNAs against *TYR* should result in an overall decrease in melanin synthesis. [154]

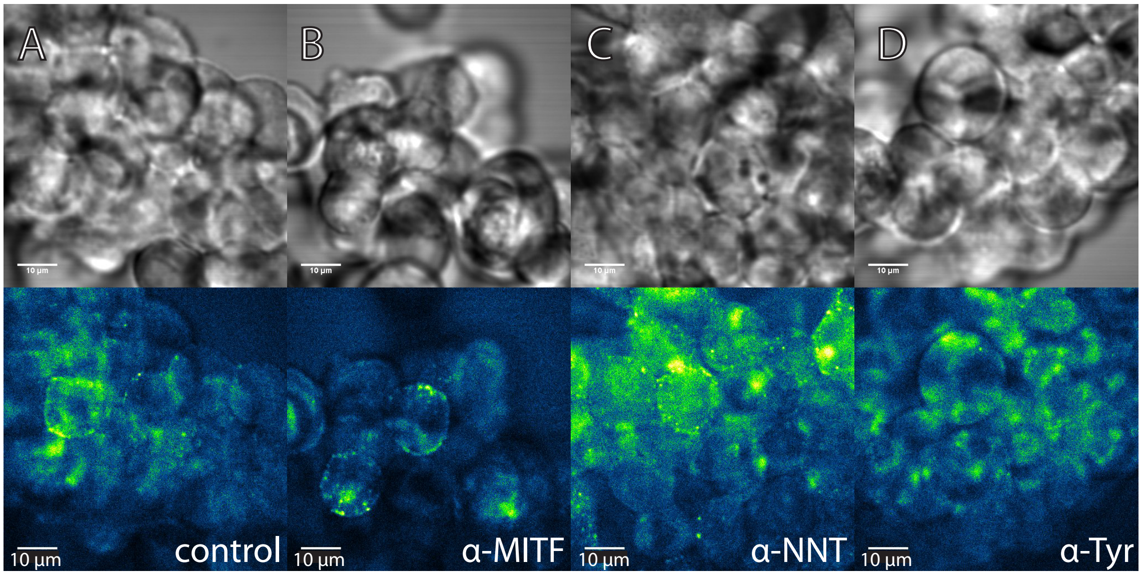

Figure 4.2.6: epi-CARS images of siRNA-treated human melanoma cells. The CARS system was tuned for imaging at 2,000 cm^{-1} (ω_p = 861 nm, ω_s = 1040 nm) to access pheomelanin-specific molecular vibrations. Bright, punctate regions putatively correspond to melanosomes. **A**: Cells treated with control fragment of siRNA do not exhibit changes in melanin production. **B,C**: *α*-MITF (B) and *α*-NNT (C) siRNA treatments bias cells towards pheomelanin and eumelanin production, respectively, resulting in enhanced peripheral distribution of punctate signal. **D**: Treatment with tyrosinase siRNA downregulates all melanin synthesis, as demonstrated through the absence of bright punctate regions in the cells' periphery.

Upon imaging, we observed that siRNA treatment resulted in pronounced differences in spatial localization and patterning of the CARS signal (Figure 4.2.6).Treatment with *α*-MITF siRNA resulted in an overall decrease in signal, but resulted in an increase in the number of punctate, peripheral subcellular signal that could be distinctly visualized relative to control. In contrast, *α*-NNT siRNA treatment resulted in an increase in the diffuse signal that lacked the precise spatial localization of that observered during *α*-MITF siRNA treatment. Most compellingly, *α*-TYR treatment resulted in complete elimination of the punctate signal, such that only a less intense, diffuse signal remained.

To verify these findings as well as to better understand the physical nature of the generated signal, the MITF and NNT siRNA knockdown experiments were repeated and epi-CARS spectra were collected (Figures 4.2.7 and 4.2.8). While the images acquired failed to demonstrate a clear trend, both samples again showed a clear, punctate signal pattern distal from the nucleus; furthermore, the CARS spectra collected under both conditions exhibit a broad spectral peak centered at 2000 cm^{-1}, consistent with both the reported Raman peak of pheomelanin as well as the CARS spectrum of synthetic pheomelanin shown in Figure4.2.3. [189]

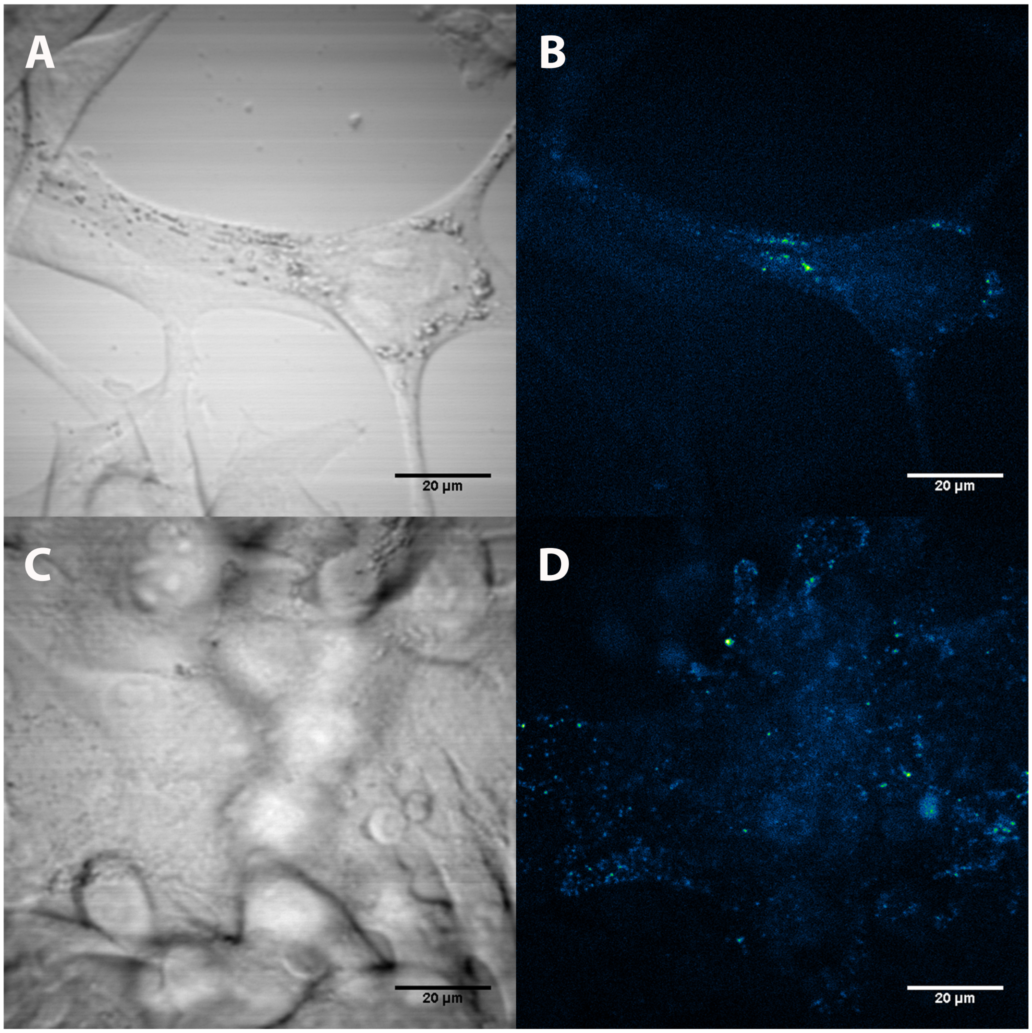

Figure 4.2.7: Epi-CARS imaging of siRNA-treated UACC-257 melanoma cells reveals punctate localization consistent with known melanosome biology. **A**: Transmission image of cells treated with *α*-MITF siRNA. **B**: Epi-CARS image of cells treated with *α*-MITF siRNA. **C**: Transmission image of cells treated with *α*-NNT siRNA. **D**: Epi-CARS image of cells treated with *α*-NNT siRNA.

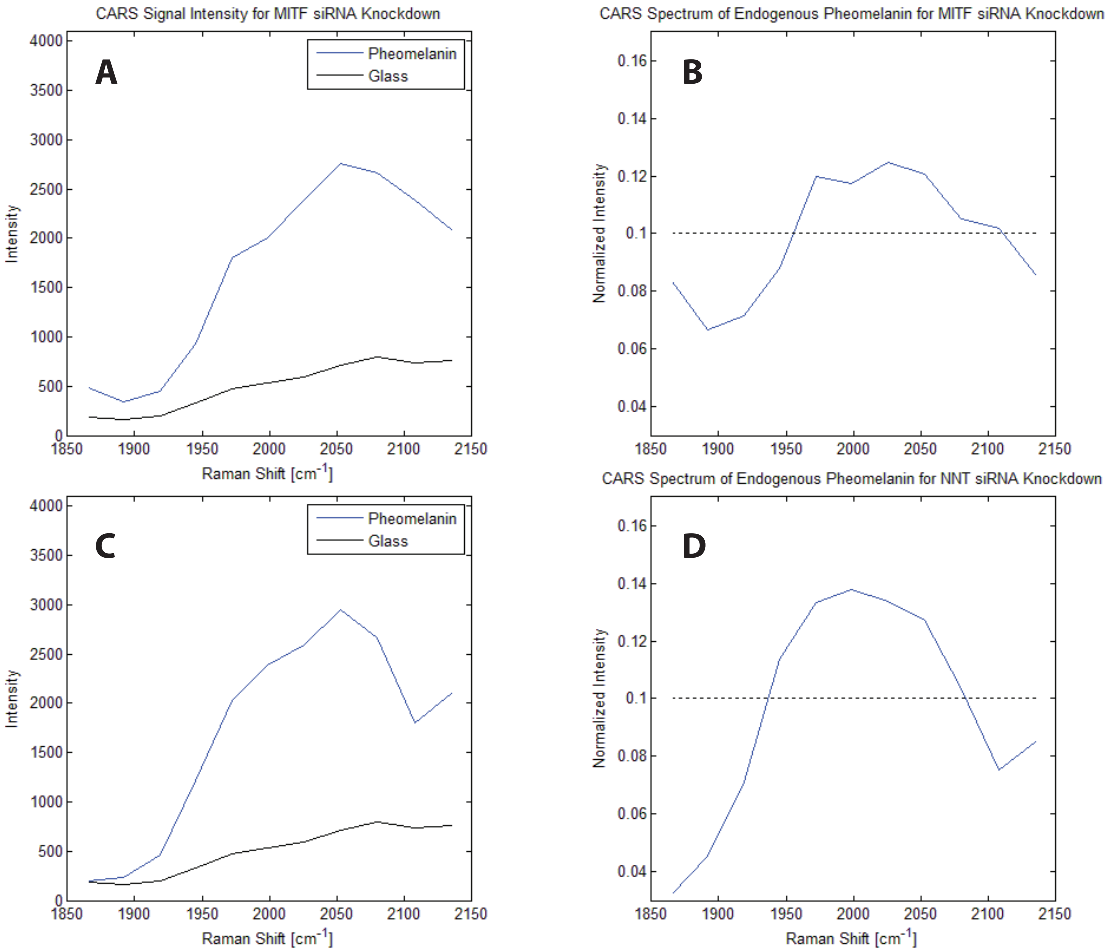

Figure 4.2.8: siRNA-treated UACC-257 cells exhibit CARS spectra characteristic of pheomelanin. **A**: Raw CARS signal intensity of endogenous pheomelanin in UACC-257 cells treated with α-MITF siRNA ($n = 1$) and glass coverslip ($n = 1$). **B**: CARS spectrum of endogenous pheomelanin in UACC-257 cells treated with α-MITF siRNA, corrected for wavelength-dependent variation and normalized by area under curve. Dotted line represents a theoretical flat normalized spectrum. **C**: Raw CARS signal intensity of endogenous pheomelanin in UACC-257 cells treated with α-NNT siRNA ($n = 1$) and glass coverslip ($n = 1$). **D**: CARS spectrum of endogenous pheomelanin in UACC-257 cells treated with α-NNT siRNA, corrected for wavelength-dependent variation and normalized by area under curve. This experiment was conducted using a preliminary version of the CARS spectral acquisition protocol; only 1 spectrum was acquired for each siRNA knockdown condition/glass coverslip pair. The same CARS signal intensity values for glass are used in **A** and **B** as in **C** and **D**.

Although it is difficult to draw many definitive conclusions from these preliminary experiments, the results demonstrate that molecular modulation of factors known to affect the eumelanin/pheomelanin synthetic balance result in observable differences in CARS signal localization. In particular, the observation of a punctate CARS intensity pattern following α-MITF siRNA treatment combined with the complete absence of punctate CARS signal following α-TYR siRNA treatment suggests that the punctate, peripheral regions of intensity may correspond to pheomelanin-rich melanosomal structures. Additionally, the molecular sources of the diffuse versus punctate signals remain unclear and are an area of active investigation. More careful studies, some of which are described below, are necessary to confirm these observations.

4.3 DISCUSSION AND FUTURE WORK

The work presented in this chapter opens up the exciting possibility that it may be possible to image pheomelanin *in vitro*, *ex vivo*, and *in vivo* using CARS, EE-FWM, or a combination thereof. We demonstrate proof-of-concept that both synthetic pheomelanin and cellular pheomelanin imaged *in situ* generate a CARS spectrum that is consistent with previously reported pheomelanin spectra from the Raman literature; we additionally show that this signal and its cellular localization can be modulated using molecular interventions known to alter pheomelanin synthesis pathways, thereby demonstrating that this CARS approach can be used to monitor dynamic cellular processes that are spectrally consistent with pheomelanin transport. Taken together, our data offer compelling evidence that CARS microscopy could be a useful tool in studying nevus formation as well as melanoma carcinogenesis in redheads.

While promising, the data are preliminary and they leave several fundamental physical questions unanswered. Although the presence of a pronounced peak within the CARS spectrum at 2000 cm^{-1} strongly suggests that CARS is the dominant mechanism of contrast, the data do not exclude the possibility that EE-FWM is contributing at a lower level. As discussed in Section 4.1.2, *ceteris paribus* the presence of EE-FWM in pheomelanin would lead to an increase in signal as ω_p shifts further into the blue, or equivalently as the Raman detuning Δ becomes more positive. This stands in contrast to a spectrum derived purely from CARS, wherein positive Δ leads to a *drop* in signal due to the presence of the mixed non-linear susceptibility term $2\chi^{(3)}_{NR}\Re\{\chi^{(3)}_{R}(\Delta)\}$ in the CARS intensity expression (Figure 4.1.8). Thus, the effects of positive Δ are opposed for EE-FWM and CARS. Interestingly, inspection of the pheomelanin CARS spectra shown in Figures 4.2.3 and 4.2.8 reveals that it does not exhibit negative deviation as Δ increases beyond 2000 cm^{-1}, but rather approaches a baseline level similar to or higher than that observed for negative Δ on the other side of the peak. This observation is consistent with a contrast mechanism dominated by CARS but with an EE-FWM signal that increases with positive Δ, offsetting what would otherwise be a drop in contrast. (It should also be noted, however, that the Raman tuning range Δ explored during these experiments is small enough that the expected positive change in EE-FWM may effectively approach zero, making the EE-FWM contribution flat across the wavelengths studied).

It is also interesting to consider the observation that both Figures 4.2.3 and 4.2.8 show a CARS spectrum that is approximately centered at 2000 cm^{-1} or slightly higher. This is also inconsistent with the theory described in Section 4.1.2, which predicts that the CARS peak should fall at a *negative* Δ/lower $\omega_p - \omega_s$ relative to the Raman spectra shown in Figure 4.1.5 and reference [189]. While the theory proposed in the previous paragraph could conceivably also explain a perceived spectral shift to higher wavenumbers (*i.e.*, an increasing EE-FWM signal to match a decreasing CARS signal), recall that pheomelanin is a heterogeneous biomolecule with poorly defined structure and microenvironment; it is therefore also possible that the Raman shift itself is different in the samples imaged, or that the Raman curve could be broadened relative to the samples tested by Galvàn *et al.* [189]. (Interestingly, if an approximately continuous distribution of pheomelanin macromolecular sizes were present, this would have a effect comparable to convolving the CARS spectrum of a given individual macromolecule with the distribution of all macromolecules, which would also reduce the $2\chi^{(3)}_{NR}\Re\{\chi^{(3)}_{R}(\Delta)\}$-induced drop in contrast described above.) One simple way to address this latter question would be to take a confocal Raman spectrum of both the synthetic pheomelanin and the *in situ* pheomelanin and compare them to the CARS spectrum. Although our laboratory had access to a Raman spectrometer, it operated at a wavelength too blue to be of use in this context, as background autofluorescence would easily overwhelm the faint Raman spectrum; a Raman spectrometer operating at or around 1000 nm would be ideal for this application.

Another important factor to consider, and one related to the questions described above, is whether the observed signal is unique to pheomelanin or whether it can also be generated by eumelanin. The absorption spectrum of eumelanin is similar to that of pheomelanin, in that both are broad spectrum absorbers with molar extinction coefficients that globally increase towards shorter wavelengths. [172] Furthermore, eumelanin possesses no Raman-active vibrations at 2000 cm^{-1}, and should therefore not exhibit any resonant CARS signal near the 2000 cm^{-1} wavenumber regime (Figure 4.1.5). [189] Thus, to a first approximation, if a four-wave mixing signal is observed from an eumelanin sample, it is likely EE-FWM and not CARS. While not definitive, this would also suggest by extension that a similar signal could be present in pheomelanin, given their similarities in electronic structure. More importantly, a finding of appreciable four-wave mixing signal in eumelanin would indicate that the signal at 2000 cm^{-1} is not specific for pheomelanin in non-redhead samples that are capable of synthesizing appreciable quantities of eumelanin (such as the UACC-257 cells imaged in Section 4.2). However, as redhead mice are genetically incapable of producing appreciable quantities of eumelanin, this finding would have little impact on CARS studies in this model system. The spectral properties of eumelanin described above could easily be determined through straightforward Raman and CARS spectroscopy experiments on commercially available eumelanin standards such as *Sepia* melanin.

As described in Section 4.1.1, the motivation for this work is to develop a straightforward method to image pheomelanin as a means to monitor nevus formation and melanoma carcinogenesis *in vivo* in a redhead mouse model. On the basis of pheomelanin's Raman spectrum, CARS was selected as the first imaging modality to be explored due to its relative ease of implementation versus more complex techniques like pump-probe microscopy as well as its superior imaging speed. [190]

However, there exist other Raman-based imaging modalities that, while more complex, would help to answer several of the questions posed above and potentially improve imaging outcomes. One such technique is Stimulated Raman Scattering (SRS) microscopy.[208–211] SRS, analogous to the well-described phenomenon of stimulated emission, is a two-color, non-parametric process whereby two laser sources ω_p and ω_s are tuned such that $\omega_p - \omega_s = \Omega_R$, where Ω_R is a Raman-active vibration of interest in the analyte. When this condition is met, amplification of the Raman phenomenon occurs through simultaneous induction of a Raman loss within ω_p and a Raman gain within ω_s.[5] [203] First described as a microscopy technique in 2008, SRS is capable of generating similar contrast to that generated by CARS, but benefits from numerous advantages, namely, elimination of the non-resonant background and a signal that is linearly proportional to analyte concentration.[208, 212] (Recall from Section 4.1.2 that the relationship between CARS signal strength and analyte concentration is not straightforward). Additionally, the detection schemes used for SRS are highly sensitive, and the non-parametric SRS signal is generated only through resonant processes; thus, neither non-resonant FWM nor tdTomato fluorescence will be detected, offering the ability to isolate the physical nature of the signal source. Unfortunately, the equipment required for SRS detection is expensive, and its operation is nuanced and complex; thus, we opted to begin our work with CARS. Nonetheless, we have recently begun to integrate SRS capability into our system, although substantial optimization remains necessary to achieve a signal-to-noise ratio suitable for biological imaging.

In addition to understanding the physical nature of the CARS signal, it is also important to conclusively demonstrate that it physically colocalizes with pheomelanin. One possible approach to demonstrating colocalization would be to histologically label pheomelanin within cells using staining or immunofluorescence, confocally image its subcellular localization, and then image the same cell with CARS. Unfortunately, pheomelanin is not a conserved epitope but rather a heterogeneous

---

[5] The attentive reader will again note that this condition is identical to that required for CARS; indeed, both phenomena occur simultaneously, but differ in the means they are detected.

aggregate for which no commercially available antibodies exist, and a comprehensive literature search revealed that most histochemical stains used for melanins react preferentially with eumelanin and not pheomelanin, making direct histological identification of pheomelanin challenging. However, as discussed in Section 4.1.1, pheomelanin is synthesized in stage III/IV melanosomes, which express characteristic and specific surface antigens. As our current understanding of melanosomal biology suggests that only stage III/IV melanosomes engage in pheomelanin synthesis, it might be sufficient to demonstrate that the pheomelanin CARS signal localizes to these structures. Two candidate melanosomal antigens that meet these criteria are Rab27a and Pmel 17, which are targeted by the antibodies α-Rab27a and HMB45, respectively. [157]

Finally, studies demonstrate that pheomelanin can be visualized with specificity using transmission electron microscopy (TEM) when samples are prepared using a uranyl acetate/osmium tetroxide staining procedure. [213] While sample preparation required for TEM imaging would render samples unable to be imaged using CARS, a comparison of TEM and CARS images acquired from similar samples would allow for a qualitative comparison of the localization and spatial distribution of the two signals; analogous results from both TEM and immunofluorescence would strengthen the case that the CARS signal colocalizes with known cellular depositories of pheomelanin.

4.4 Materials and methods

Note: all animal studies described herein were reviewed and approved by the Institutional Animal Care and Use Committee (IACUC) at the Massachusetts General Hospital. All animals received care in strict compliance with the 2011 *Guide for the Care and Use of Laboratory Animals* by the National Research Council and were maintained in a facility accredited by the Association for Assessment and Accreditation of Laboratory Animal Care International (AAALAC, Int.)

4.4.1 CONSTRUCTION OF THE CARS MICROSCOPE

The CARS microscope was built around an Olympus FV1000 confocal microscope, modified to accept an external pulsed laser source (Figure 4.4.1). For our laser source, we selected a Spectra-Physics InSight Deepsee with a pulse repetition rate of 80 MHz, pulse width of <120 fs, and dual outputs (1040 nm and 680-1300 nm tunable). The average output power varied as a function of wavelength but generally was in the range of 0.6- 1.8 W at the laser aperture. The 1040 nm output was used as the Stokes beam (ω_s), and the tunable output was used as the pump beam (ω_p). For lipid imaging experiments ($\Omega_R = 2845$ cm^{-1}), the pump beam was tuned to 803 nm, corresponding to a CARS emission at 654 nm. For pheomelanin imaging experiments ($\Omega_R = 2000$ cm^{-1}), the pump beam was tuned to 861 nm, corresponding to a CARS emission at 735 nm. A NIR-optimized Glan laser polarizer/$\lambda/2$-wave plate was placed after the output aperture of each of the two beam lines to adjust the beam output power. A 20 MHz NIR-optimized resonant electro-optic modulator (Thorlabs EO-AM-R-20-C2) was also included in the Stokes beam line in anticipation of later incorporation of simulated Raman scattering (SRS) microscopy modality, but was unused for any the experiments described above. The second Glan laser polarizer and $\lambda/4$ wave plate were included to correct for circular polarization imparted to the beam by the EOM, which is otherwise horizontally polarized; the presence of this optical elements does not otherwise affect the microscope's performance as a CARS imaging system.

Pulse temporal overlap was achieved through construction of a translatable delay stage; measurement of coarse overlap was attained using a photodiode and a 1 GHz oscilloscope, whereas measurement of fine overlap was achieved using an A.P.E. PulseCheck autocorrelator. A small 1:1 variable telescope was placed after the translation stage to compensate for chromatic aberrations leading to a mismatch of focal depth between the pump and Stokes beams. The beams were combined in a short-pass dichroic mirror and expanded approximately 4x before entering the FV1000.

CARS detection was performed at the FV1000's camera port. A short focal length lens was placed at the camera output, along with optical filters appropriate for the emission light of interest, to focus the non-descanned light onto the active area of a thermoelectrally-cooled Hamamatsu small-area PMT. For 2845 cm^{-1} lipid imaging, a Hamamatsu h7422PA-40 was used, whereas for 2000 cm^{-1} pheomelanin, a h7422PA-50 was used. Unless otherwise specified, all images were acquired using either the UPLSAPO 60XW objective or the UPLSAPO 40XW objective, both from Olympus. All images were acquired with power levels at or below 5 mW/beam, measured at the objective.

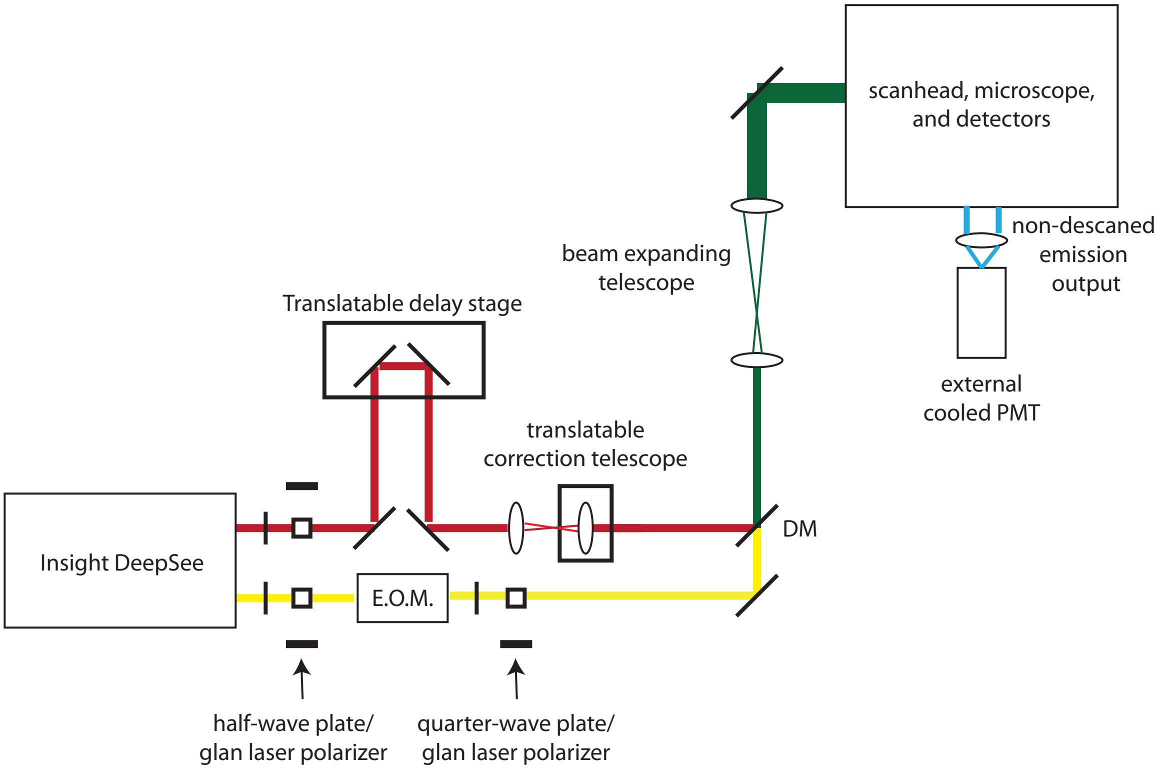

Figure 4.4.1: Schematic of the the CARS microscope used in all experiments. The EOM and the $\lambda/4$-wave plate/Glan laser polarizer pair were included in anticipation of future SRS incorporation and do not affect the system's CARS performance.

4.4.2 IMAGING OF MOUSE SEBACEOUS GLANDS

Imaging of sebaceous glands was performed on mouse ears, freshly acquired from anesthetized albino C57BL/6 mice. Ears were excised at the base, placed on PBS-soaked gauze, and hair was removed from the ears using commercially-available Nair™. In preparation for imaging, ears were placed on a microscope slide and covered with a #0 glass coverslip.

4.4.3 PHEOMELANIN SYNTHESIS AND IMAGING

Pheomelanin was synthesized as previously reported by D'Ischia *et al.* and lyophilized to yield a dense, brown aggregate. [154] The pheomelanin was used with no further analysis or purification.

To emulsify the pheomelanin, a small quantity (0.1 mg) was placed in a 2 mL microcentrifuge tube, to which 1 ml H_2O and 0.25 ml hexane were added and the mixture was sonicated for two cycles of three minutes each to generate an emulsion. Immediately afterward, the sample was aliquoted into a microscope slide prepared with a Secure-Seal™imaging spacer (Grace Biolabs) and covered with a glass coverslip. To prevent evaporation of hexane, the edges of the coverslip were sealed in nail polish.

4.4.4 ACQUISITION OF CARS SPECTRA

Wavelength adjustments on the Insight DeepSee were performed using the included software. Notably, the system includes a dispersion compensation module that, if left on, will alter the temporal overlap of the two beams; to overcome this problem, the dispersion compensation module was bypassed. After wavelength adjustment, the half-wave plate at the pump beam laser output and the variable telescope were adjusted to maintain a constant in-line laser power as needed, ensuring identical power delivery and optical properties across wavelengths.

The pump wavelength was varied from 871 nm to 851 nm at 2 nm increments, which corresponds to a CARS spectrum ranging from 1866 cm^{-1} to 2136 cm^{-1} in increments of roughly 27

cm^{-1}. For each new pump wavelength, the microscope focus was repositioned into the glass coverslip and an image was acquired; this represents the non-resonant background signal of the glass and does not vary as a function of pump wavelength. These non-resonant reference images serve as a basis over which the CARS images of the samples can be normalized for each given wavelength; this normalization compensates for any wavelength-related signal dependencies of the system, thus only highlighting variations related to sample. Following this, the focus was readjusted back to the sample plane, and a sample image was acquired. This procedure was repeated for each spectral point.

To process the images and segment the pheomelanin from the image background, the 11 acquired images were summed together and normalized to obtain a grayscale image ranging from 0 to 1. A binary mask was then created using 0.6 as a threshold; lower pixel values were set to 0 while greater values were set to 1. This threshold value was determined through iterative adjustments until the white areas of the binary mask overlapped best with the pheomelanin aggregates visible in the microscope images. This preliminary mask was then processed using morphological cleaning and filling to removed isolated bright pixels (1s surrounded by 0s) and fill isolated dark pixels (0s surrounded by 1s). The resulting binary mask was then multiplied on a pixel-by-pixel basis with each image of the spectrum to produce a pheomelanin-only set of images. The unmasked regions of each image were then averaged together to produce a single pheomelanin data point per image, *i.e.*, one data point per Raman shift. Since the images were encoded over 12 bits, the intensity values varied over a dynamic range of 0 to 4095. The inverse mask was also used in the same fashion in order to create a single data point of the image background for each Raman shift. The intensity values of the reference glass images were averaged across the entire image; the resulting mean value was used as the glass reference data point for the corresponding Raman shift. To generate CARS spectra, each data point (pheomelanin or background) was divided by the glass reference value for each Raman shift. The resulting spectrum was then normalized by the area under its curve, calculated by trapezoidal numerical integration. This process was repeated n times; the means of the *n* trials were plotted as a function of Raman shift, with error bars corresponding to ±1 standard deviation.

4.4.5 GENERATION OF TDTOMATO-EXPRESSING MOUSE LINES

To generate mouse lines that express tdTomato in melanocytes, the mice described in Section 4.1.1 and Figure 4.1.4 (black, redhead, or albino, as described above) were crossed with C57BL/6.Cg-$Gt(ROSA)26Sor^{tm9(CAG-tdTomato)Hze}$/J mice (The Jackson Laboratory), which contain a conditional tdTomato preceded by a *loxP*-flanked STOP cassette. Offspring displaying the appropriate genetic background were selected and bred again with mice containing a *Cre* allele driven by a melanocyte-specific *Tyr* promoter; thus, these doubly transgenic mice in principle only express tdTomato in melanocytes, where *Cre* is expressed and the STOP cassette is resultantly excised. [6]

4.4.6 ISOLATION AND ANTIBODY STAINING OF MOUSE MELANOCYTES

To isolate dermal melanocytes, approximately eight 48-72 hour newborn mouse pups of the appropriate genetic background were euthanized through asphyxiation with CO_2 and their carcasses were rolled in a 70% solution of ethanol. The carcasses were decapitated, the limbs and tails were removed, and the carcasses were rinsed several times in a solution of 2% BSA in Dulbecco's PBS supplemented with antibiotics and fungizone; the carcass was left to soak in the final rinse solution for approximately 60 minutes at room temperature. Carcasses were split down the midline, the skin was removed, and any residual fascia was trimmed away. Skins were flattened and laid dermal side up in a 100 mm petri dish containing 7-10 ml 0.25% trypsin, and the skin-containing dishes were refrigerated overnight at 4 C°. The following morning, the epidermis was separated from the dermis using sterile forceps, and skins were placed in 15 ml tubes, each containing 3 ml of 0.25% tryispin and 1 mM EDTA (1-4 skins/tube). Tubes were placed in a 37 C°incubator for 15 minutes, after which 3 ml of 2% BSA-PBS was was added to each tube, and the contents of each tube were gently

---

[6] The Fisher lab gratefully acknowledges Lynda Chin for providing the *Tyr-Cre* mice.

pipetted up and down approximately 15 times using a 5 ml pipette. The skin matrix was removed from each tube (with the melanocytes remaining as a suspension) and tubes were centrifuged at 1100 RPM for 5 minutes to pellet cells.

After centrifugation, the supernatant was discarded, cells were resuspended in a small volume of 2%-BSA PBS, passed through a 100 μm filter, and transferred to a small Eppendorf tube for antibody staining. Each tube was treated with 10 μl of AB24870 (Abcam), a FITC-conjugated rat monoclonal antibody against c-Kit, and the tube was placed on ice for 30 minutes, following which 1 ml 2% BSA-PBS was added to each tube. FACS was performed after antibody staining, with the cells sorted by C-Kit fluorescence, tdTomato expression, or both, where relevant. Cells that exhibited the highest fluorescence levels of each group were then fixed, transferred to microscope slides prepared with Secure-Seal™imaging spacers, and sealed with red nail polish, as described in 4.4.3. CARS images were acquired as described in the text.

4.4.7 Preparation of UACC 257 human melanoma cells and siRNA knockdown

UACC-257 human melanoma cells were plated on six-well glass-bottomed plates (In Vitro Scientific, Inc.) at a density of $5x10^5$ cells/well in 900 μl RMPI culture medium, to which a solution of 97 μl sodium acetate (25 mM), 2 μl lipoid (1 mg/ml), and 1 μl siRNA (10 μM) were added. Cells were transferred to a 37°incubator, and the media was changed after 24 hours; following this media change, all cells were incubated for an additional 4 days to allow pigmentation changes to occur. (siRNA treatments were performed by Dr. Elizabeth Roider, a research in our collaborator David Fisher's lab, in accordance with her standard protocols and preferences). CARS spectra were acquired as above.

References

[1] Conor L Evans and X Sunney Xie. Coherent anti-stokes Raman scattering microscopy: chemical imaging for biology and medicine. *Annual review of analytical chemistry (Palo Alto, Calif.)*, 1:883–909, January 2008.

[2] Lihong V Wang and Song Hu. Photoacoustic tomography: in vivo imaging from organelles to organs. *Science (New York, N.Y.)*, 335(6075):1458–62, March 2012.

[3] J. Priestley. An Account of Further Discoveries in Air. By the Rev. Joseph Priestley, LL.D. F. R. S. in Letters to Sir John Pringle, Bart. P. R. S. and the Rev. Dr. Price, F. R. S. *Philosophical Transactions of the Royal Society of London*, 65:384–394, January 1775.

[4] C A Hampel. *The Encyclopedia of the Chemical Elements*. Reinhold Book Corporation, 1968.

[5] Donald Voet and Judith G. Voet. *Biochemistry*. Wiley, Hoboken, NJ, 3rd edition, 2004.

[6] R M Berne, B M Koeppen, and B A Stanton. *Berne and Levy Physiology*. Number p. 578 in Berne & Levy Physiology. Mosby/Elsevier, 2008.

[7] Aude Carreau, Bouchra El Hafny-Rahbi, Agata Matejuk, Catherine Grillon, and Claudine Kieda. Why is the partial oxygen pressure of human tissues a crucial parameter? Small molecules and hypoxia. *Journal of cellular and molecular medicine*, 15(6):1239–53, June 2011.

[8] Vikram Dhawan and Michael DeGeorgia. Neurointensive care biophysiological monitoring. *Journal of neurointerventional surgery*, 4(6):407–13, November 2012.

[9] Adam J Brooks, John S Hammond, Keith Girling, and Ian J Beckingham. The effect of hepatic vascular inflow occlusion on liver tissue pH, carbon dioxide, and oxygen partial pressures: defining the optimal clamp/release regime for intermittent portal clamping. *The Journal of surgical research*, 141(2):247–51, August 2007.

[10] L S Lilly and H M School. *Pathophysiology of Heart Disease: A Collaborative Project of Medical Students and Faculty*. Wolters Kluwer/Lippincott Williams & Wilkins, 2011.

[11] M Carrier, S Trudelle, P Thai, and L Pelletier. Ischemic threshold during cold blood cardioplegic arrest: monitoring with tissue pH and pO2. *The Journal of cardiovascular surgery*, 39(5):593–7, October 1998.

[12] Babs R Soller, Charles Hsi, Janice Favreau, Ndumiso Cingo, Robert A Lancey, Okike N Okike, and Thomas J Vander Salm. Multiparameter fiber optic sensor for the assessment of intramyocardial perfusion. *Journal of cardiac surgery*, 19(2):167–74, 2004.

[13] Søren Erik Pischke, Christian Tronstad, Lars Holhjem, Per Steinar Halvorsen, and Tor Inge Tø nnessen. Perioperative detection of myocardial ischaemia/reperfusion with a novel tissue CO2 monitoring technology. *European journal of cardio-thoracic surgery : official journal of the European Association for Cardio-thoracic Surgery*, 42(1):157–63, July 2012.

[14] Charanjit Kaur, Wallace S Foulds, and Eng-Ang Ling. Hypoxia-ischemia and retinal ganglion cell damage. *Clinical ophthalmology (Auckland, N.Z.)*, 2(4):879–89, December 2008.

[15] Guénahel H Danet. Expansion of human SCID-repopulating cells under hypoxic conditions. *Journal of Clinical Investigation*, 112(1):126–135, July 2003.

[16] Kalindi Parmar, Peter Mauch, Jo-Anne Vergilio, Robert Sackstein, and Julian D Down. Distribution of hematopoietic stem cells in the bone marrow according to regional hypoxia. *Proceedings of the National Academy of Sciences of the United States of America*, 104(13):5431–6, March 2007.

[17] Joel A Spencer, Francesca Ferraro, Emmanuel Roussakis, Alyssa Klein, Juwell Wu, Judith M Runnels, Walid Zaher, Luke J Mortensen, Clemens Alt, Raphaël Turcotte, Rushdia Yusuf, Daniel Côté, Sergei A Vinogradov, David T Scadden, and Charles P Lin. Direct measurement of local oxygen concentration in the bone marrow of live animals. *Nature*, 508(7495):269–73, April 2014.

[18] Jen-Tsan Chi, Zhen Wang, Dimitry S A Nuyten, Edwin H Rodriguez, Marci E Schaner, Ali Salim, Yun Wang, Gunnar B Kristensen, Aslaug Helland, Anne-Lise Bø rresen Dale, Amato Giaccia, Michael T Longaker, Trevor Hastie, George P Yang, Marc J van de Vijver, and Patrick O Brown. Gene expression programs in response to hypoxia: cell type specificity and prognostic significance in human cancers. *PLoS medicine*, 3(3):e47, March 2006.

[19] Yair Benita, Hirotoshi Kikuchi, Andrew D Smith, Michael Q Zhang, Daniel C Chung, and Ramnik J Xavier. An integrative genomics approach identifies Hypoxia Inducible Factor-1 (HIF-1)-target genes that form the core response to hypoxia. *Nucleic acids research*, 37(14):4587–602, August 2009.

[20] Nadine Rohwer and Thorsten Cramer. Hypoxia-mediated drug resistance: novel insights on the functional interaction of HIFs and cell death pathways. *Drug resistance updates : reviews and commentaries in antimicrobial and anticancer chemotherapy*, 14(3):191–201, June 2011.

[21] H F Bunn and R O Poyton. Oxygen sensing and molecular adaptation to hypoxia. *Physiological reviews*, 76(3):839–85, July 1996.

[22] Julián Aragonés, Martin Schneider, Katie Van Geyte, Peter Fraisl, Tom Dresselaers, Massimiliano Mazzone, Ruud Dirkx, Serena Zacchigna, Hélène Lemieux, Nam Ho Jeoung, Diether Lambrechts, Tammie Bishop, Peggy Lafuste, Antonio Diez-Juan, Sarah K Harten, Pieter Van Noten, Katrien De Bock, Carsten Willam, Marc Tjwa, Alexandra Grosfeld, Rachel Navet, Lieve Moons, Thierry Vandendriessche, Christophe Deroose, Bhathiya Wijeyekoon, Johan Nuyts, Benedicte Jordan, Robert Silasi-Mansat, Florea Lupu, Mieke Dewerchin, Chris Pugh, Phil Salmon, Luc Mortelmans, Bernard Gallez, Frans Gorus, Johan Buyse, Francis Sluse, Robert a Harris, Erich Gnaiger, Peter Hespel, Paul Van Hecke, Frans Schuit, Paul Van Veldhoven, Peter Ratcliffe, Myriam Baes, Patrick Maxwell, and Peter Carmeliet. Deficiency or inhibition of oxygen sensor Phd1 induces hypoxia tolerance by reprogramming basal metabolism. *Nature genetics*, 40(2):170–80, February 2008.

[23] Eric L Bell, Tatyana A Klimova, James Eisenbart, Carlos T Moraes, Michael P Murphy, G R Scott Budinger, and Navdeep S Chandel. The Qo site of the mitochondrial complex III is required for the transduction of hypoxic signaling via reactive oxygen species production. *The Journal of cell biology*, 177(6):1029–36, June 2007.

[24] Shigeomi Shimizu, Yutaka Eguchi, Wataru Kamiike, Y Itoh, J Hasegawa, K Yamabe, Y Otsuki, H Matsuda, and Y Tsujimoto. Induction of apoptosis as well as necrosis by hypoxia and predominant prevention of apoptosis by Bcl-2 and Bcl-XL. *Cancer research*, 56(9):2161–6, May 1996.

[25] Min Xu and Hui-ling Zhang. Death and survival of neuronal and astrocytic cells in ischemic brain injury: a role of autophagy. *Acta pharmacologica Sinica*, 32(9):1089–99, September 2011.

[26] Yu-Long Hu, Michael DeLay, Arman Jahangiri, Annette M Molinaro, Samuel D Rose, W Shawn Carbonell, and Manish K Aghi. Hypoxia-induced autophagy promotes tumor cell survival and adaptation to antiangiogenic treatment in glioblastoma. *Cancer research*, 72(7):1773–83, April 2012.

[27] Colin R Lenihan and Cormac T Taylor. The impact of hypoxia on cell death pathways. *Biochemical Society transactions*, 41(2):657–63, April 2013.

[28] Zhao Yang, Tian-Zhi Zhao, Yong-Jie Zou, John H Zhang, and Hua Feng. Hypoxia Induces Autophagic Cell Death through Hypoxia-Inducible Factor 1α in Microglia. *PloS one*, 9(5):e96509, January 2014.

[29] William R Wilson and Michael P Hay. Targeting hypoxia in cancer therapy. *Nature reviews. Cancer*, 11(6):393–410, July 2011.

[30] Douglas Hanahan, R.A. Weinberg, and Others. The Hallmarks of Cancer. *Cell*, 100(1):57–70, 2000.

[31] Judah Folkman. Angiogenesis. *Annual review of medicine*, 57:1–18, January 2006.

[32] Judah Folkman. Angiogenesis: an organizing principle for drug discovery? *Nature reviews. Drug discovery*, 6(4):273–86, April 2007.

[33] Douglas Hanahan and Robert A Weinberg. Hallmarks of cancer: the next generation. *Cell*, 144(5):646–74, March 2011.

[34] Daniel Ackerman and M Celeste Simon. Hypoxia, lipids, and cancer: surviving the harsh tumor microenvironment. *Trends in Cell Biology*, July 2014.

[35] Rui-hua Xu, Helene Pelicano, Yan Zhou, Jennifer S Carew, Li Feng, Kapil N Bhalla, Michael J Keating, and Peng Huang. Inhibition of glycolysis in cancer cells: a novel strategy to overcome drug resistance associated with mitochondrial respiratory defect and hypoxia. *Cancer research*, 65(2):613–21, January 2005.

[36] Xianrang Song, Xianxi Liu, Weiling Chi, Yonglei Liu, Ling Wei, Xingwu Wang, and Jinming Yu. Hypoxia-induced resistance to cisplatin and doxorubicin in non-small cell lung cancer is inhibited by silencing of HIF-1alpha gene. *Cancer chemotherapy and pharmacology*, 58(6):776–84, December 2006.

[37] J Martin Brown. Tumor hypoxia in cancer therapy. *Methods in enzymology*, 435:297–321, January 2007.

[38] S Koch, F Mayer, F Honecker, M Schittenhelm, and C Bokemeyer. Efficacy of cytotoxic agents used in the treatment of testicular germ cell tumours under normoxic and hypoxic conditions in vitro. *British journal of cancer*, 89(11):2133–9, December 2003.

[39] Jonathan P Celli, Imran Rizvi, Conor L Evans, Adnan O Abu-Yousif, and Tayyaba Hasan. Quantitative imaging reveals heterogeneous growth dynamics and treatment-dependent residual tumor distributions in a three-dimensional ovarian cancer model. *Journal of biomedical optics*, 15(5):051603, 2010.

[40] Conor L Evans, Adnan O Abu-Yousif, Yong Jin Park, Oliver J Klein, Jonathan P Celli, Imran Rizvi, Xiang Zheng, and Tayyaba Hasan. Killing Hypoxic Cell Populations in a 3D Tumor Model with EtNBS-PDT. *PloS one*, 6(8):e23434, January 2011.

[41] Oliver J Klein, Brijesh Bhayana, Yong Jin Park, and Conor L Evans. In vitro optimization of EtNBS-PDT against hypoxic tumor environments with a tiered, high-content, 3D model optical screening platform. *Molecular pharmaceutics*, 9(11):3171–82, November 2012.

[42] Xu-dong Wang and Otto S Wolfbeis. Optical methods for sensing and imaging oxygen: materials, spectroscopies and applications. *Chemical Society reviews*, 43(10):3666–761, May 2014.

[43] J M Vanderkooi, G Maniara, T J Green, and D F Wilson. An optical method for measurement of dioxygen concentration based upon quenching of phosphorescence. *The Journal of biological chemistry*, 262(12):5476–82, April 1987.

[44] Sergei A Vinogradov and David F Wilson. Porphyrin dendrimers as biological oxygen sensors. In Sebastiano Campagna, Paola Ceroni, and Fausto Puntoriero, editors, *Designing Dendrimers*, chapter 12, pages 463–503. Wiley, Hoboken, New Jersey, 1st edition, 2012.

[45] Shaojuan Zhang, Masahiro Hosaka, Toshitada Yoshihara, Kazuya Negishi, Yasuhiko Iida, Seiji Tobita, and Toshiyuki Takeuchi. Phosphorescent light-emitting iridium complexes serve as a hypoxia-sensing probe for tumor imaging in living animals. *Cancer research*, 70(11):4490–8, June 2010.

[46] Ruslan I Dmitriev and Dmitri B Papkovsky. Optical probes and techniques for O2 measurement in live cells and tissue. *Cellular and molecular life sciences : CMLS*, 69(12):2025–39, June 2012.

[47] S A Vinogradov and D F Wilson. Phosphorescence lifetime analysis with a quadratic programming algorithm for determining quencher distributions in heterogeneous systems. *Biophysical journal*, 67(5):2048–59, November 1994.

[48] W L Rumsey, J M Vanderkooi, and D F Wilson. Imaging of phosphorescence: a novel method for measuring oxygen distribution in perfused tissue. *Science*, 241(4873):1649–51, September 1988.

[49] R J Woods, Stephen Scypinski, and L J Cline Love. Transient digitizer for the determination of microsecond luminescence lifetimes. *Analytical Chemistry*, 56(8):1395–1400, July 1984.

[50] Richard M Ballew and J N Demas. An error analysis of the rapid lifetime determination method for the evaluation of single exponential decays. *Analytical Chemistry*, 61(1):30–33, January 1989.

[51] Bernard Valeur. *Molecular Fluorescence: Principles and Applications*. 2010.

[52] Matthias I J Stich, Lorenz H Fischer, and Otto S Wolfbeis. Multiple fluorescent chemical sensing and imaging. *Chemical Society reviews*, 39(8):3102–14, August 2010.

[53] Sergei A Vinogradov, Maria A Fernandez-Searra, Benjamin W Dugan, and David F Wilson. Frequency domain instrument for measuring phosphorescence lifetime distributions in heterogeneous samples. *Review of Scientific Instruments*, 72(8):3396, 2001.

[54] David F Wilson, Sergei A Vinogradov, Benjamin W Dugan, Dubravko Biruski, Lee Waldron, and Sydney A Evans. Measurement of tumor oxygenation using new frequency domain phosphorometers. *Comparative Biochemistry and Physiology Part A: Molecular & Integrative Physiology*, 132(1):153–159, May 2002.

[55] Lisa S Ziemer, William M. F Lee, Sergei A Vinogradov, Chandra Sehgal, and David F Wilson. Oxygen distribution in murine tumors: characterization using oxygen-dependent quenching of phosphorescence. *J Appl Physiol*, 98(4):1503–1510, April 2005.

[56] Elmar Schmälzlin, Joost T van Dongen, Ingo Klimant, Bettina Marmodée, Martin Steup, Joachim Fisahn, Peter Geigenberger, and Hans-Gerd Löhmannsröben. An optical multi-frequency phase-modulation method using microbeads for measuring intracellular oxygen concentrations in plants. *Biophysical journal*, 89(2):1339–45, August 2005.

[57] Joseph R Lakowicz and Klaus W Berndt. Lifetime-selective fluorescence imaging using an rf phase-sensitive camera. *Review of Scientific Instruments*, 62(7):1727, 1991.

[58] Ross D Shonat and Amanda C Kight. Oxygen Tension Imaging in the Mouse Retina. *Annals of Biomedical Engineering*, 31(9):1084–1096, October 2003.

[59] Chen-Shane Chu and Yu-Lung Lo. 2D full-field measurement of oxygen concentration based on the phase fluorometry technique that uses the four-frame integrating-bucket method. *Sensors and Actuators B: Chemical*, 147(1):310–315, May 2010.

[60] Mahsa Ranji, Dwight L Jaggard, Sofia V Apreleva, Sergei A Vinogradov, and Britton Chance. Simultaneous fluorometry and phosphorometry of Langendorff perfused rat heart: ex vivo animal studies. *Optics letters*, 31(20):2995–7, October 2006.

[61] Sava Sakadzić, Emmanuel Roussakis, Mohammad A Yaseen, Emiri T Mandeville, Vivek J Srinivasan, Ken Arai, Svetlana Ruvinskaya, Anna Devor, Eng H Lo, Sergei A Vinogradov, and David A Boas. Two-photon high-resolution measurement of partial pressure of oxygen in cerebral vasculature and tissue. *Nature methods*, 7(9):755–9, September 2010.

[62] Jérôme Lecoq, Alexandre Parpaleix, Emmanuel Roussakis, Mathieu Ducros, Yannick Goulam Houssen, Sergei A Vinogradov, and Serge Charpak. Simultaneous two-photon imaging of oxygen and blood flow in deep cerebral vessels. *Nature medicine*, 17(7):893–8, July 2011.

[63] Isolde Dunphy, Sergei A Vinogradov, and David F Wilson. Oxyphor R2 and G2: phosphors for measuring oxygen by oxygen-dependent quenching of phosphorescence. *Analytical biochemistry*, 310(2):191–8, November 2002.

[64] Sergei A Vinogradov, Evelyn Kim, and David F Wilson. Pd tetrabenzoporphyrin-dendrimers - near infrared phosphors for oxygen measurements by phosphorescence quenching. volume 4626, pages 193–200, June 2002.

[65] Calvin D Roskelley and Mina J Bissell. The dominance of the microenvironment in breast and ovarian cancer. *Seminars in cancer biology*, 12(2):97–104, April 2002.

[66] H Xu, J W Aylott, R Kopelman, T J Miller, and M A Philbert. A real-time ratiometric method for the determination of molecular oxygen inside living cells using sol-gel-based spherical optical nanosensors with applications to rat C6 glioma. *Analytical Chemistry*, 73(17):4124–4133, September 2001.

[67] Yong-Eun Lee Koo, Youfu Cao, Raoul Kopelman, Sang Man Koo, Murphy Brasuel, and Martin A Philbert. Real-time measurements of dissolved oxygen inside live cells by organically modified silicate fluorescent nanosensors. *Analytical chemistry*, 76(9):2498–505, May 2004.

[68] Youfu Cao, Yong-Eun Lee Koo, and Raoul Kopelman. Poly(decyl methacrylate)-based fluorescent PEBBLE swarm nanosensors for measuring dissolved oxygen in biosamples. *The Analyst*, 129(8):745–50, August 2004.

[69] Tomás C O'Riordan, Kathleen Fitzgerald, Gelii V Ponomarev, John Mackrill, James Hynes, Cormac Taylor, and Dmitri B Papkovsky. Sensing intracellular oxygen using near-infrared phosphorescent probes and live-cell fluorescence imaging. *American journal of physiology. Regulatory, integrative and comparative physiology*, 292(4):R1613–20, April 2007.

[70] Bradley B Collier, Saurabh Singh, and Mike McShane. Microparticle ratiometric oxygen sensors utilizing near-infrared emitting quantum dots. *The Analyst*, December 2010.

[71] Haifeng Xiang, Li Zhou, Yan Feng, Jinghui Cheng, Di Wu, and Xiangge Zhou. Tunable Fluorescent/Phosphorescent Platinum(II) Porphyrin-Fluorene Copolymers for Ratiometric Dual Emissive Oxygen Sensing. *Inorganic chemistry*, 51(9):5208–12, May 2012.

[72] Toshitada Yoshihara, Yuji Yamaguchi, Masahiro Hosaka, Toshiyuki Takeuchi, and Seiji Tobita. Ratiometric molecular sensor for monitoring oxygen levels in living cells. *Angewandte Chemie (International ed. in English)*, 51(17):4148–51, April 2012.

[73] O Boussif, F Lezoualc'h, M A Zanta, M D Mergny, D Scherman, B Demeneix, and J P Behr. A versatile vector for gene and oligonucleotide transfer into cells in culture and in vivo: polyethylenimine. *Proceedings of the National Academy of Sciences of the United States of America*, 92(16):7297–7301, 1995.

[74] Hyukjin Lee, In-Kyoung Kim, and Tae Gwan Park. Intracellular trafficking and unpacking of siRNA/quantum dot-PEI complexes modified with and without cell penetrating peptide: confocal and flow cytometric FRET analysis. *Bioconjugate chemistry*, 21(2):289–95, February 2010.

[75] J Peterson, A Ebber, V Allikmaa, and M Lopp. Synthesis and CZE analysis of PAMAM dendrimers with an ethylenediamine core. *Proceedings of the Estonian Academy of Sciences*, 50(3):156–166, 2001.

[76] D A Tomalia, H Baker, J Dewald, M Hall, G Kallos, S Martin, J Roeck, J Ryder, and P Smith. A New Class of Polymers: Starburst-Dendritic Macromolecules. *Polymer Journal*, 17(1):117–132, January 1985.

[77] S Sadekar and H Ghandehari. Transepithelial transport and toxicity of PAMAM dendrimers: implications for oral drug delivery. *Advanced drug delivery reviews*, 64(6):571–88, May 2012.

[78] Anil K Patri, István J Majoros, and James R Baker. Dendritic polymer macromolecular carriers for drug delivery. *Current Opinion in Chemical Biology*, 6(4):466–471, August 2002.

[79] Christine Dufès, Ijeoma F Uchegbu, and Andreas G Schätzlein. Dendrimers in gene delivery. *Advanced drug delivery reviews*, 57(15):2177–202, December 2005.

[80] Javier López-Andarias, Javier Guerra, Gregorio Castañeda, Sonia Merino, Valentín Ceña, and Prado Sánchez-Verdú. Development of Microwave-Assisted Reactions for PAMAM Dendrimer Synthesis. *European Journal of Organic Chemistry*, 2012(12):2331–2337, April 2012.

[81] Barbara Klajnert, Lidia Stanisławska, Maria Bryszewska, and Bartłomiej Pałecz. Interactions between PAMAM dendrimers and bovine serum albumin. *Biochimica et Biophysica Acta (BBA) - Proteins and Proteomics*, 1648(1-2):115–126, May 2003.

[82] Hartmuth C Kolb, M G Finn, and K Barry Sharpless. Click Chemistry: Diverse Chemical Function from a Few Good Reactions. *Angewandte Chemie (International ed. in English)*, 40(11):2004–2021, June 2001.

[83] Vsevolod V Rostovtsev, Luke G Green, Valery V Fokin, and K Barry Sharpless. A stepwise huisgen cycloaddition process: copper(I)-catalyzed regioselective "ligation" of azides and terminal alkynes. *Angewandte Chemie (International ed. in English)*, 41(14):2596–9, July 2002.

[84] Jae Wook Lee, Hee Joo Kim, Seung Choul Han, Ji Hyeon Kim, and Sung-Ho Jin. Designing poly(amido amine) dendrimers containing core diversities by click chemistry of the propargyl focal point poly(amido amine) dendrons. *Journal of Polymer Science Part A: Polymer Chemistry*, 46(3):1083–1097, February 2008.

[85] Ibai E Valverde, Agnès F Delmas, and Vincent Aucagne. Click à la carte: robust semi-orthogonal alkyne protecting groups for multiple successive azide/alkyne cycloadditions. *Tetrahedron*, 65(36):7597–7602, September 2009.

[86] Vladimir Rozhkov, David Wilson, and Sergei Vinogradov. Phosphorescent Pd Porphyrin Dendrimers: Tuning Core Accessibility by Varying the Hydrophobicity of the Dendritic Matrix. *Macromolecules*, 35(6):1991–1993, March 2002.

[87] Shuang Liu. Radiolabeled multimeric cyclic RGD peptides as integrin alphavbeta3 targeted radiotracers for tumor imaging. *Molecular pharmaceutics*, 3(5):472–87, 2006.

[88] Ingrid Dijkgraaf, Anneloes Y Rijnders, Annemieke Soede, Annemarie C Dechesne, G Wilma van Esse, Arwin J Brouwer, Frans H M Corstens, Otto C Boerman, Dirk T S Rijkers, and Rob M J Liskamp. Synthesis of DOTA-conjugated multivalent cyclic-RGD peptide dendrimers via 1,3-dipolar cycloaddition and their biological evaluation: implications for tumor targeting and tumor imaging purposes. *Organic & biomolecular chemistry*, 5(6):935–44, March 2007.

[89] Tamotsu Zako, Hiroyasu Nagata, Naofumi Terada, Arata Utsumi, Masafumi Sakono, Masafumi Yohda, Hiroshi Ueda, Kohei Soga, and Mizuo Maeda. Cyclic RGD peptide-labeled upconversion nanophosphors for tumor cell-targeted imaging. *Biochemical and biophysical research communications*, 381(1):54–8, March 2009.

[90] Shuang Liu. Radiolabeled cyclic RGD peptides as integrin alpha(v)beta(3)-targeted radiotracers: maximizing binding affinity via bivalency. *Bioconjugate chemistry*, 20(12):2199–213, December 2009.

[91] Carolyn L Waite and Charles M Roth. PAMAM-RGD conjugates enhance siRNA delivery through a multicellular spheroid model of malignant glioma. *Bioconjugate chemistry*, 20(10):1908–16, October 2009.

[92] Carolyn L Waite and Charles M Roth. Binding and transport of PAMAM-RGD in a tumor spheroid model: The effect of RGD targeting ligand density. *Biotechnology and bioengineering*, 108(12):2999–3008, July 2011.

[93] Yanyan Guo, Hushan Yuan, William L Rice, Anand T N Kumar, Craig J Goergen, Kimmo Jokivarsi, and Lee Josephson. The PEG-fluorochrome shielding approach for targeted probe design. *Journal of the American Chemical Society*, 134(47):19338–41, November 2012.

[94] C P Leamon and P S Low. Delivery of macromolecules into living cells: a method that exploits folate receptor endocytosis. *Proceedings of the National Academy of Sciences of the United States of America*, 88(13):5572–6, July 1991.

[95] J Sudimack and R J Lee. Targeted drug delivery via the folate receptor. *Advanced drug delivery reviews*, 41(2):147–62, March 2000.

[96] Michael D Kennedy, Karim N Jallad, David H Thompson, Dor Ben-Amotz, and Philip S Low. Optical imaging of metastatic tumors using a folate-targeted fluorescent probe. *Journal of biomedical optics*, 8(4):636–41, October 2003.

[97] Dhruba J Bharali, Derrick W Lucey, Harishankar Jayakumar, Haridas E Pudavar, and Paras N Prasad. Folate-receptor-mediated delivery of InP quantum dots for bioimaging using confocal and two-photon microscopy. *Journal of the American Chemical Society*, 127(32):11364–71, August 2005.

[98] Yili Zhao, Sen Liu, Yapeng Li, Wei Jiang, Yulei Chang, Si Pan, Xuexun Fang, Y Andrew Wang, and Jingyuan Wang. Synthesis and grafting of folate-PEG-PAMAM conjugates onto quantum dots for selective targeting of folate-receptor-positive tumor cells. *Journal of colloid and interface science*, 350(1):44–50, October 2010.

[99] Chao Zhang, Shijuan Gao, Wei Jiang, Song Lin, Fusheng Du, Zichen Li, and Wenlin Huang. Targeted minicircle DNA delivery using folate-poly(ethylene glycol)-polyethylenimine as non-viral carrier. *Biomaterials*, 31(23):6075–86, August 2010.

[100] Seok Ki Choi, Thommey Thomas, Ming-Hsin Li, Alina Kotlyar, Ankur Desai, and James R Baker. Light-controlled release of caged doxorubicin from folate receptor-targeting PAMAM dendrimer nanoconjugate. *Chemical communications (Cambridge, England)*, 46(15):2632–4, April 2010.

[101] Gooitzen M van Dam, George Themelis, Lucia M A Crane, Niels J Harlaar, Rick G Pleijhuis, Wendy Kelder, Athanasios Sarantopoulos, Johannes S de Jong, Henriette J G Arts, Ate G J van der Zee, Joost Bart, Philip S Low, and Vasilis Ntziachristos. Intraoperative tumor-specific fluorescence imaging in ovarian cancer by folate receptor-α targeting: first in-human results. *Nature Medicine*, 17(10):1315–1319, September 2011.

[102] Xu-dong Wang, Judith a Stolwijk, Thomas Lang, Michaela Sperber, Robert J Meier, Joachim Wegener, and Otto S Wolfbeis. Ultra-small, highly stable, and sensitive dual nanosensors for imaging intracellular oxygen and pH in cytosol. *Journal of the American Chemical Society*, 134(41):17011–4, October 2012.

[103] Birgit Ungerböck, Verena Charwat, Peter Ertl, and Torsten Mayr. Microfluidic oxygen imaging using integrated optical sensor layers and a color camera. *Lab on a chip*, February 2013.

[104] Levi A Garraway and Pasi A Jänne. Circumventing cancer drug resistance in the era of personalized medicine. *Cancer discovery*, 2(3):214–26, March 2012.

[105] Eliezer M Van Allen, Nikhil Wagle, Petar Stojanov, Danielle L Perrin, Kristian Cibulskis, Sara Marlow, Judit Jane-Valbuena, Dennis C Friedrich, Gregory Kryukov, Scott L Carter, Aaron McKenna, Andrey Sivachenko, Mara Rosenberg, Adam Kiezun, Douglas Voet, Michael Lawrence, Lee T Lichtenstein, Jeff G Gentry, Franklin W Huang, Jennifer Fostel, Deborah Farlow, David Barbie, Leena Gandhi, Eric S Lander, Stacy W Gray, Steven Joffe, Pasi Janne, Judy Garber, Laura MacConaill, Neal Lindeman, Barrett Rollins, Philip Kantoff, Sheila a Fisher, Stacey Gabriel, Gad Getz, and Levi a Garraway. Whole-exome sequencing and clinical interpretation of formalin-fixed, paraffin-embedded tumor samples to guide precision cancer medicine. *Nature Medicine*, (April 2013), May 2014.

[106] Nikhil Wagle, Brian C Grabiner, Eliezer M Van Allen, Eran Hodis, Susanna Jacobus, Jeffrey G Supko, Michelle Stewart, Toni K Choueiri, Leena Gandhi, James M Cleary, Aymen a Elfiky, Mary Ellen Taplin, Edward C Stack, Sabina Signoretti, Massimo Loda, Geoffrey I Shapiro, David M Sabatini, Eric S Lander, Stacey B Gabriel, Philip W Kantoff, Levi a Garraway, and Jonathan E Rosenberg. Activating mTOR Mutations in a Patient with an Extraordinary Response on a Phase I Trial of Everolimus and Pazopanib. *Cancer discovery*, March 2014.

[107] Alexander J Nichols, Emmanuel Roussakis, Oliver J Klein, and Conor L Evans. Click-assembled, oxygen-sensing nanoconjugates for depth-resolved, near-infrared imaging in a 3D cancer model. *Angewandte Chemie (International ed. in English)*, 53(14):3671–4, April 2014.

[108] Hugo E Gottlieb, Vadim Kotlyar, and Abraham Nudelman. NMR Chemical Shifts of Common Laboratory Solvents as Trace Impurities. *The Journal of Organic Chemistry*, 62(21):7512–7515, October 1997.

[109] Li Zhou, David H Russell, Mingqi Zhao, and Richard M Crooks. Characterization of Poly(amidoamine) Dendrimers and Their Complexes with Cu 2+ by Matrix-Assisted Laser Desorption Ionization Mass Spectrometry. *Macromolecules*, 34(11):3567–3573, May 2001.

[110] Jae Wook Lee, Jung Hwan Kim, Byung-Ku Kim, Ji Hyeon Kim, Won Suk Shin, and Sung-Ho Jin. Convergent synthesis of PAMAM dendrimers using click chemistry of azide-functionalized PAMAM dendrons. *Tetrahedron*, 62(39):9193–9200, September 2006.

[111] Jae Wook Lee, Byung-Ku Kim, Hee Joo Kim, Seung Choul Han, Won Suk Shin, and Sung-Ho Jin. Convergent Synthesis of Symmetrical and Unsymmetrical PAMAM Dendrimers. *Macromolecules*, 39(6):2418–2422, March 2006.

[112] Yosuke Kaburagi and Yoshito Kishi. Operationally simple and efficient workup procedure for TBAF-mediated desilylation: application to halichondrin synthesis. *Organic letters*, 9(4):723–6, February 2007.

[113] Alexander J Nichols and Conor L Evans. Video-rate scanning confocal microscopy and microendoscopy. *Journal of visualized experiments : JoVE*, (56):1–10, January 2011.

[114] C K Sen. Wound healing essentials: let there be oxygen. *Wound Repair Regen*, 17(1):1–18, 2009.

[115] A Bishop. Role of oxygen in wound healing. *Journal of Wound Care*, 17:399–402, 2008.

[116] C K Sen, G M Gordillo, S Roy, R Kirsner, L Lambert, T K Hunt, F Gottrup, G C Gurtner, and M T Longaker. Human skin wounds: a major and snowballing threat to public health and the economy. *Wound Repair Regen*, 17(6):763–771, 2009.

[117] Madhuri Reddy, David Keast, Evonne Fowler, and R Gary Sibbald. Pain in pressure ulcers. *Ostomy/wound management*, 49(4 Suppl):30–5, April 2003.

[118] F Gottrup. Oxygen in wound healing and infection. *World J Surg*, 28(3):312–315, 2004.

[119] S Schreml, R M Szeimies, L Prantl, S Karrer, M Landthaler, and P Babilas. Oxygen in acute and chronic wound healing. *Br J Dermatol*, 163(2):257–268, 2010.

[120] J L Burns, J S Mancoll, and L G Phillips. Impairments to wound healing. *Clin Plast Surg*, 30(1):47–56, 2003.

[121] D Xing, L Liu, G P Marti, X Zhang, M Reinblatt, S M Milner, and J W Harmon. Hypoxia and hypoxia-inducible factor in the burn wound. *Wound Repair Regen*, 19(2):205–213, 2011.

[122] Sze Ting Lee and Andrew M Scott. Hypoxia positron emission tomography imaging with 18f-fluoromisonidazole. *Seminars in nuclear medicine*, 37(6):451–61, November 2007.

[123] D M Danilenko, B D Ring, J E Tarpley, B Morris, G Y Van, A Morawiecki, W Callahan, M Goldenberg, S Hershenson, and G F Pierce. Growth factors in porcine full and partial thickness burn repair. Differing targets and effects of keratinocyte growth factor, platelet-derived growth factor-BB, epidermal growth factor, and neu differentiation factor. *Am J Pathol*, 147(5):1261–1277, 1995.

[124] G H Takahashi, I Fatt, and T K Goldstick. Oxygen consumption rate of tissue measured by a micropolarographic method. *J Gen Physiol*, 50(2):317–335, 1966.

[125] C Ruangsetakit, K Chinsakchai, P Mahawongkajit, C Wongwanit, and P Mutirangura. Transcutaneous oxygen tension: a useful predictor of ulcer healing in critical limb ischaemia. *Journal of wound care*, 19(5):202–6, May 2010.

[126] H H Moosa, M S Makaroun, A B Peitzman, D L Steed, and M W Webster. TcPO2 values in limb ischemia: effects of blood flow and arterial oxygen tension. *The Journal of surgical research*, 40(5):482–7, May 1986.

[127] K M Baldwin. Transcutaneous oximetry and skin surface temperature as objective measures of pressure ulcer risk. *Advances in skin & wound care*, 14(1):26–31, 2001.

[128] Yutaka Amao. Probes and Polymers for Optical Sensing of Oxygen. *Microchimica Acta*, 143(1):1–12, September 2003.

[129] Sergey M Borisov, Gunter Zenkl, and Ingo Klimant. Phosphorescent platinum(II) and palladium(II) complexes with azatetrabenzoporphyrins-new red laser diode-compatible indicators for optical oxygen sensing. *ACS applied materials & interfaces*, 2(2):366–74, February 2010.

[130] Chen-Shane Chu, Yu-Lung Lo, and Ti-Wen Sung. Enhanced oxygen sensing properties of Pt(II) complex and dye entrapped core-shell silica nanoparticles embedded in sol-gel matrix. *Talanta*, 82(3):1044–51, August 2010.

[131] Michael B Winter, Emily J McLaurin, Steven Y Reece, Charles Olea, Daniel G Nocera, and Michael a Marletta. Ru-porphyrin protein scaffolds for sensing O2. *Journal of the American Chemical Society*, 132(16):5582–3, April 2010.

[132] Changfeng Wu, Barbara Bull, Kenneth Christensen, and Jason McNeill. Ratiometric single-nanoparticle oxygen sensors for biological imaging. *Angewandte Chemie (International ed. in English)*, 48(15):2741–5, January 2009.

[133] Fabian Niedermair, Sergey M Borisov, Gunter Zenkl, Oliver T Hofmann, Hansjörg Weber, Robert Saf, and Ingo Klimant. Tunable phosphorescent NIR oxygen indicators based on mixed benzo- and naphthoporphyrin complexes. *Inorganic chemistry*, 49(20):9333–42, October 2010.

[134] Artem Y Lebedev, Andrei V Cheprakov, Sava Sakadzić, David A Boas, David F Wilson, and Sergei A Vinogradov. Dendritic phosphorescent probes for oxygen imaging in biological systems. *ACS applied materials & interfaces*, 1(6):1292–304, June 2009.

[135] S Schreml, R J Meier, O S Wolfbeis, T Maisch, R M Szeimies, M Landthaler, J Regensburger, F Santarelli, I Klimant, and P Babilas. 2D luminescence imaging of physiological wound oxygenation. *Exp Dermatol*, 20(7):550–554, 2011.

[136] A Mahnke, R J Meier, V Schatz, J Hofmann, K Castiglione, U Schleicher, O S Wolfbeis, C Bogdan, and J Jantsch. Hypoxia in Leishmania major Skin Lesions Impairs the NO-Dependent Leishmanicidal Activity of Macrophages. *J Invest Dermatol*, 2014.

[137] Julian Hofmann, Valentin Schatz, Christian Bogdan, Jantsch, and Jonathan. Ratiometric luminescence 2D in vivo imaging and monitoring of mouse skin oxygenation. *Methods Appl. Fluoresc.*, 1:45002, 2013.

[138] Joshua S Boateng, Kerr H Matthews, Howard N E Stevens, and Gillian M Eccleston. Wound healing dressings and drug delivery systems: a review. *Journal of pharmaceutical sciences*, 97(8):2892–923, August 2008.

[139] N J Turro. *Modern Molecular Photochemistry*. University Science Books, Sausalito, CA, 1991.

[140] Xu-dong Wang, Robert J Meier, Martin Link, and Otto S Wolfbeis. Photographing oxygen distribution. *Angewandte Chemie (International ed. in English)*, 49(29):4907–9, July 2010.

[141] Sovia V Apreleva, David F Wilson, and Sergei a Vinogradov. Tomographic imaging of oxygen by phosphorescence lifetime. *Applied optics*, 45(33):8547–59, November 2006.

[142] S A Vinogradov, M A Fernandez-Seara, B W Dupan, and D F Wilson. A method for measuring oxygen distributions in tissue using frequency domain phosphorometry. *Comp Biochem Physiol A Mol Integr Physiol*, 132(1):147–152, 2002.

[143] Teresa J Kelechi and Diane E Neal. Skin perfusion pressure in chronic venous disorders. *Advances in skin & wound care*, 21(12):576–81, December 2008.

[144] Ezio Faglia, Faglia Ezio, Giacomo Clerici, Clerici Giacomo, Maurizio Caminiti, Caminiti Maurizio, Antonella Quarantiello, Quarantiello Antonella, Vincenzo Curci, Curci Vincenzo, Francesco Somalvico, and Somalvico Francesco. Evaluation of feasibility of ankle pressure and foot oximetry values for the detection of critical limb ischemia in diabetic patients. *Vascular and endovascular surgery*, 44(3):184–9, April 2010.

[145] C C Powell, S C Schultz, D G Burris, W R Drucker, and D S Malcolm. Subcutaneous oxygen tension: a useful adjunct in assessment of perfusion status. *Critical care medicine*, 23(5):867–73, May 1995.

[146] G S Dowd, K Linge, and G Bentley. Measurement of transcutaneous oxygen pressure in normal and ischaemic skin. *The Journal of bone and joint surgery. British volume*, 65(1):79–83, January 1983.

[147] Juan Barret-Nerin and David N Herndon. *Principles and Practice of Burn Surgery*. New York: Marcel Dekker, 2004.

[148] A Papp, K Kiraly, M Härmä, T Lahtinen, A Uusaro, and E Alhava. The progression of burn depth in experimental burns: a histological and methodological study. *Burns*, 30(7):684–690, 2004.

[149] A Coruh and Y Yontar. Application of split-thickness dermal grafts in deep partial- and full-thickness burns: a new source of auto-skin grafting. *J Burn Care Res*, 33(3):e94–e100, 2012.

[150] J W Alexander, B G MacMillan, E Law, and D S Kittur. Treatment of severe burns with widely meshed skin autograft and meshed skin allograft overlay. *The Journal of trauma*, 21(6):433–8, June 1981.

[151] Zongxi Li, Emmanuel Roussakis, Pieter G. L. Koolen, Ahmed M. S. Ibrahim, Kuylhee Kim, Lloyd F. Rose, Jesse Wu, Alexander J. Nichols, Yunjung Baek, Reginald Birngruber, Gabriela Apiou-Sbirlea, Robina Matyal, Thomas Huang, Rodney Chan, Samuel J. Lin, and Conor L. Evans. Non-invasive transdermal two-dimensional mapping of cutaneous oxygenation with a rapid-drying liquid bandage. *Biomedical Optics Express*, 5(11):3748, October 2014.

[152] E Wenczl, G P Van der Schans, L Roza, R M Kolb, a J Timmerman, N P Smit, S Pavel, and a a Schothorst. (Pheo)melanin photosensitizes UVA-induced DNA damage in cultured human melanocytes. *The Journal of investigative dermatology*, 111(4):678–82, October 1998.

[153] Shosuke Ito and Kazumasa Wakamatsu. Quantitative analysis of eumelanin and pheomelanin in humans, mice, and other animals: a comparative review. *Pigment cell research / sponsored by the European Society for Pigment Cell Research and the International Pigment Cell Society*, 16(5):523–31, October 2003.

[154] Marco D'Ischia, Kazumasa Wakamatsu, Alessandra Napolitano, Stefania Briganti, José-Carlos Garcia-Borron, Daniela Kovacs, Paul Meredith, Alessandro Pezzella, Mauro Picardo, Tadeusz Sarna, John D Simon, and Shosuke Ito. Melanins and melanogenesis: methods, standards, protocols. *Pigment cell & melanoma research*, 26(5):616–33, September 2013.

[155] S Ito and K Fujita. Microanalysis of eumelanin and pheomelanin in hair and melanomas by chemical degradation and liquid chromatography. *Analytical biochemistry*, 144(2):527–36, February 1985.

[156] Giorgia Greco, Lucia Panzella, Luisella Verotta, Marco D'Ischia, and Alessandra Napolitano. Uncovering the structure of human red hair pheomelanin: benzothiazolylthiazinodihydroisoquinolines as key building blocks. *Journal of natural products*, 74(4):675–82, April 2011.

[157] M S Marks and M C Seabra. The melanosome: membrane dynamics in black and white. *Nature reviews. Molecular cell biology*, 2(10):738–48, October 2001.

[158] Graça Raposo and Michael S Marks. Melanosomes–dark organelles enlighten endosomal membrane transport. *Nature reviews. Molecular cell biology*, 8(10):786–97, October 2007.

[159] Arthur R Rhodes, M A Weinstock, T B Fitzpatrick, M C Mihm, and A J Sober. Risk factors for cutaneous melanoma. A practical method of recognizing predisposed individuals. *JAMA : the journal of the American Medical Association*, 258(21):3146–54, December 1987.

[160] D P Lookingbill, G L Lookingbill, and B Leppard. Actinic damage and skin cancer in albinos in northern Tanzania: findings in 164 patients enrolled in an outreach skin care program. *Journal of the American Academy of Dermatology*, 32(4):653–8, April 1995.

[161] H Z Hill and G J Hill. UVA, pheomelanin and the carcinogenesis of melanoma. *Pigment cell research / sponsored by the European Society for Pigment Cell Research and the International Pigment Cell Society*, 13 Suppl 8(7):140–4, January 2000.

[162] Francois Rouzaud, Ana Luisa Kadekaro, Zalfa a Abdel-Malek, and Vincent J Hearing. MC1R and the response of melanocytes to ultraviolet radiation. *Mutation research*, 571(1-2):133–52, April 2005.

[163] Devarati Mitra, Xi Luo, Ann Morgan, Jin Wang, Mai P Hoang, Jennifer Lo, Candace R Guerrero, Jochen K Lennerz, Martin C Mihm, Jennifer a Wargo, Kathleen C Robinson, Suprabha P Devi, Jillian C Vanover, John a D'Orazio, Martin McMahon, Marcus W Bosenberg, Kevin M Haigis, Daniel a Haber, Yinsheng Wang, and David E Fisher. An ultraviolet-radiation-independent pathway to melanoma carcinogenesis in the red hair/fair skin background. *Nature*, 491(7424):449–53, November 2012.

[164] P Valverde, E Healy, I Jackson, J L Rees, and A J Thody. Variants of the melanocyte-stimulating hormone receptor gene are associated with red hair and fair skin in humans. *Nature genetics*, 11(3):328–30, November 1995.

[165] E Elizabeth Patton, Hans R Widlund, Jeffery L Kutok, Kamden R Kopani, James F Amatruda, Ryan D Murphey, Stephane Berghmans, Elizabeth A Mayhall, David Traver, Christopher D M Fletcher, Jon C Aster, Scott R Granter, A Thomas Look, Charles Lee, David E Fisher, and Leonard I Zon. BRAF Mutations Are Sufficient to Promote Nevi Formation and Cooperate with p53 in the Genesis of Melanoma. 15:249–254, 2005.

[166] Chrysiis Michaloglou, Liesbeth C W Vredeveld, Maria S Soengas, Christophe Denoyelle, Thomas Kuilman, Chantal M a M van der Horst, Donné M Majoor, Jerry W Shay, Wolter J Mooi, and Daniel S Peeper. BRAFE600-associated senescence-like cell cycle arrest of human naevi. *Nature*, 436(7051):720–4, August 2005.

[167] David Dankort, David P Curley, Robert a Cartlidge, Betsy Nelson, Anthony N Karnezis, William E Damsky, Mingjian J You, Ronald a DePinho, Martin McMahon, and Marcus Bosenberg. Braf(V600E) cooperates with Pten loss to induce metastatic melanoma. *Nature genetics*, 41(5):544–52, May 2009.

[168] Nathalie Dhomen, Jorge S Reis-Filho, Silvy da Rocha Dias, Robert Hayward, Kay Savage, Veronique Delmas, Lionel Larue, Catrin Pritchard, and Richard Marais. Oncogenic Braf induces melanocyte senescence and melanoma in mice. *Cancer cell*, 15(4):294–303, April 2009.

[169] V K Goel, N Ibrahim, G Jiang, M Singhal, S Fee, T Flotte, S Westmoreland, F S Haluska, P W Hinds, and F G Haluska. Melanocytic nevus-like hyperplasia and melanoma in transgenic BRAFV600E mice. *Oncogene*, 28(23):2289–98, June 2009.

[170] Jenny Aalborg, Joseph G Morelli, Tim E Byers, Stefan T Mokrohisky, and Lori a Crane. Effect of hair color and sun sensitivity on nevus counts in white children in Colorado. *Journal of the American Academy of Dermatology*, 63(3):430–9, September 2010.

[171] S P Nighswander-Rempel. Quantitative fluorescence spectra and quantum yield map of synthetic pheomelanin. *Biopolymers*, 82(6):631–7, August 2006.

[172] Aravind Krishnaswamy and Gladimir V.G. Baranoski. A Biophysically-Based Spectral Model of Light Interaction with Human Skin. *Computer Graphics Forum*, 23(3):331–340, September 2004.

[173] Lu Wei and Wei Min. Pump-probe optical microscopy for imaging nonfluorescent chromophores. *Analytical and bioanalytical chemistry*, 403(8):2197–202, June 2012.

[174] Thomas E Matthews, Ivan R Piletic, M Angelica Selim, Mary Jane Simpson, and Warren S Warren. Pump-probe imaging differentiates melanoma from melanocytic nevi. *Science translational medicine*, 3(71):71ra15, February 2011.

[175] Francisco E Robles, Jesse W Wilson, Martin C Fischer, and Warren S Warren. Phasor analysis for nonlinear pump-probe microscopy. *Optics Express*, 20(15):17082, July 2012.

[176] Mary Jane Simpson, Jesse W Wilson, M Anthony Phipps, Francisco E Robles, M Angelica Selim, and Warren S Warren. Nonlinear Microscopy of Eumelanin and Pheomelanin with Subcellular Resolution. *The Journal of investigative dermatology*, pages 1–5, January 2013.

[177] S V Frolov and Z V Vardeny. Double-modulation electro-optic sampling for pump-and-probe ultrafast correlation measurements. *Review of Scientific Instruments*, 69(3):1257, 1998.

[178] J Brian Nofsinger, Tong Ye, and John D Simon. Ultrafast Nonradiative Relaxation Dynamics of Eumelanin. *The Journal of Physical Chemistry B*, 105(14):2864–2866, April 2001.

[179] Tong Ye and John D. Simon. Ultrafast Spectroscopic Study of Pheomelanin: Implications on the Mechanism of Superoxide Anion Formation. *The Journal of Physical Chemistry B*, 106(24):6133–6135, June 2002.

[180] Tong Ye and John D Simon. The action spectrum for generation of the primary intermediate revealed by ultrafast absorption spectroscopy studies of pheomelanin. *Photochemistry and photobiology*, 77(1):41–5, January 2003.

[181] Tong Ye and John D Simon. Comparison of the Ultrafast Absorption Dynamics of Eumelanin and Pheomelanin. *The Journal of Physical Chemistry B*, 107(40):11240–11244, October 2003.

[182] Peifang Tian and Warren S Warren. Ultrafast measurement of two-photon absorption by loss modulation. *Optics letters*, 27(18):1634–6, September 2002.

[183] Dan Fu, Tong Ye, Thomas E Matthews, Gunay Yurtsever, and Warren S Warren. Two-color, two-photon, and excited-state absorption microscopy. *Journal of biomedical optics*, 12(5):054004, 2007.

[184] Dan Fu, Tong Ye, Thomas E Matthews, James Grichnik, Lian Hong, John D Simon, and Warren S Warren. Probing skin pigmentation changes with transient absorption imaging of eumelanin and pheomelanin. *Journal of biomedical optics*, 13(5):054036, 2008.

[185] Thomas E Matthews, Jesse W Wilson, Simone Degan, Mary Jane Simpson, Jane Y Jin, Jennifer Y Zhang, and Warren S Warren. In vivo and ex vivo epi-mode pump-probe imaging of melanin and microvasculature. *Biomedical optics express*, 2(6):1576–83, June 2011.

[186] NB Colthup, LH Daly, and SE Wiberley. *Introduction to Infrared and Raman Spectroscopy*. 1990.

[187] Zhiwei Huang, Harvey Lui, X K Chen, Abdulmajeed Alajlan, David I McLean, and Haishan Zeng. Raman spectroscopy of in vivo cutaneous melanin. *Journal of biomedical optics*, 9(6):1198–205, 2004.

[188] Ismael Galván, Alberto Jorge, Francisco Solano, and Kazumasa Wakamatsu. Vibrational characterization of pheomelanin and trichochrome F by Raman spectroscopy. *Spectrochimica acta. Part A, Molecular and biomolecular spectroscopy*, 110:55–9, June 2013.

[189] Ismael Galván, Alberto Jorge, Kazuma Ito, Keisuke Tabuchi, Francisco Solano, and Kazumasa Wakamatsu. Raman spectroscopy as a non-invasive technique for the quantification of melanins in feathers and hairs. *Pigment cell & melanoma research*, 26(6):917–23, November 2013.

[190] Conor L Evans, Eric O Potma, Mehron Puoris'haag, Daniel Côté, Charles P Lin, and X Sunney Xie. Chemical imaging of tissue in vivo with video-rate coherent anti-Stokes Raman scattering microscopy. *Proceedings of the National Academy of Sciences of the United States of America*, 102(46):16807–12, November 2005.

[191] PD Maker and RW Terhune. Study of Optical Effects Due to an Induced Polarization Third Order in the Electric Field Strength. *Physical Review*, 137(3), 1965.

[192] M D Duncan, J Reintjes, and T J Manuccia. Scanning coherent anti-Stokes Raman microscope. *Optics letters*, 7(8):350–2, August 1982.

[193] Andreas Zumbusch, Gary Holtom, and X Xie. Three-Dimensional Vibrational Imaging by Coherent Anti-Stokes Raman Scattering. *Physical Review Letters*, 82(20):4142–4145, May 1999.

[194] Thomas Hellerer, Claes Axäng, Christian Brackmann, Per Hillertz, Marc Pilon, and Annika Enejder. Monitoring of lipid storage in Caenorhabditis elegans using coherent anti-Stokes Raman scattering (CARS) microscopy. *Proceedings of the National Academy of Sciences of the United States of America*, 104(37):14658–63, September 2007.

[195] Yookyung Jung, Joanna H Ng, Cameron P Keating, Prabhu Senthil-Kumar, Jie Zhao, Mark a Randolph, Jonathan M Winograd, and Conor L Evans. Comprehensive evaluation of peripheral nerve regeneration in the acute healing phase using tissue clearing and optical microscopy in a rodent model. *PloS one*, 9(4):e94054, January 2014.

[196] Jaime Imitola, Daniel Côté, Stine Rasmussen, X Sunney Xie, Yingru Liu, Tanuja Chitnis, Richard L Sidman, Charles P Lin, and Samia J Khoury. Multimodal coherent anti-Stokes Raman scattering microscopy reveals microglia-associated myelin and axonal dysfunction in multiple sclerosis-like lesions in mice. *Journal of biomedical optics*, 16(2):021109, February 2011.

[197] Conor L Evans, Xiaoyin Xu, Santosh Kesari, X Sunney Xie, Steven T C Wong, and Geoffrey S Young. Chemically-selective imaging of brain structures with CARS microscopy. *Optics express*, 15(19):12076–87, September 2007.

[198] Paul D A Pudney, Mickaël Mélot, Peter J Caspers, Andre Van Der Pol, and Gerwin J Puppels. An in vivo confocal Raman study of the delivery of trans retinol to the skin. *Applied spectroscopy*, 61(8):804–11, August 2007.

[199] Maxwell Zimmerley, Chia-Yu Lin, David C Oertel, Jennifer M Marsh, Jimmie L Ward, and Eric Olaf Potma. Quantitative detection of chemical compounds in human hair with coherent anti-Stokes Raman scattering microscopy. *Journal of biomedical optics*, 14(4):044019, 2011.

[200] Yookyung Jung, Joshua Tam, H Ray Jalian, R Rox Anderson, and Conor L Evans. Longitudinal, 3D In Vivo Imaging of Sebaceous Glands by Coherent Anti-Stokes Raman Scattering Microscopy: Normal Function and Response to Cryotherapy. *The Journal of investigative dermatology*, pages 1–6, July 2014.

[201] GW Chantry and A Anderson. The raman effect. *Vol. 1Marcel Dekker, New York*, April 1971.

[202] T Dieing, O Hollricher, and J Toporski. *Confocal Raman Microscopy*. 2011.

[203] Y R Shen. *The principles of nonlinear optics*. Wiley Series in Pure and Applied Optics. J. Wiley, 1984.

[204] Hilde a Rinia, Mischa Bonn, Michiel Müller, and Erik M Vartiainen. Quantitative CARS spectroscopy using the maximum entropy method: the main lipid phase transition. *Chemphyschem : a European journal of chemical physics and physical chemistry*, 8(2):279–87, February 2007.

[205] Severine Tabone-Eglinger, Monique Wehrle-Haller, Nicole Aebischer, Marie-Claude Jacquier, and Bernhard Wehrle-Haller. Membrane-bound Kit ligand regulates melanocyte adhesion and survival, providing physical interaction with an intraepithelial niche. *FASEB journal : official publication of the Federation of American Societies for Experimental Biology*, 26(9):3738–53, September 2012.

[206] Keith S Hoek, Natalie C Schlegel, Ossia M Eichhoff, Daniel S Widmer, Christian Praetorius, Steingrimur O Einarsson, Sigridur Valgeirsdottir, Kristin Bergsteinsdottir, Alexander Schepsky, Reinhard Dummer, and Eirikur Steingrimsson. Novel MITF targets identified using a two-step DNA microarray strategy. *Pigment cell & melanoma research*, 21(6):665–76, December 2008.

[207] Rizwan Haq, Jonathan Shoag, Pedro Andreu-Perez, Satoru Yokoyama, Hannah Edelman, Glenn C Rowe, Dennie T Frederick, Aeron D Hurley, Abhinav Nellore, Andrew L Kung, Jennifer a Wargo, Jun S Song, David E Fisher, Zolt Arany, and Hans R Widlund. Oncogenic BRAF regulates oxidative metabolism via PGC1α and MITF. *Cancer cell*, 23(3):302–15, March 2013.

[208] Christian W Freudiger, Wei Min, Brian G Saar, Sijia Lu, Gary R Holtom, Chengwei He, Jason C Tsai, Jing X Kang, and X Sunney Xie. Label-free biomedical imaging with high sensitivity by stimulated Raman scattering microscopy. *Science (New York, N.Y.)*, 322(5909):1857–61, December 2008.

[209] Brian G Saar, Christian W Freudiger, Jay Reichman, C Michael Stanley, Gary R Holtom, and X Sunney Xie. Video-rate molecular imaging in vivo with stimulated Raman scattering. *Science*, 330(6009):1368–70, December 2010.

[210] Wei Min, Christian W Freudiger, Sijia Lu, and X Sunney Xie. Coherent nonlinear optical imaging: beyond fluorescence microscopy. *Annual review of physical chemistry*, 62:507–30, May 2011.

[211] Christian W Freudiger, Wei Min, Gary R Holtom, Bingwei Xu, Marcos Dantus, and X. Sunney Xie. Highly specific label-free molecular imaging with spectrally tailored excitation-stimulated Raman scattering (STE-SRS) microscopy. *Nature Photonics*, 5(2):103–109, January 2011.

[212] R W Boyd. *Nonlinear Optics*. Nonlinear Optics Series. Elsevier Science, 2008.

[213] K Jimbow, O Ishida, S Ito, Y Hori, C J Witkop, and R a King. Combined chemical and electron microscopic studies of pheomelanosomes in human red hair. *The Journal of investigative dermatology*, 81(6):506–11, December 1983.

Appendix

A

Supplemental Figures

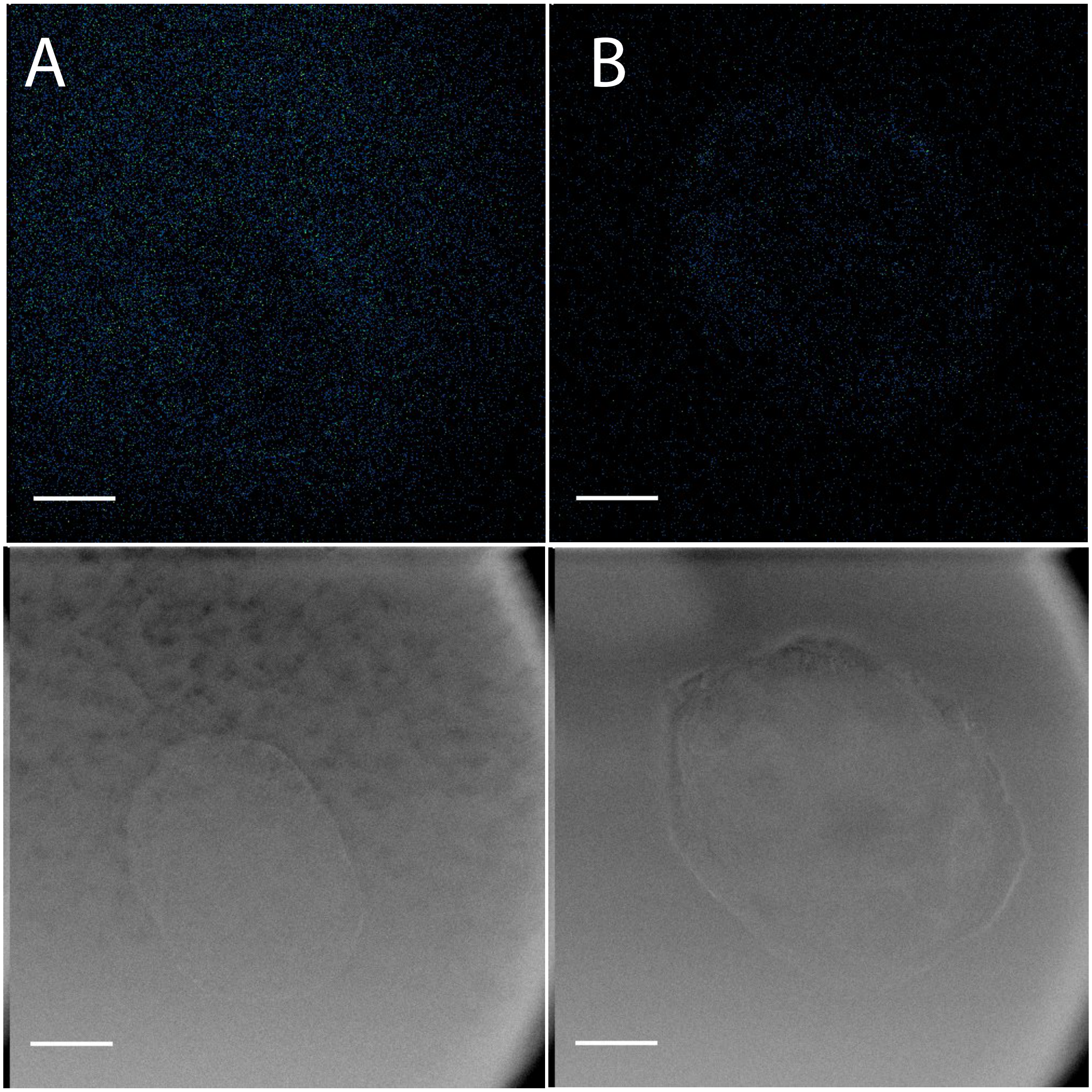

Figure A.1: Commercially available Oxyphor G2 does not penetrate OvCa 3D spheroids. **A**: OvCa spheroids treated with 2 μM Oxyphor G2 for 4 hours demonstrate no appreciable increase in phosphorescence relative to control, treatment-free conditions. **B**: OvCa 3D spheroids, no treatment control. Scale bar = 30 μm.

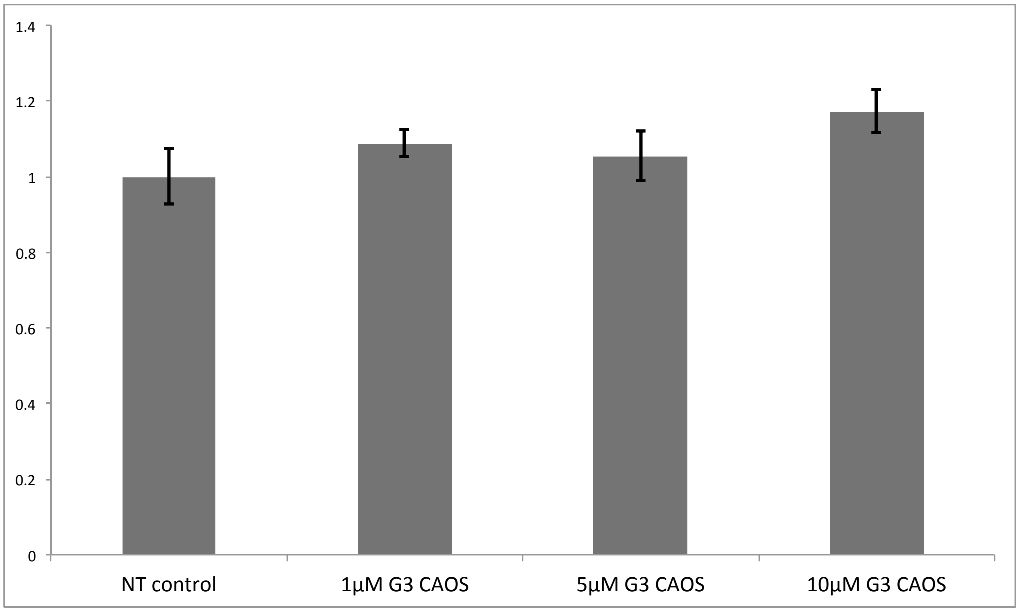

Figure A.2: MTT assay viability results for G3 CAOS nanoconjugates across a range of concentrations. No statistically significant reduction in viability was observed at any concentration tested. Vertical axis: normalized viability.

B

NMR and MALDI-TOF spectra of synthetic products

Compound 1b

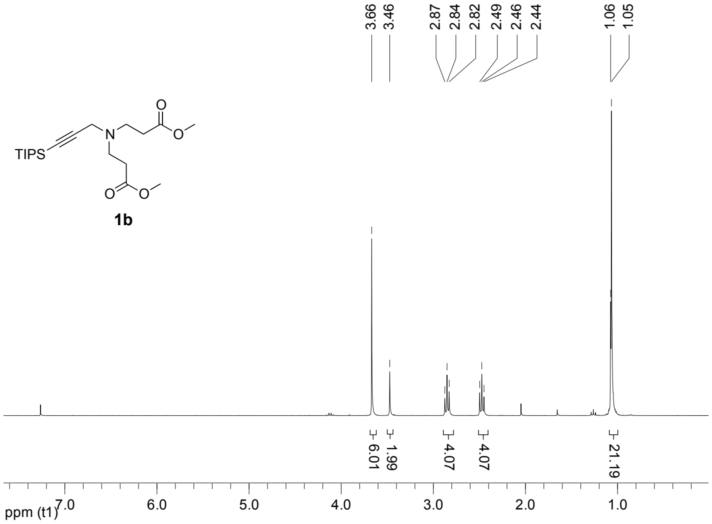

Figure B.1: NMR spectrum of **1b**

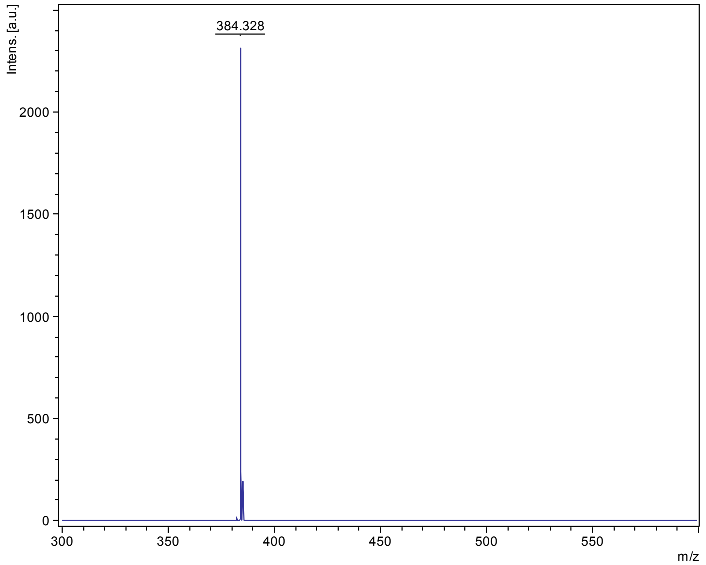

Figure B.2: MALDI spectrum of **1b**

Compound 1c

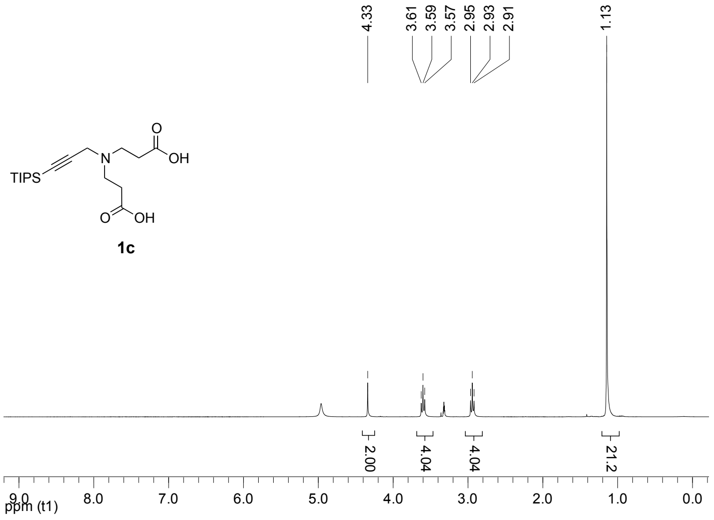

Figure B.3: NMR spectrum of **1c**

Compound 1d

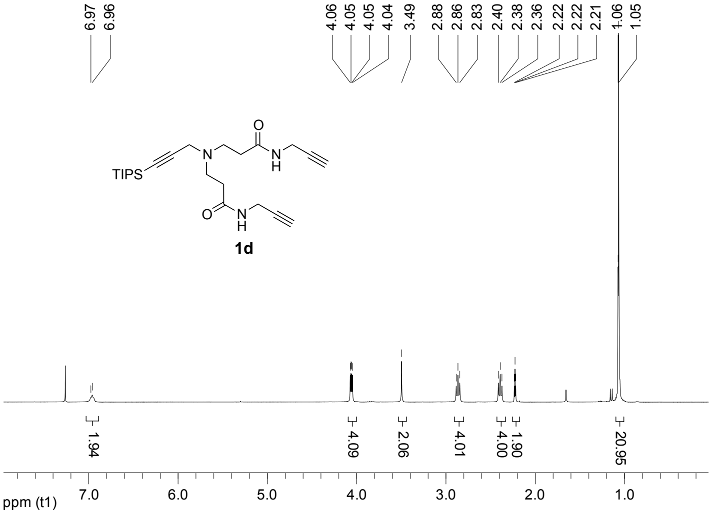

Figure B.4: NMR spectrum of **1d**

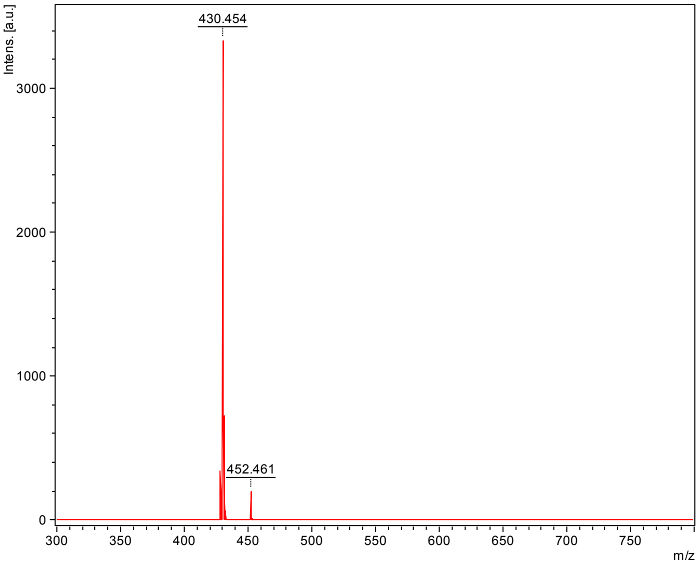

Figure B.5: MALDI spectrum of **1d**

Compound 2b

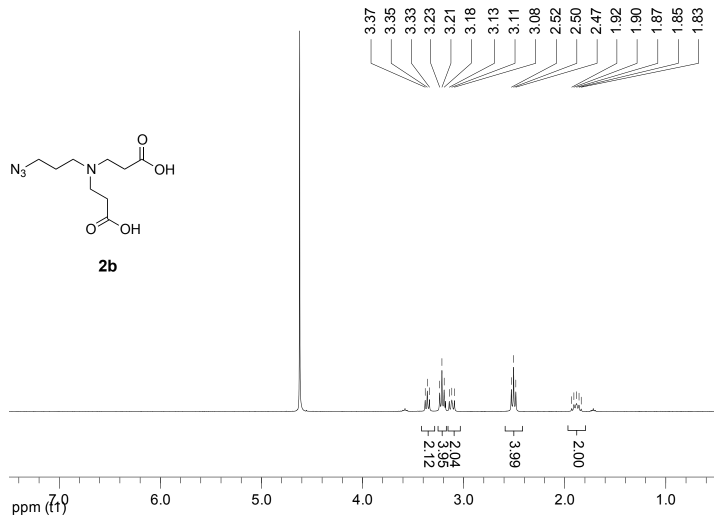

Figure B.6: NMR spectrum of **2b**

Compound 2c

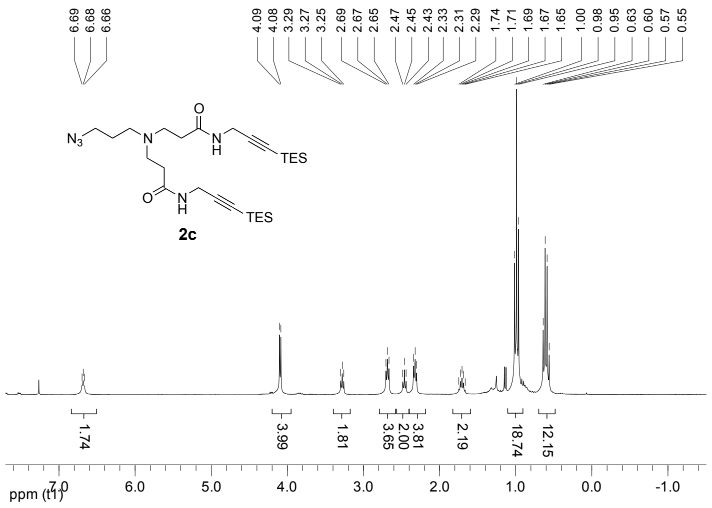

Figure B.7: NMR spectrum of **2c**

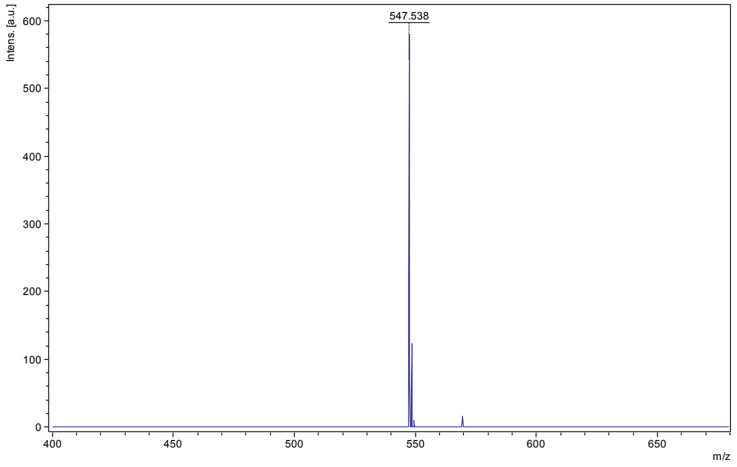

Figure B.8: MALDI spectrum of **2c**

Compound 3b

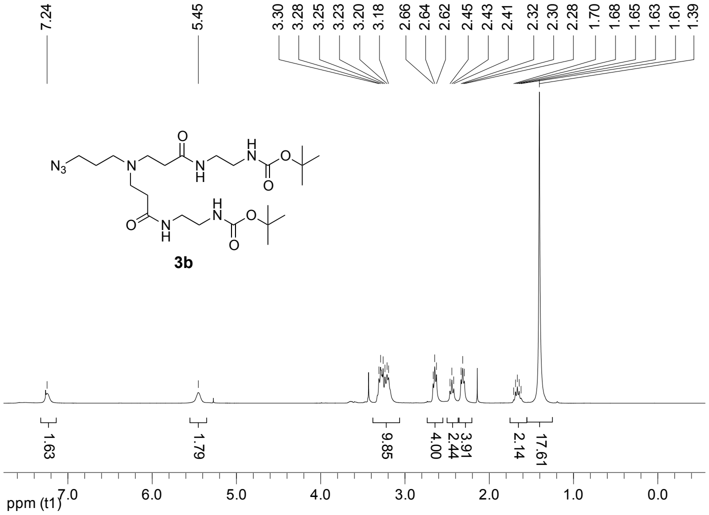

Figure B.9: NMR spectrum of **3b**

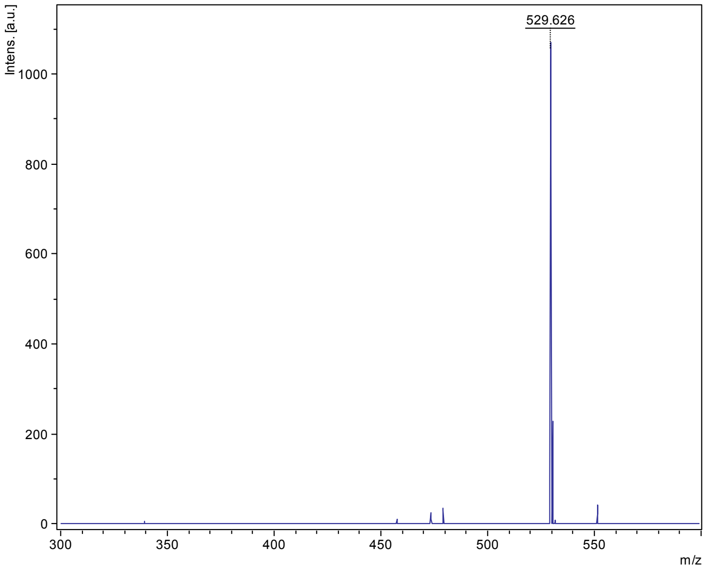

Figure B.10: MALDI spectrum of **3b**

Compound **4a**

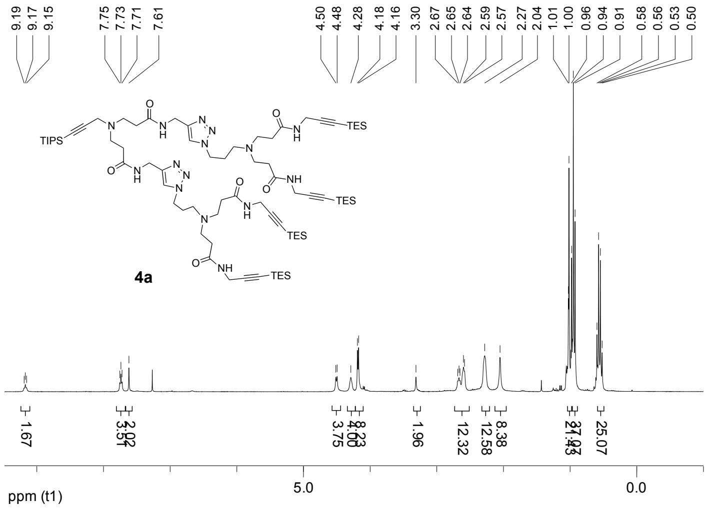

Figure B.11: NMR spectrum of **4a**

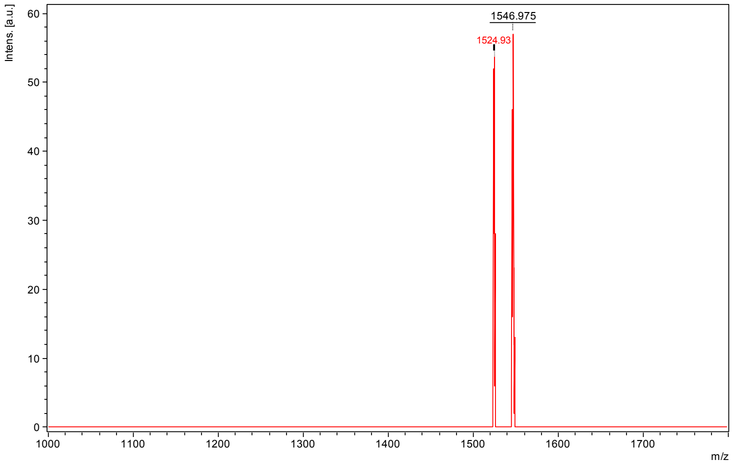

Figure B.12: MALDI spectrum of **4a**

Compound 4b

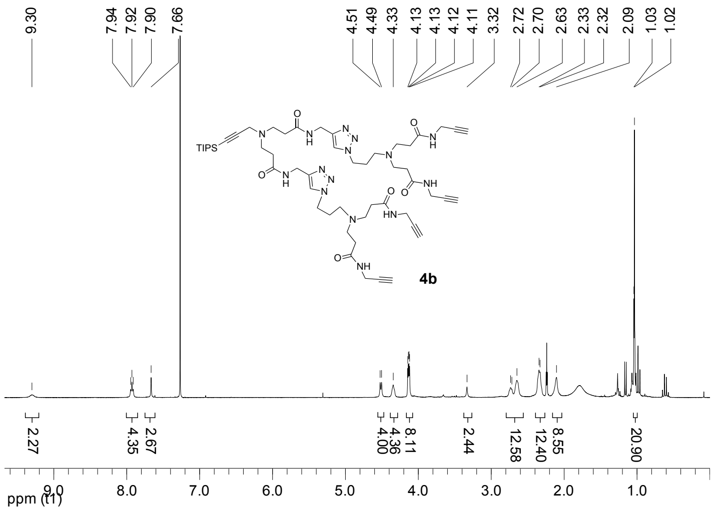

Figure B.13: NMR spectrum of **4b**

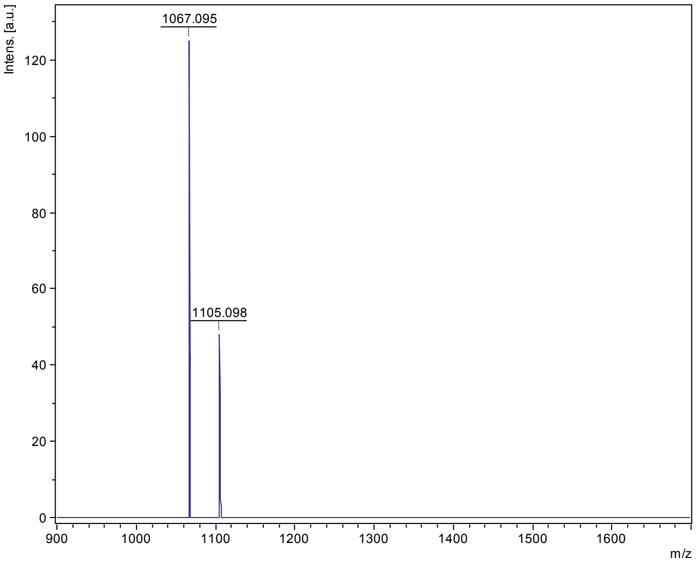

Figure B.14: MALDI spectrum of **4b**

Compound 4c

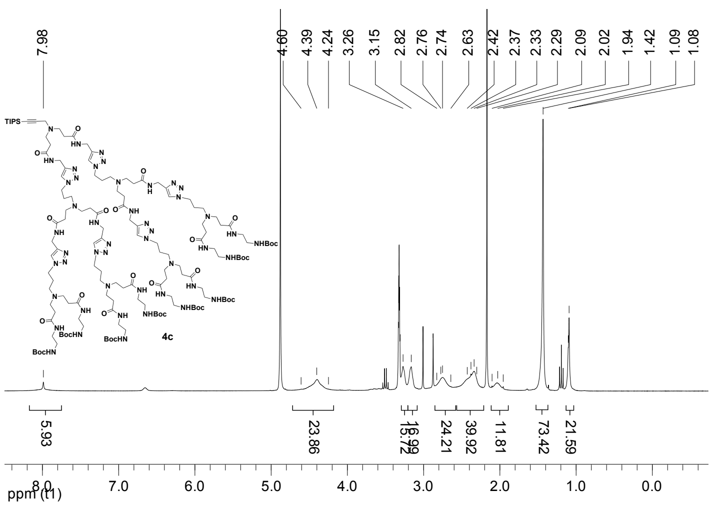

Figure B.15: NMR spectrum of **4c**

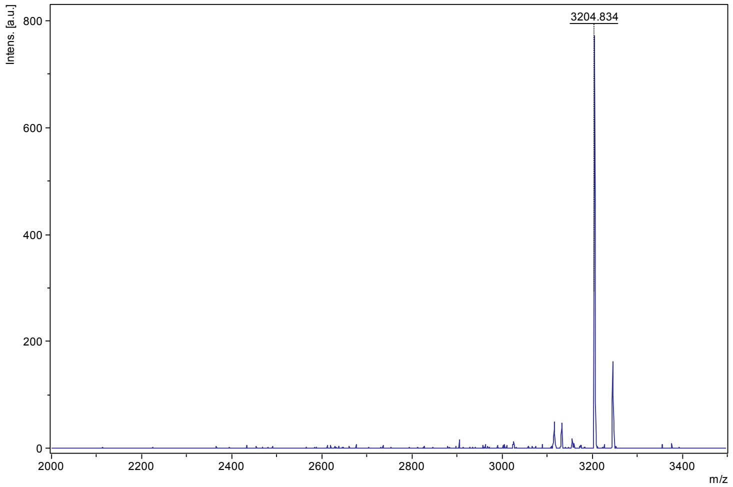

Figure B.16: MALDI spectrum of **4c**

Compound 4d

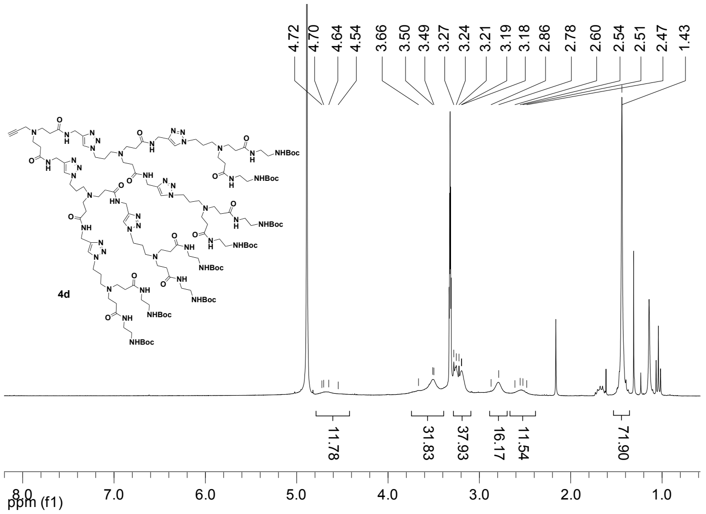

Figure B.17: NMR spectrum of **4d**

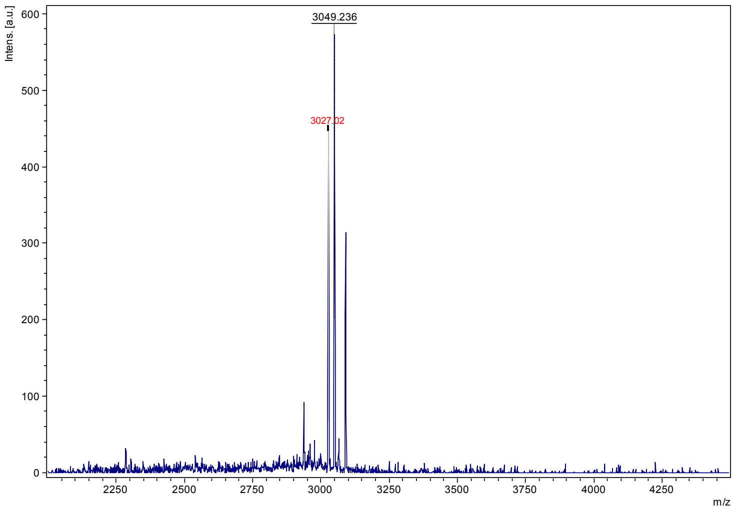

Figure B.18: MALDI spectrum of **4d**

2-azidoethylamine

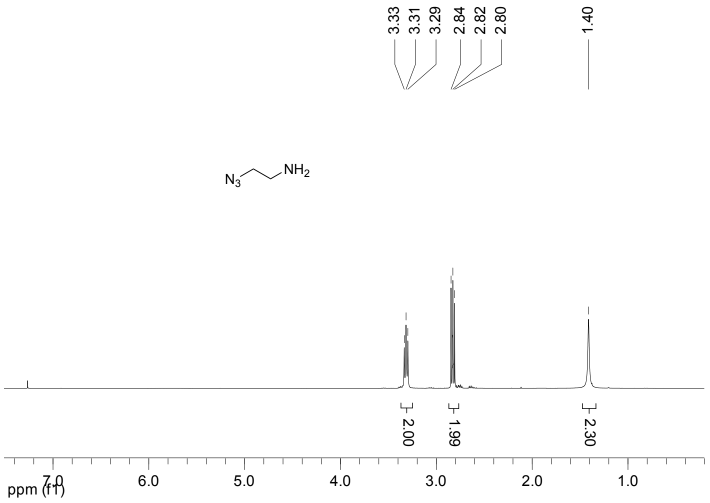

Figure B.19: NMR spectrum of **2-azidoethylamine**

Compound 5b

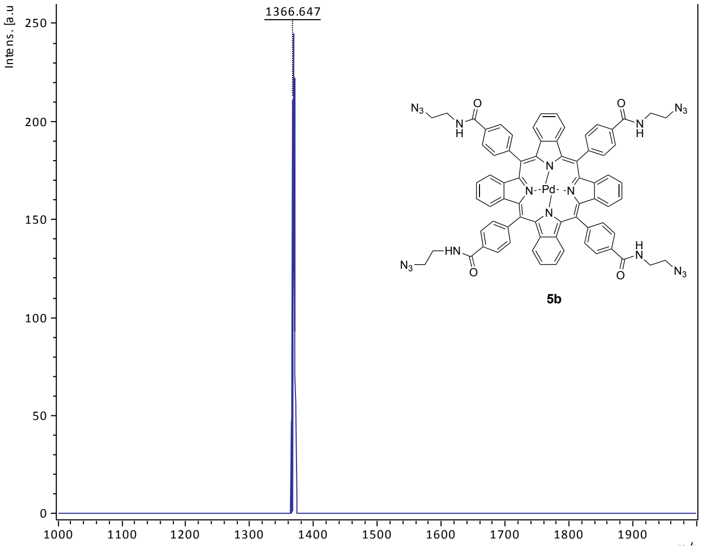

Figure B.20: MALDI spectrum of **5b**

Compound 6b

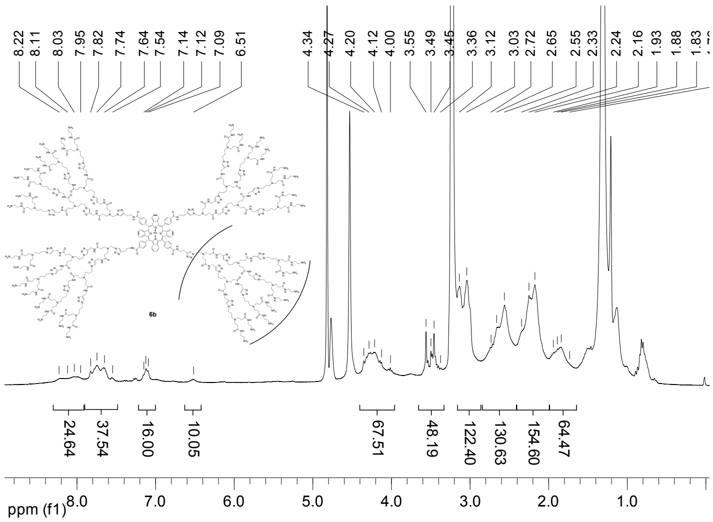

Figure B.21: NMR spectrum of **6b**. Note that the presence of the tetra-adduct G3 CAOS nanoconjugate was not confirmed, as indicated by the brackets in the chemical structure.

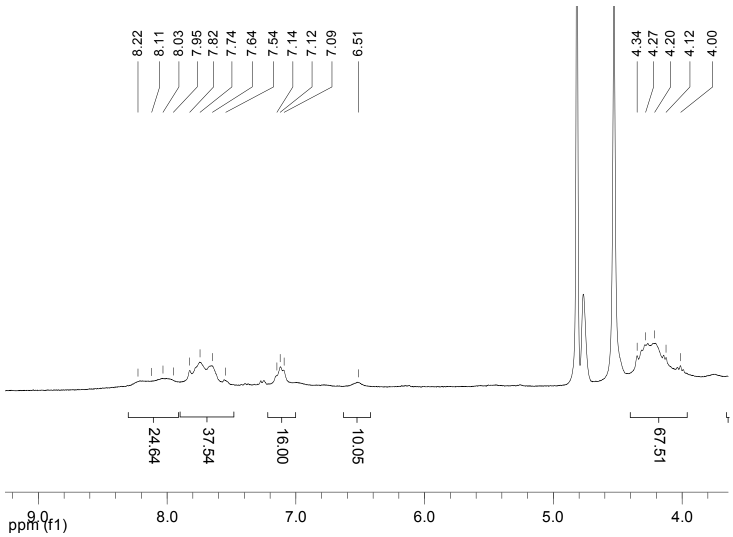

Figure B.22: NMR spectrum of **6b** (expanded).

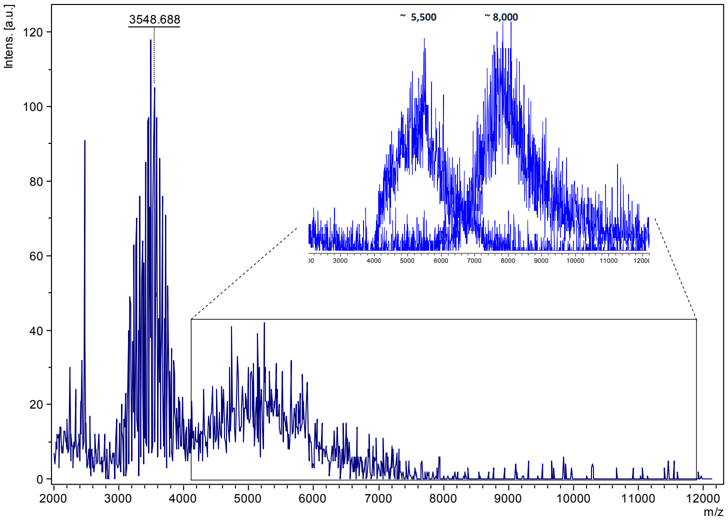

Figure B.23: MALDI spectrum of **6b**

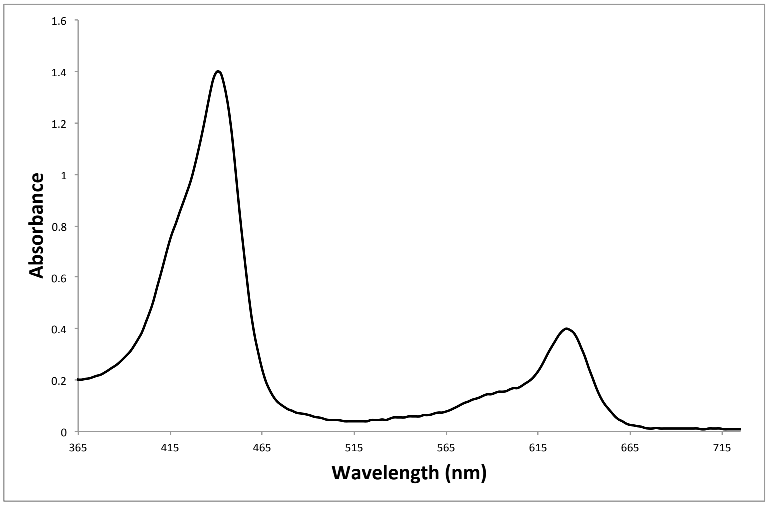

Figure B.24: UV-VIS spectrum of **6b**